Fire performance of ductile fiber reinforced cementitious composites

Liu, Jincheng

2018

FIRE PERFORMANCE OF DUCTILE FIBER REINFORCED CEMENTITIOUS COMPOSITES

LIU JINCHENG

SCHOOL OF CIVIL AND ENVIRONMENTAL ENGINEERING

2018

FIRE PERFORMANCE OF DUCTILE FIBER REINFORCED CEMENTITIOUS COMPOSITES

LIU JINCHENG

School of Civil and Environmental Engineering

A thesis submitted to the Nanyang Technological University
in partial fulfillment of the requirement for the degree of
Doctor of Philosophy

2018

ACKNOWLEDGEMENTS

TABLE OF CONTENTS

SUMMARY

Ductile fiber reinforced cementitious composite (DFRCC), emerged in early 1990s, has been proven to be an excellent building material in terms of structural performance at ambient temperature. Many studies have demonstrated that DFRCC outperforms conventional concrete in terms of seismic performance, impact resistance and durability due to its high tensile ductility and multiple fine cracking behaviors. However, behavior of DFRCC at elevated temperatures remains questionable so far. As fire accidents occur frequently in buildings, there is an urgent need to improve and evaluate fire performance of DFRCC.

This thesis focuses mainly on two topics: (a) improve and study mechanical performance of fire-damaged DFRCC (b) re-examine fire-induced concrete spalling mechanism and assess thermal spalling risk of DFRCC.

An experimental program was designed to optimize post-fire responses of DFRCC. The optimized DFRCC mix was then subjected to fire resistance testing, which covered two aspects, i.e., residual mechanical properties and thermal spalling resistance. The optimized DFRCC were observed to perform better than normal concrete in these two aspects.

Fire-induced spalling is perhaps the least understood of the major issues plaguing concrete in fire. Many studies have attempted to better understand the underlying mechanisms behind fire-induced spalling; however, several controversies still exist. A unified fire-induced concrete spalling theory was advanced in this thesis, which classifies fire-induced spalling into three types based on their distinct spalling mechanisms. They are thermo-hygral, thermal-mechanical, and thermal-chemical spalling, respectively. Hot permeability test and microstructural analysis techniques were used to study the mechanism of PVA fibers in DFRCC

to combating thermo-hygral spalling. A numerical model with reasonable accuracy was also proposed to assess thermo-hygral spalling risk of concrete.

LIST OF TABLES

LIST OF FIGURES

XII

XIII

XIV

XV

CHAPTER 1. INTRODUCTION

1.1 Background and motivation

Concrete, the most-widely used construction material in the world, is intrinsically brittle. A number of approaches have been attempted to overcome the brittle nature of concrete over the years, among which the most effective means is the use of fibers. This results in fiber reinforced concrete (FRC), which is featured by its tension softening. This means that decreasing load can still be sustained as a crack opens. In early 1990s, a special class of FRC, ductile fiber reinforced cementitious composite (DFRCC), was invented through tailoring of fibers, matrix and interface based on theory of steady-state crack propagation and micromechanics (Li and Leung 1992). DFRCC is also known as engineered cementitious composite (ECC), strain hardening cementitious composite (SHCC) and bendable concrete. The fundamental difference in mechanical performance between DFRCC and FRC is that, DFRCC shows pseudo strain-hardening behavior instead of strain softening behavior exhibited by FRC under direct uniaxial tension. The pseudo strain-hardening of DFRCC is achieved by sequential formation of multiple fine cracks. Typical tensile behaviors of concrete, FRC and DFRCC are schematically shown in Fig. 1.1(a)-(c). Clearly, DFRCC in Fig. 1.1(c) shows strain hardening property with multiple fine cracks compared to concrete in Fig. 1.1(a) or FRC in Fig. 1.1(b). Fig. 1.1 also shows the advances in ductility of concrete materials over the years, arising from persistent efforts by many researchers worldwide.
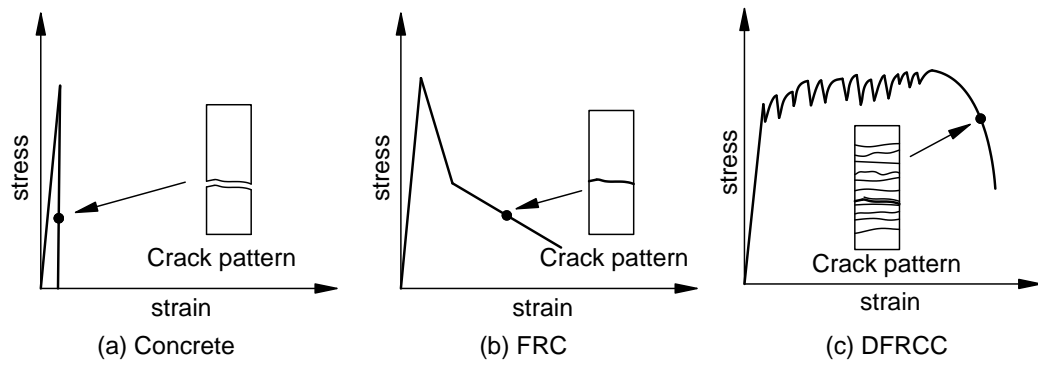
Fig. 1.1 Typical tensile behaviors of concrete, FRC and DFRCC

An ideal construction material should have satisfactory performance under different environmental or extreme loading conditions (explosion, impact, earthquake, fire) as shown in Fig. 1.2. So far, a significant number of works (Fukuyama et al. 2000, Douglas and Billington 2005, Yang and Li 2006, Şahmaran and Li 2009, Mechtcherine et al. 2011, van Zijl et al. 2012, Qudah and Maalej 2014) have been conducted to study durability, seismic performance and impact resistance of DFRCC. Owing to its intrinsic ductile nature, DFRCC outperforms concrete or FRC in terms of durability, seismic resistance, and impact resistance. Another important advantage of DFRCC in addition to high tensile ductility is that it exhibits multiple self-controlled fine cracks at large deformation stage. Due to its intrinsic self healing with crack width less than 0.1 mm, DFRCC has exceptional durability performance under different environmental loads. So far the understanding of DFRCC under earthquake, impact and environmental actions is gradually improving, but the knowledge of performance of DFRCC under fire action is rather limited. In terms of material constituents, DFRCC is typically made of cement, fly ash (FA), fine sand, water, Polyvinyl Alcohol (PVA) fibers and some common chemical additives. The PVA fiber, an indispensable element in achieving tensile strain-hardening of DFRCC, melts at about 240 ℃. Thus, DFRCC will shortly lose its prominent advantage in fire and become no different from ordinary mortar. Besides, melting of PVA fibers introduces

additional porosity, which tends to reduce mechanical strength of DFRCC. Therefore, fire performance of DFRCC is questionable and needs to be studied comprehensively, so that the material can be used safely in construction of structural members.

(a) Durability   (b) Explosion   (c) Impact   (d) Earthquake   (e) Fire
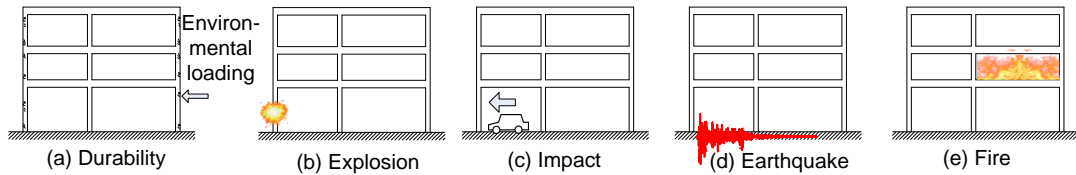
Fig. 1.2 Building materials under different environmental or loading conditions

The very first published work on fire performance of DFRCC dates back to 2010, which presented compressive properties and microstructure of fire-damaged DFRCC (Sahmaran et al. 2010). Following that, the effects of fly ash, specimen dimensions, and PVA fibers on compressive properties of fire-damaged DFRCC (Şahmaran et al. 2011, Erdem 2014) were studied. In general, DFRCC performs similar to or better than concrete or FRC in terms of compressive strength degradation. Limited test data (Bhat et al. 2014, da Silva Magalhães et al. 2015, Yu et al. 2015) was available for residual tensile properties of fire-damaged DFRCC. Different trends in strain capacity of DFRCC were found below 200 °C, possibly due to use of different DFRCC mixes. Above 250 °C, DFRCC lost its strain-hardening behavior (Bhat et al. 2014, da Silva Magalhães et al. 2015). Previous work gained an in-depth insight into mechanical behaviors of fire-damaged DFRCC. However, little effort was made to improve mechanical properties of fire-damaged DFRCC.

Fire performance of concrete materials includes two main aspects: high-temperature mechanical properties and explosive spalling resistance. So far, little work has been done to evaluate explosive spalling risk of DFRCC. In previous work, the specimens used for compressive tests were also used for spalling risk assessment (Şahmaran et al. 2011, Erdem 2014). However, explosive

spalling is influenced by the specimen dimensions and heating rate. Therefore, there is still a need to re-examine explosive spalling risk of DFRCC and the role of PVA fibers in resisting explosive spalling.

Before studying spalling resistance of DFRCC, thermal spalling mechanism needs to be understood thoroughly. Currently, there are two main mechanisms to explain fire-induced concrete spalling: spalling due to (a) pore pressure buildup or (b) thermal stress. The relative importance of these two mechanisms has been a subject of intense debate in the research community over the past few decades. No universal agreement has been reached on this unresolved problem so far. Understanding the spalling mechanism is crucial to predicting and mitigating this unfavorable phenomenon. Therefore, it is important to address the controversy surrounding existing spalling theories and to propose a unified and consistent spalling theory.

1.2 Objectives

The main objectives of this thesis are listed as follows:

- To improve fire resistance of DFRCC;

- To study residual mechanical properties of improved DFRCC after exposure to elevated temperature;

- To re-examine historical views of concrete spalling under fire, resolve existing contradictions and propose a unified and consistent concrete spalling theory;

- To examine explosive spalling resistance of DFRCC materials under fire conditions;

- To measure permeability of DFRCC at elevated temperatures;

- To develop a simple numerical model to predict heat and moisture transfer, pore pressure buildup and explosive spalling in concrete under fire.

1.3 Thesis layout

The layout of this thesis is shown in Fig. 1.3.
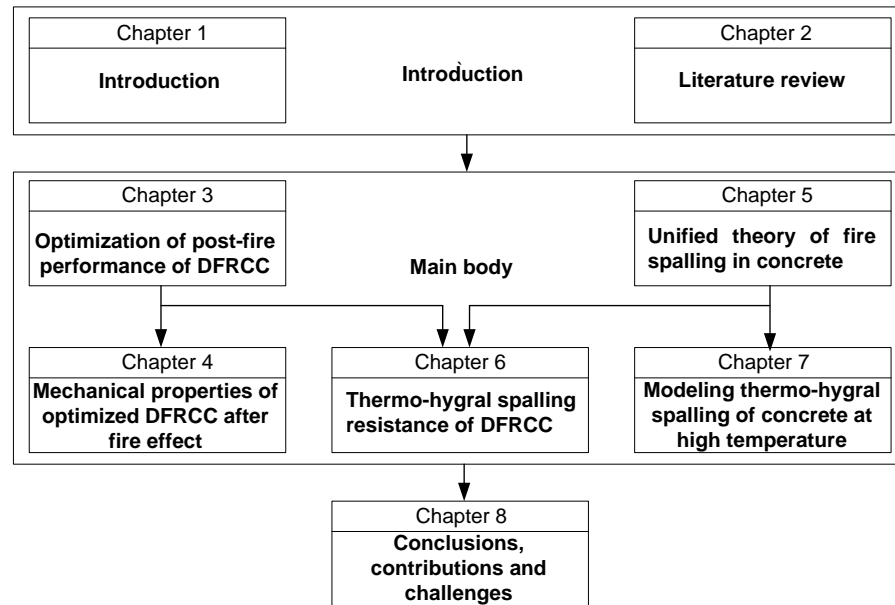
Fig. 1.3 Thesis layout

This thesis consists of eight chapters, starting with the introduction in Chapter 1, followed by six chapters presenting the main elements of author's work.

Chapter 2 reviews previous studies on high-temperature mechanical properties, spalling resistance of DFRCC, and spalling mechanisms of concrete. Furthermore, questions remained unanswered in these aspects will be discussed.

Chapter 3 presents an experimental program to optimize post-fire mechanical properties of DFRCC by means of Taguchi approach (Roy 2010) and utility concept.

Chapter 4 examines compressive properties and tensile properties of optimized DFRCC material developed in Chapter 3.

Chapter 5 summarizes conflicting and concordant points on concrete spalling at high temperature and proposes a unified and coherent fire-induced concrete

spalling theory. Recommendations to mitigate fire spalling of concrete are given following the new spalling theory.

Chapter 6 presents a test program to study explosive spalling resistance and permeability of DFRCC at high temperature. The influence of hot permeability on spalling resistance of DFRCC and the role of fibers in mitigating explosive spalling will be discussed.

Chapter 7 proposes a one-dimensional numerical model to predict moisture migration, pore pressure and fire-induced spalling in concrete. Case studies from different perspectives are presented to validate the applicability of the spalling model.

Finally, Chapter 8 draws overall conclusions and recommends future work based on the research conducted in this thesis.

CHAPTER 2. LITERATURE REVIEW

2.1 Introduction

This chapter offers a critical review of the research that is pertinent to the work of this thesis. First, a review of fire performance of DFRCC is provided. The fire performance of DFRCC includes high-temperature mechanical properties, thermal properties, and thermal spalling resistance of DFRCC. Next, the research that has been conducted on fire-induced concrete spalling mechanism, spalling mitigation mechanism of polypropylene (PP) and PVA fibers, and fire-induced concrete spalling model is summarized. At the end of this chapter, the research problems and knowledge gaps pertaining to the topics of this thesis are identified and discussed based on the literature review. These identified problems and knowledge gaps provide research subjects to be studied and discussed in the main body of this thesis.

2.2 Fire performance of DFRCC

2.2.1 Compressive properties of DFRCC after elevated temperature

Quite a number of researchers had investigated residual compressive properties of different DFRCC mixes. Table 2.1 summarizes the DFRCC mixes used for residual compressive tests. Fig. 2.1 and Fig. 2.2 give residual compressive strength and residual compressive strength reduction factor of DFRCC, respectively. From Fig. 2.2, it can be seen that DFRCC performs similarly to or slightly better than normal concrete (EN 2004) in terms of compressive strength degradation.

Table 2.1 Summary of the DFRCC mixes used for residual compressive tests *

Source	Cement	FA	Sand	Water	PVA fiber	HRWR[†]	HPMC[‡]
Sahmaran et al. (2010)	1	1.2	0.8	0.58	2.0%	0.004	
Şahmaran et al. (2011)	1	2.2	1.16	0.85	2.0%	0.005	
Erdem (2014)	1	1.2	0.8	0.58	2.0%	0.004	
Bhat et al. (2014)	1	1.9	1	0.57	2.0%	0.002	0.001
Yu et al. (2014)	1	0.4	0.7	0.49	2.0%	0.02	0.003
da Silva Magalhães et al. (2015)	1	1.2	0.8	0.8	2.0%	0.03	
Yu et al. (2015)	1	4.4	1.94	1.4	2.0%	0.018	

* Content of fibers is written as volume fraction of the mix, while the other ingredients are written as mass proportion of cement.

† HRWR: high-range water reducer.

‡ HPMC: hydroxypropyl methylcellulose
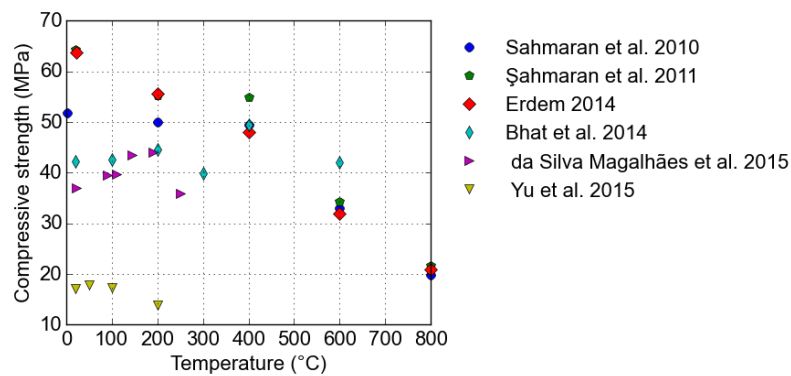
Fig. 2.1 Compressive strength of DFRCC as a function of temperature
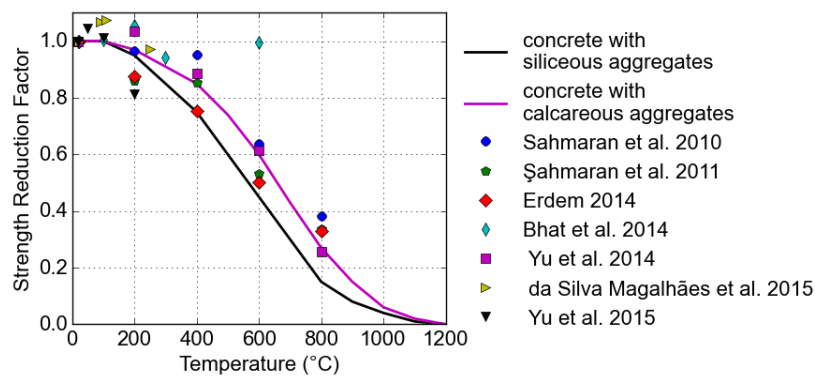
Fig. 2.2 Compressive strength reduction factor of DFRCC with temperature

● Effect of FA replacement ratio

Şahmaran et al. (2011) found that DFRCC with a FA/cement replacement ratio of about 70% had a lower reduction in compressive strength and stiffness than DFRCC with a FA/cement replacement ratio of 55%, after exposure to temperatures from 200 to 600 ℃. Two reasons were proposed to account for this. The first was that DFRCC with a lower FA/cement replacement ratio had a denser microstructure, which induced more of vapor pressure buildup upon heating and resulted in cracking. The second was that pozzolanic reaction between calcium hydroxide (CH) and FA reduced amount of CH, resulting in less cracking and improved compressive strength (Xu et al. 2001). However, this advantage of DFRCC with approximately 70% FA/cement replacement became weaker after exposure to 800 ℃.

● Effect of specimen dimensions

Erdem (2014) observed that residual compressive properties of DFRCC were almost insensitive to changes in specimen dimensions and concluded that DFRCC can be regarded as independent of size effect in terms of high-temperature deterioration. No reasons were given to explain this size-effect independence in his work. The size-effect independence at room temperature was due to high tensile strain capacity of DFRCC. This is confirmed by finding by Nguyen et al. (2013) that concrete with a higher tensile strain capacity showed less sensitivity to the specimen size. Size-effect insensitivity of DFRCC after elevated temperature exposure is still not clear. It is possibly related to the PVA fibers in DFRCC.

● Effect of cooling regime

Yu et al. (2014) observed that fire-damaged DFRCC specimens after cooling in water performed better than those subjected to air cooling, and the effect increased

with the temperature exposure level. This was because quenching in water led to rehydration process, which generated more CSH-like gel and crystals.

● Relationship between microstructure and compressive strength

Studies have been conducted to investigate the evolution of porosity and pore structure of DFRCC with elevated temperature (measured after cooling). Fig. 2.3 and Fig. 2.4 give porosity values and average pore diameter of DFRCC as a function of temperature, respectively. The studied DFRCC mixes are given in Table 2.1. From room temperature to 200 ℃, some researchers found an increase in porosity, but some found negligible change. From 200 ℃ onwards, all studies showed an increasing trend of porosity but with different slopes. The average pore diameter of DFRCC was observed to vary a little from room temperature to 400 ℃. But at 600 ℃, there was an apparent change in it. At 800 ℃, its growth range was even larger. The change in compressive strength of DFRCC was found to be closely related with the changes in porosity and average pore diameter. An increase in both porosity and average pore diameter reduces compressive strength.
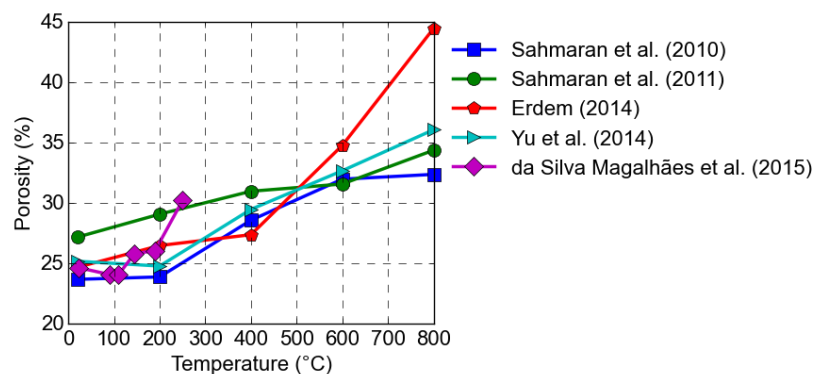
Fig. 2.3 Porosity values of DFRCC as a function of temperature
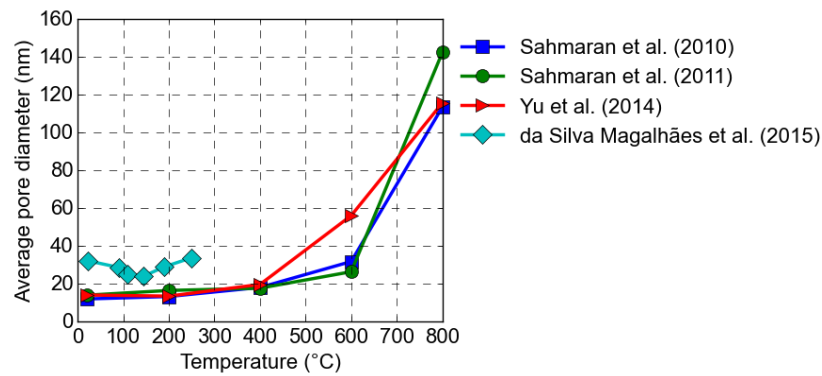
Fig. 2.4 Average pore diameter of DFRCC as a function of temperature

2.2.2 Tensile properties of DFRCC after elevated temperature

Limited work was done to study residual tensile properties of DFRCC after high temperature, since its tensile behavior is expected to be similar to that of mortar after exposure to temperature above the melting point of PVA fibers. Table 2.2 summarizes the DFRCC mixes used for residual tensile tests.

Table 2.2 Summary of the DFRCC mixes used for residual tensile tests *

Source	Cement	FA	Sand	Water	PVA fiber	HRWR	HPMC	SAP[†]
Mechtcherine et al. (2012)	1	1.2	1.06	0.71	2.2%	0.038	0.006	0.004
Bhat et al. (2014)	1	1.9	1	0.57	2.0%	0.002	0.001	
da Silva Magalhães et al. (2015)	1	1.2	0.8	0.8	2.0%	0.03		
Yu et al. (2015)	1	4.4	1.94	1.4	2.0%	0.018		

* Content of fibers is written as volume fraction of the mix, while the other ingredients are written as mass proportion of cement.

† SAP: super absorbent polymer.

Mechtcherine et al. (2012) reported residual tensile performance of DFRCC with 2.2% vol. of PVA fibers subject to 22, 60, 100 and 150 ℃. DFRCC showed a downward trend in both the tensile strain capacity and the tensile strength as

temperature increased. The tensile strain capacity refers to the tensile strain at softening point (JSCE 2008).

da Silva Magalhães et al. (2015) studied residual tensile behaviors of DFRCC heated to a temperature ranging from ambient to 250 ℃. At 90 ℃ the strain capacity of DFRCC mix remained almost unchanged, but declined beyond 90 ℃. At 250 ℃, strain hardening behavior of DFRCC diminished completely.

Bhat et al. (2014) reported that tensile strain capacity of DFRCC decreased as temperature increased from 20 ℃ to 200 ℃. As temperature rose above 200 ℃, DFRCC lost its tensile strain-hardening behavior.

Yu et al. (2015) reported that residual tensile strength and strain capacity of DFRCC with high-volume of fly ash (HVFA) increased at 50 ℃ and 100 ℃, but declined at 200 ℃. Even so, HVFA-DFRCC had a tensile strain capacity of 3.1% after subjected to 200 ℃ for one hour. But compressive strength of this HVFA-DFRCC was only about 17.1 MPa (see Fig. 2.1), which means this HVFA-DFRCC cannot be used for structural applications.

Fig. 2.5 gives the normalized tensile strain capacity of DFRCC by its ambient tensile strain capacity as a function of temperature. To summarize, for DFRCC with compressive strength higher than 30MPa, the strain capacity of DFRCC deteriorated with temperature. At 150 ℃ and above, the strain capacity of DFRCC is quite small already compared to that at ambient. At melting temperature of PVA fibers (about 240 ℃) and above, DFRCC behaves similarly to mortar.
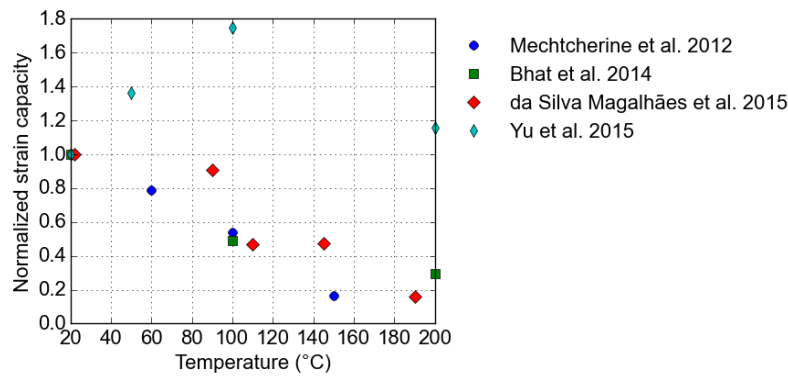
Fig. 2.5 Normalized tensile strain capacity of DFRCC with elevated temperature

2.2.3 Tensile properties of DFRCC at elevated temperature

Mechtcherine et al. (2012) reported in-situ tensile performance of DFRCC with 2.2% vol. PVA fibers subject to different temperatures and strain rates. The test temperatures were 22, 60, 100, and 150 ℃ and the selected strain rates were $10^{-5}\,s^{-1}$, $3\times10^{-4}\,s^{-1}$, and $10^{-2}\,s^{-1}$. At in-situ temperature of 60 ℃, DFRCC showed an increase in strain capacity and a decline in strength under a strain rate of $10^{-5}\,s^{-1}$. At 100 and 150 ℃, DFRCC showed a decrease in both the strain capacity and strength under a strain rate of $10^{-5}\,s^{-1}$. At 150 ℃ DFRCC lost its strain-hardening feature.

Mechtcherine et al. (2012) also observed that hot strain capacity of DFRCC was larger than residual strain capacity of DFRCC at 22, 60, and 100 ℃. But this has limited influence on behavior of DFRCC in fire, since fire temperature exceeds 100 ℃ soon.

2.2.4 Spalling resistance of DFRCC at elevated temperature

● Explosive spalling

DFRCC is cement-based composites, also known as "bendable concrete". Explosive spalling, a common problem faced by concrete, could be a potential threat to DFRCC. So far, there is no particular test designed to investigate spalling

resistance of DFRCC at elevated temperatures. However, some positive findings regarding this aspect of DFRCC have been reported. Şahmaran et al. (2011) found that no explosive spalling occurred in 50 mm DFRCC cube specimens when heated to the maximum temperature of 800 ℃ at 15 ℃/min. Similar observation was found in Bhat et al. (2014), in which ϕ76.2mm×152.4mm cylinder specimens were heated to the maximum temperature of 800 ℃ at 23.5 ℃/min. In contrast, Bhat et al. (2014) observed explosive spalling in control mortar specimens heated to 600 ℃ and above. It is noted that fire spalling is influenced by size of specimens and heating rate. The smaller a specimen is and the lower heating rate it is subjected to, the lower its susceptibility to spalling is (Kodur 2000). Therefore, there is a need to conduct spalling tests to evaluate propensity of DFRCC to spall under heating.

● Hot permeability

Currently, no test data on hot permeability of DFRCC can be found in the literature. There is test data on water permeability of DFRCC at room temperature (Lepech and Li 2009, van Zijl et al. 2012, Wagner et al. 2012), but this property is intended for durability assessment. It is widely accepted that permeability is a critical factor influencing fire spalling of concrete materials (Hertz 2003, Jansson and Boström 2013). It is significant to get first-hand permeability data of DFRCC at elevated temperature and link it with spalling resistance of DFRCC.

2.2.5 Sprayable lightweight DFRCC for fire protection

Instead of studying applications of DFRCC as a structural material, Zhang et al. (2014) developed a sprayable lightweight DFRCC (SL-DFRCC) for fire protection of steel members. The SL-DFRCC was desired to have excellent durability and thermal insulating property. To achieve the desired properties, 3M S38 glass bubbles were used instead of fine silica sand in the SL-DFRCC. The

mix proportion of the SL-DFRCC is shown in Table 2.3. The SL-DFRCC was found to perform better than conventional sprayable fireproof material in terms of mechanical properties, thermal insulation properties and interfacial cohesive strength with steel substrate under impact load.

Table 2.3 Mixture proportion of SL-DFRCC by weight

Source	Cement	Glass bubbles	Water	PVA fiber (by volume)	HRWR	HPMC
Zhang et al. (2014)	1	0.5	0.75	2 %	0.03	0.05

Good cohesive performance of the SL-DFRCC under impact load was achieved by its high ductility. However, the PVA fibers in SL-DFRCC melt under fire, which means SL-DFRCC is one-off fireproof material. In addition to that, only the cohesive performance of SL-DFRCC under impact load is studied. The cohesive performance of SL-DFRCC under fire is questionable, and therefore should be examined.

2.2.6 Thermal properties of DFRCC

Thermal properties of DFRCC are important parameters for conducting heat transfer analysis and subsequent thermo-mechanical analysis of DFRCC members. Compared to the work on mechanical properties of DFRCC after fire, the work on thermal properties of DFRCC is rather limited.

● Thermal conductivity

Magalhães et al. (2011) calculated thermal conductivity values of DFRCC at 20, 40, and 60 ℃ based on measured values of thermal diffusivity and specific heat. Mixture proportion of the DFRCC in their study is given in the fourth row of Table 2.2. Thermal conductivity values and thermal diffusivity values of the DFRCC mix are listed in Table 2.4.

Thermal conductivity of normal weight concrete at 20 ℃ is in between 1.33 and 1.95 W/mK according to Eurocode 2 (EN 2004). Thermal conductivity of DFRCC is smaller than normal weight concrete. It is also noted that thermal conductivity of DFRCC increases from 20 ℃ to 60 ℃. However, thermal conductivity of normal weight concrete shows an opposite trend. This is probably because the moisture in DFRCC samples prepared for thermal conductivity measurement was not removed.

Table 2.4 Thermal properties of DFRCC at 20, 40, and 60 ℃

Temperature (℃)	20	40	60
Thermal conductivity (W/mK)	1.17	1.49	1.62
Thermal diffusivity (m^2/day)	0.0447	0.0512	0.0509
Specific heat (J/kgK)	1344	1468	1628

Huang et al. (2013) measured thermal conductivities of six green lightweight DFRCC (GL-DFRCC) mixtures. To produce the GL-DFRCC mixtures, three kinds of waste materials including iron ore tailings (IOTs), fly ash, and fly ash cenosphere (FAC) were used as shown in Table 2.5. The mixtures were designed to study the influence of FA/cement ratio and replacement percentage of IOTs by FAC on thermal conductivity of GL-DFRCC.

Table 2.5 Mixture proportions of GL-DFRCC (Huang et al. 2013)

FA/cement	Mix ID	Ingredients (kg/m^3)						HRWR/(Cement +FA) (%)
		Cement	FA	IOTs	FAC	Water	Fiber	
2.2	C1[a]	389.5	856.8	448.7	0	324	26	0.46
	C2	389.5	856.8	179.5	84.1	324	26	0.38
	C3	389.5	856.8	0	140.2	324	26	0.33
4.4	C4[a]	227.2	999.7	441.7	0	319	26	0.42
	C5	227.2	999.7	176.7	82.8	319	26	0.32
	C6	227.2	999.7	0	138	319	26	0.26

[a] Control mixes with no FAC.

A thermal capacitance calorimeter was used to measure thermal conductivity of GL-DFRCC mixtures in conformity to ASTM E2584 (2010) at 23 ℃. Fig. 2.6 shows thermal conductivities of GL-DFRCC mixtures normalized by that of

mixture C1 (0.37 W/mK). FA/cement ratio and replacement percentage of IOTs by FAC were found to influence thermal conductivity of GL-DFRCC. The higher these two factors are, the lower thermal conductivity of GL-DFRCC is.
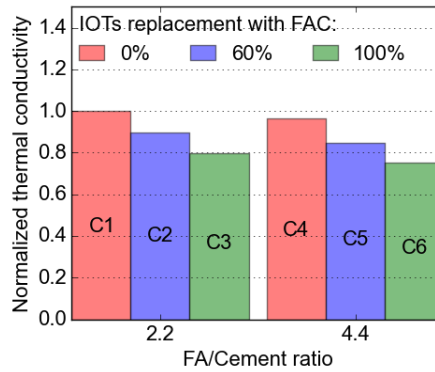
Fig. 2.6 Normalized thermal conductivities of GL-DFRCC mixtures (after Huang et al. (2013))

Zhang et al. (2014) measured thermal conductivity of SL-DFRCC at elevated temperatures in conformity to ASTM E2584 (2010). The detailed information of SL-DFRCC can be seen in Section 2.2.5. The measured thermal conductivity of SL-DFRCC as a function of temperature is shown in Fig. 2.7.
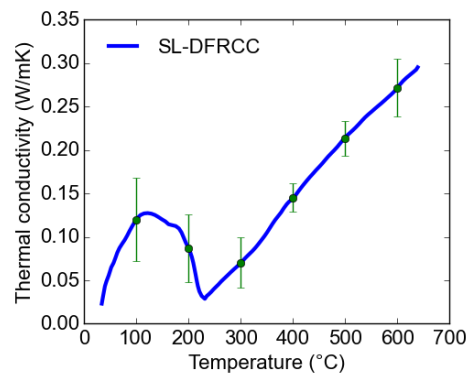
Fig. 2.7 Thermal conductivity of SL-DFRCC (after Zhang et al. (2014))

To summarize, little has been done on thermal conductivity of DFRCC at elevated temperature. Although Zhang et al. (2014) measured thermal conductivity of SL-DFRCC at elevated temperature, SL-DFRCC is not intended for structural use.

● Specific heat

Magalhães et al. (2011) conducted specific heat tests on DFRCC samples at 20, 40, and 60 ℃ in an isothermal calorimeter. Mixture proportion of DFRCC in their study is given in the fourth row of Table 2.2. Specific heat values of DFRCC mixture are listed in Table 2.4. Magalhães et al. (2011) found that the specific values of DFRCC varied linearly from 20 to 60 ℃.

Zhang et al. (2014) measured specific heat of SL-DFRCC at 400 ℃ via differential scanning calorimetry (DSC) in conformity to ASTM E1269 (2011). The detailed information of SL-DFRCC is presented in Section 2.2.5. The measured specific heat of SL-DFRCC is 930 J/kgK at 400 ℃. Zhang et al. (2014) assumed that specific heat of SL-DFRCC is constant from 40 to 670 ℃.

No published result on specific heat of DFRCC at elevated temperatures is found to date.

● Thermal expansion

Magalhães et al. (2011) measured linear thermal expansion coefficients of DFRCC under different temperature exposure processes. The temperature exposure processes and their corresponding measured linear thermal expansion coefficients are listed in Table 2.6. The average value of linear thermal expansion coefficient at ambient temperature is determined to be $11.52 \times 10^{-6}/℃$. There is a lack of data on variations of thermal expansion of DFRCC with greater temperature beyond 40 ℃.

Table 2.6 Thermal expansion coefficients of DFRCC

Temperature exposure process	20 ℃→40 ℃	40 ℃→20 ℃	20 ℃→4 ℃	4 ℃→20 ℃
Linear thermal expansion coefficient (10^{-6}/℃)	10.35	12.66	9.38	13.68

● Density

Mass loss of DFRCC as a function of temperature was studied by Sahmaran et al. (2010), Şahmaran et al. (2011), Bhat et al. (2014) and Yu et al. (2014). The DFRCC mixture proportions they used are listed in Table 2.1. Fig. 2.8 shows the correlation between mass loss of DFRCC samples and heat exposure temperature compared with that of concrete suggested by prENV 1992-1-2 (de Normalisation 1993). The mass loss of DFRCC increased with temperature. Up to 400 ℃, mass loss rate of DFRCC is larger than that of concrete, due to pyrolysis of PVA fibers. It should be noted that the moisture content of their DFRCC samples was not removed when they conducted mass loss tests. However, the mass loss curve of concrete specified in Eurocode2 (Institution 2004) removes the influence of moisture content. In future work, the influence of moisture content of DFRCC should be taken into account. Density of DFRCC at temperatures higher than 800 ℃ should also be measured to fill the knowledge gap.
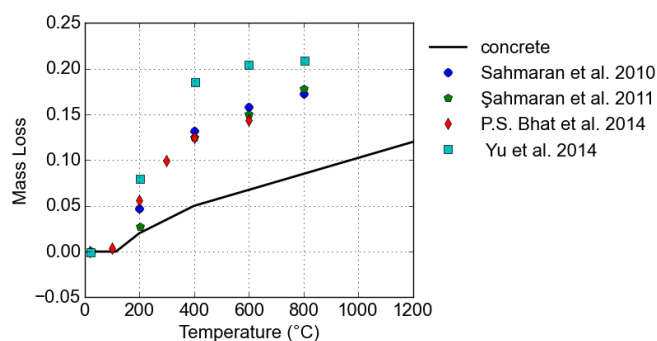
Fig. 2.8 Mass losses of DFRCC and normal weight concrete

2.3 Fire-induced spalling

Fire-induced spalling is a serious threat to concrete structures. It reduces member cross section, exposes reinforcement to fire directly, consequently leading to a much earlier member failure (Dotreppe et al. 1999, Ali et al. 2004). This localized failure endangers the integrity of a structural system as a whole and may trigger progressive collapse in the worst-case scenario. Thus it is important to understand the driving force behind spalling phenomenon and work out solutions to mitigate or even avoid spalling.

2.3.1 Fire-induced spalling mechanism

Fire spalling of concrete is a stochastic and complex phenomenon accompanied by coupled thermo-chemo-hydro-mechanical process. Owing to complexity of the phenomenon and difficulty with identification of the main driving force, three main theories have been proposed to account for fire-induced spalling.

● Thermal stress spalling theory

When concrete member is under fire, a thermal gradient is generated across the member section. The thermal gradient results in restrained thermal expansion, which leads to a buildup of compressive stress in surface concrete and tensile stress in inner concrete as depicted in Fig. 2.9(a). When the compressive stress acting on the heated surface concrete exceeds compressive strength of concrete, spalling of concrete occurs (Saito 1966).

● Pore pressure spalling theory

When concrete is subjected to fire, the temperature of concrete gradually increases and pore pressure builds up as a result of temperature rise and moisture accumulation as depicted in Fig. 2.9(b). Meanwhile, concrete also suffers from a

deterioration of tensile strength and compressive strength. When the tensile stress induced by pore pressure exceeds the tensile strength of concrete at a certain temperature, fire spalling of concrete occurs (Shorter and Harmathy 1965). The pore pressure magnitude is closely related to permeability of concrete; the larger the permeability, the lower the pore pressure is and vice versa. High strength concrete has lower permeability than normal strength concrete, thus leading to higher pore pressure and higher probability of spalling than normal strength concrete, which is in good agreement with observations of fire tests done by researchers (Noumowe et al. 2006, Ngo et al. 2013).

● Combined actions of thermal stress and pore pressure

Fire spalling of concrete originates from the combined actions of thermal stress and pore pressure. When the total stress due to thermal stress and pore pressure surpasses hot tensile strength of concrete, spalling is initiated (Zhukov 1975).

(a) Spalling induced by
thermal stress

(b) Spalling induced by pore
pressure
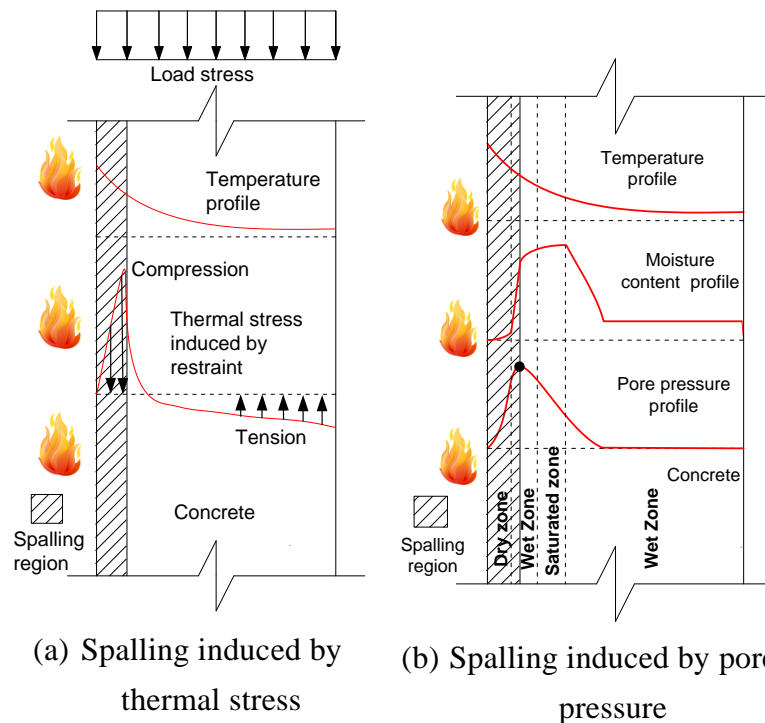
Fig. 2.9 Simplified illustration of two spalling mechanisms (after (Zhukov 1975))

2.3.2 Mechanisms of PP and PVA fibers to combat spalling

● Melting of fibers

Polymeric fibers melt and decompose as temperature increases. Micro-channels originally occupied by fibers form and become available for the transport of moisture. As a result, it leaves little chance for moisture to accumulate and pore pressure to develop inside concrete. Therefore, the probability of spalling is reduced. Table 2.7 lists thermal characteristics of PP and PVA fibers. Spalling occurs between 190 and 250 ℃ (Kalifa et al. 2001), whereas PP fiber melts before reaching the spalling temperature and PVA fiber melts in between the spalling temperature range.

Table 2.7 Thermal characteristics of fibers

	PP fiber	PVA fiber
Glass transition temperature, ℃	-18 (Tapkın 2008)	66 (da Silva Magalhães et al. 2015)
Melting temperature, ℃	160-170 (Tapkın 2008)	244 (da Silva Magalhães et al. 2015)
Decomposition temperature, ℃	341 (Kalifa et al. 2001)	
Thermal expansion, linear, m/m/℃	0.031-0.039 (Tapkın 2008)	

● Interfacial transition zone (ITZ)

Bentz (2000) proffered a percolation theory which assumes ITZs surrounding PP fibers. The ITZs around PP fibers, together with ITZs between cement matrix and aggregates, formed a permeable network for moisture transport.

● Pressure-induced tangential space (PITS)

Khoury (2008) proposed a PITS theory which assumes ITZs surrounding poorly wetted PP fibers form due to vapor pressure induced disruption of interfacial bond

between PP fibers and cement matrix in between 100 and 165 ℃ (see Fig. 2.10). This mechanism continues to work until the temperature reaches the vaporization point of PP fiber. This is because viscosity of melted PP fibers is very high and does not allow for easy transport of the melted fibers in concrete.
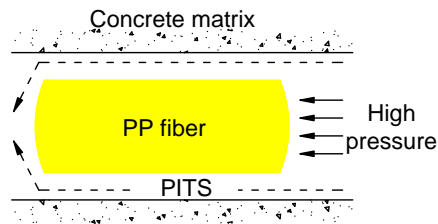
Fig. 2.10 Simplified representation of PITS (after Khoury (2008))
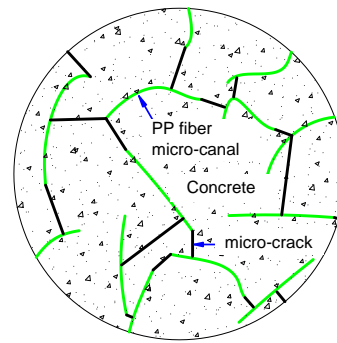
Fig. 2.11 Simplified representation of permeable network of micro-cracks and PP micro-canals

● Micro-cracks induced by fibers

Pistol et al. (2011) developed an innovative methodology to investigate the mode of action of PP fibers in mitigating fire spalling of concrete. The methodology consists of a combination of ultrasonic and acoustic emission measurements at high temperature and microstructure analysis of samples after heating using micro X-ray computed tomography (CT) and scanning electron microscope (SEM). The results showed that micro-cracks were formed around micro channels left by melted PP fibers. The micro-canals and micro-cracks form a filtration network for moisture to escape from concrete interior (see Fig. 2.11).

● Bridging action of PVA fibers

Fiber bridging action is the action of fibers exerting a force across a crack in an attempt to prevent the crack from further widening. Bhat et al. (2014) held that, in

addition to melting of PVA fibers, bridging action of PVA fibers after formation of cracks also contributed to preventing explosive spalling of DFRCC.

However, the melting point of PVA fibers is about 240 ℃ (da Silva Magalhães et al. 2015), but explosive spalling had been observed to occur between 250 ℃ and 300 ℃. Besides, bridging action of PVA fibers becomes less effective upon approaching to 200 ℃ as evidenced by gradual decrease in tensile strain capacity of DFRCC (Bhat et al. 2014). Therefore, whether bridging action of PVA fibers plays a positive role in resisting spalling is questionable.

2.4 Spalling model

A number of spalling models have been developed to predict explosive spalling of concrete under fire. They provide a deep insight into complex physical and chemical processes behind spalling phenomenon from different perspectives. A brief summary of some spalling models is presented in Table 2.8. These spalling models were developed based on different spalling theories mentioned in Section 2.3.1. Previous works on spalling model covered a wide range of topics, from formulation of governing equations to determination of input parameters and spalling criterion, from validations of spalling model to investigations of influence of different factors, such as moisture content of concrete, concrete permeability, heating rate, and influence of reinforcement, etc. They enrich the numerical tools to assess concrete spalling risk in the preliminary design stage and provide valuable solutions to mitigate fire-induced spalling based on their analysis.

To develop a spalling model, it is important to select a spalling mechanism. As mentioned in Section 2.3.1, the spalling mechanism is still a controversial topic. In this sense, it is necessary to work out the spalling mechanism first prior to establishing a spalling model. Moreover, some of the proposed spalling models had not been validated against the experimental results, and some need complex

input parameters, which are difficult to obtain from tests. So there is still a need to

develop a simple and yet effective spalling model that can be validated by

published test results.

Table 2.8 A brief summary of some spalling models

Authors	Spalling mechanism	Dimension	Validation of pore pressure	Validation of moisture content	Validation of thermal stress	Validation of spalling
Bažant et al. (1982)	Pore pressure	2D	√	√		
Majumdar et al. (1995)	Pore pressure	2D				
Gawin et al. (1999)	Pore pressure	2D				
Khoury et al. (2002)	Pore pressure	2D	√			
Ichikawa and England (2004)	Pore pressure	1D	√	√		
Qian et al. (2005)	Pore pressure	1D				
Chung and Consolazio (2005)	Pore pressure	2D	√			
Zeiml et al. (2006)	Pore pressure	1D				
Bary et al. (2008)	Pore pressure	2D	√			
Dwaikat and Kodur (2009)	Pore pressure	1D	√			√
Li et al. (2010)	Pore pressure	1D				
Fu and Li (2011)	Thermal stress	2D				
Davie et al. (2012)	Pore pressure	2D	√			
Klingsch (2014)	Pore pressure	1D				

Zhao et al. (2014)	Thermal stress	2D		√
Lu and Fontana (2015)	Combined pore pressure and thermal stress	1D		√
Beneš and Štefan (2015)	Combined pore pressure and thermal stress	1D	√	√
Ju et al. (2016)	Thermal stress	3D		√

2.5 Current codes of practice

2.5.1 Fire resistance of DFRCC

Eurocode 2 (Institution 2004) and ACI (2007) do not cover fire resistance of DFRCC. JSCE (2008) assumes that fire resistance of DFRCC is similar to ordinary mortar or concrete. However, the guideline (JSCE 2008) mentions that careful examination is needed for structures that should avoid a rapid strength reduction after fire because of melting of fibers under fire action. Therefore, there is a lack of experimental data on high-temperature mechanical properties of DFRCC to support the establishment of specific codes on fire resistance design of DFRCC. Also, there is a need to find a way to overcome the weakness of DFRCC brought by the melting of fibers.

2.5.2 Concrete spalling in fire

Eurocode 2 (Institution 2004) gives some guidance under which situations concrete are more prone to explosive spalling. It also provides some measures to

minimize explosive spalling in fire. But the spalling mechanism is still unclear, and the normative provisions in the code are rather limited and lack theoretical support.

Eurocode 2 (Institution 2004) states that no spalling tends to occur if the moisture content is below 3.0% by weight for normal strength concrete (NSC). For beams, slabs, and tensile members, if the moisture content exceeds this amount, the effect of explosive spalling may be evaluated by assuming local peeling off of cover to one rebar or a bundle of rebars in the cross section. Based on the spalled concrete section, the load-carrying capacity is re-evaluated. In reality, spalling is influenced by many factors such as axial compression load ratio, heating rate, etc. This simple prediction of spalling given in the code is a good start, but more realistic prediction of spalling is preferred.

In Eurocode 2, recommendations are given for two ranges of HSC (Institution 2004). For concrete grades C55/67 to C80/95, spalling is less likely to occur if the silica fume content does not exceed 6.0% of the total weight of cement in addition to satisfying the moisture content condition of less than 3%. For a concrete class between the strength grade of C80/95 and C90/105, four different countermeasures are provided to combat spalling. These measures include adding reinforcement mesh, using spalling-resistant concrete, adopting protective layers, and adding polypropylene fibers. For the selection of methods, one can refer to the National Annex. Although EN 1992-1-2 claims that concrete with silica fume less than 6% of cement by weight is unlikely to spall under fire, reported tests were not in favor of this conclusion (Debicki et al. 2012, Ozawa et al. 2012). So this clause may cause un-conservative design of concrete structures in fire.

Eurocode avoids dealing with spalling predictions, i.e. when and where spalling tends to occur, but provides some recommendations to prevent explosive spalling. ACI (2007) does not give any specifications on fire-induced concrete spalling. In

general, there is much work to be done to supplement the provisions of fire-induced concrete spalling.

2.6 Problem and knowledge gap

Previous research contributes to the knowledge of residual mechanical properties of DFRCC after subjected to elevated temperatures, thermal properties of DFRCC at room temperature, and fire-induced concrete spalling. However, there are still many problems and knowledge gaps concerning fire performance of DFRCC and fire-induced concrete spalling.

Based on the literature review, the problems and the knowledge gaps within the research scope of this thesis are summarized here.

- PVA fibers used in DFRCC melt at about 240 ℃. This means DFRCC will completely lose all the PVA fibers after exposure to 240 ℃ and beyond. As a result, tensile strain hardening behavior of DFRCC will also disappear. Besides, pyrolysis of PVA fibers will introduce additional porosity. Usually 2% vol. PVA fibers are used in DFRCC, which means at least 2% porosity is generated after pyrolysis of PVA fibers. Although the porosity increase can mitigate spalling, it will also reduce residual compressive strength and elastic modulus of DFRCC. Previous studies focused primarily on mechanical properties of DFRCC after exposure to high temperatures, as reviewed in Sections 2.2.1 to 2.2.3. However, little effort is dedicated to improving mechanical properties of DFRCC after or at high temperatures.

- Although DFRCC is well-known by its tensile behavior, compressive behavior of DFRCC is important for analysis and design of DFRCC structures. A better understanding of residual compressive behavior of DFRCC is crucial for wide adoptions of DFRCC in structural engineering. So far, the residual compressive stress-strain relationship of DFRCC after elevated temperature

has not been studied extensively, compared to residual tensile stress-strain relationship.

● As reviewed in Section 2.2.4, no specific test has been designed to study the risk of explosive spalling of DFRCC in fire, not to mention hot permeability of DFRCC. Hot permeability of DFRCC is a critical factor in the assessment of fire spalling risk of DFRCC. In addition, hot permeability of DFRCC is also an indicator of the role of PVA fibers in combating spalling. Therefore, it is important to conduct an experimental program to examine spalling resistance of DFRCC and to measure permeability of DFRCC at elevated temperature.

● Little is done on thermal properties of DFRCC at high temperature as mentioned in Section 2.2.6. Thermal properties of DFRCC are important parameters in thermo-mechanical analysis of DFRCC members under fire. Data on high-temperature thermal properties of DFRCC is needed for establishing analytic thermal property models of DFRCC.

● In the past several decades, researchers proposed mainly three distinct concrete spalling theories and supported their spalling theories with experimental facts and evidences. However, there is still controversy over the actual spalling mechanism. Finding out the underlying principles behind spalling phenomenon becomes especially important for tailoring spalling-free concrete so as to design concrete structures with better fire resistance. More work should be done to gain an insight into the mechanism of fire-induced spalling in concrete.

● As presented in Section 2.3.2, five different hypotheses have been put forward to explain the role of polymeric fibers in reducing explosive spalling. But till now no research has been conducted to find the actual mode of action of PVA fibers in combating explosive spalling of DFRCC.

- Quite a number of numerical models (Table 2.8) have been proposed to simulate fire-induced concrete spalling so far. However, these models were based on different concrete spalling mechanisms. Appropriateness of a spalling model largely depends on the rationality of the assumed spalling mechanism. Since there has not been a widely-acceptable spalling mechanism, development of an effective spalling model remains a challenge. Besides, among the proposed spalling models, some require input parameters that are difficult to be measured in a laboratory and some have not been validated against test results. Therefore, there is still a need to develop spalling models, simplified or refined, to predict spalling behavior of concrete elements under fire.

2.7 Scope of work

Based on the problems and knowledge gaps summarized in Section 2.6, the scope of research work is defined to tackle the existing problems and fill the knowledge gaps.

- To offset the negative influence induced by melting of PVA fibers, steel fibers are introduced to DFRCC. Then Taguchi approach combined with utility concept is used to optimize the mix parameters to maximize mechanical responses of DFRCC prior to fire, as well as after fire. This work is described in CHAPTER 3.

- Uniaxial compressive and tensile behaviors of the improved DFRCC after elevated temperatures are investigated in CHAPTER 4. SEM, DIC techniques, and micromechanical model for achieving pseudo strain-hardening are used to achieve a better understanding of the change in mechanical behaviors of DFRCC with elevated temperature.

- Conflicting and consistent findings in previous studies on fire-induced concrete spalling are summarized and analyzed in CHAPTER 5. Through the analysis, a new spalling theory is proposed to explain fire-induced spalling phenomenon. The temperature range within which spalling occurs, the factors that influence spalling, and preventive measures against spalling are discussed. A new design philosophy to protect concrete from fire spalling is advanced based on the new spalling theory.

- Explosive spalling resistance of DFRCC is studied at elevated temperature. Residual porosity and hot permeability of DFRCC within the critical spalling temperature range are measured. The mode of action of PVA fibers in combating explosive spalling of DFRCC is discussed. The experimental program is presented in CHAPTER 6.

- A simple one-dimensional spalling model is developed in CHAPTER 7 to serve as an economic tool to assess explosive spalling risk of concrete. Effectiveness of the spalling model is validated by simulating three types of tests, i.e., moisture migration test, pore pressure test and one-dimensional spalling test.

CHAPTER 3. OPTIMIZATION OF POST-FIRE PERFORMANCE OF DFRCC

3.1 Introduction

 A number of studies have been conducted to better understand residual mechanical properties of fire-damaged DFRCC as mentioned in CHAPTER 2. However, no efforts have been devoted to improve post-fire performance of DFRCC. There is also a lack of understanding of effect of different mix parameters on post-fire performance of DFRCC. The target of the work presented in this chapter was (a) to examine the effects of different mix parameters on residual properties of DFRCC after subjecting the specimens to elevated temperatures and (b) to optimize the DFRCC mix parameters based on multiple responses of fire-damaged DFRCC.

To get an optimal mix design fulfilling specific performance requirements, a large number of trial experiments are needed. Hence, it is important to design an experimental program to investigate the influences of design parameters involving multiple factors. In this connection, Taguchi method (Chaulia and Das 2008) has shown to be a powerful approach to study the effects of various parameters on the quality characteristics of a product and to optimize single quality characteristic response. Taguchi method has been successfully used to optimize compressive strength, splitting tensile strength of various types of concretes (Karahan et al. 2009, Ozbay et al. 2009, Ayan et al. 2011, Chang et al. 2011, Uysal 2012) and post-fire mechanical properties of concretes (Keleştemur et al. 2014, Tanyıldızı 2014, Tanyildizi and Şahin 2015). Since the method is only suitable for singe-response optimization, utility concept is introduced for multiple-responses optimization (Kumar et al. 2000). It has been applied by Rahim et al. (2013) to optimize multiple

responses of compressive strength of high performance concrete after subjecting to high temperatures.

Cement, fly ash, water, sand, and PVA fibers are common ingredients used in DFRCC (Lepech and Li 2009, Şahmaran et al. 2009), and hence in this study, the selected parameters of DFRCC to be optimized included fly-ash/binder ratio, water/binder ratio, sand/binder ratio and steel/PVA fiber proportion. The steel fibers were introduced to partially replace PVA fibers to study the contribution of steel fibers to fire resistance of DFRCC. Targets of optimization consisted of six responses, viz. tensile strain capacity and compressive strength at room temperature, and compressive strength after undergoing 200, 400, 600, and 800 ℃ of heating. The optimum levels of the selected four parameters for each of the six responses were then determined respectively. Combining Taguchi approach with utility concept, the optimum levels of the four parameters for the six responses could be determined so that the developed DFRCC has good performance for ductility at ambient temperature and adequate compressive strength after heating. Current research work on DFRCC is either focused on ambient behavior or fire behavior of DFRCC separately. It is important to investigate the responses of DFRCC so as to obtain an overall good performance of DFRCC at both fire and ambient conditions.

3.2 Materials and method

3.2.1 Materials

The materials used for DFRCC include ordinary Portland cement (42.5N) conforming to Institution (2000), Class F fly ash corresponding to ASTM 618 (2003), fine silica sand, tap water, steel fibers, PVA fibers and high-range water reducer. Particle size distributions of cement, fly ash and silica sand are shown in Fig. 3.1. An oiling agent content of 1.2% by weight was applied to the surface of PVA fibers for good interfacial properties between the matrix and the fibers. The

chemical compositions of cement and Class F fly ash are given in Table 3.1. Specifications of the PVA and steel fibers are given in Table 3.2 and Table 3.3, respectively. For all the mix designs, total fiber volume fraction was set to be 2%, considering workability at the fresh state of DFRCC. The third generation polycarboxylic-type superplasticizer Sika ViscoCrete-2044 was used in all DFRCC mixes.
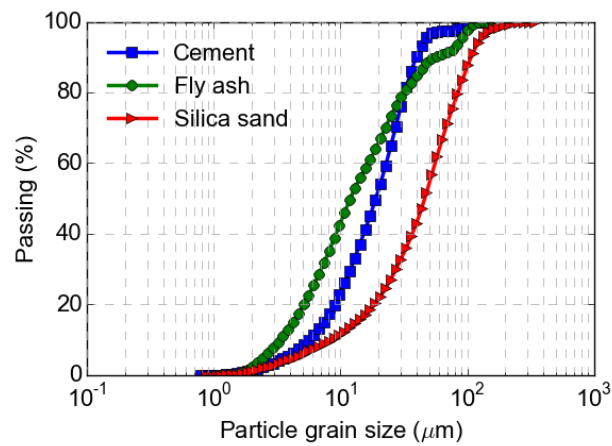
Fig. 3.1 Particle size distributions of cement, fly ash and silica sand

Table 3.1 Chemical compositions of cement and fly ash

Chemical composition	Cement	Fly ash
SiO_2, %	24.27	58.59
Al_2O_3, %	4.56	30.44
Fe_2O_3, %	3.95	4.66
TiO_2, %	0.61	2.02
K_2O, %	0.55	1.51
CaO, %	62.2	1.21
MgO, %	3.34	0.78
P_2O_5, %	0.15	0.53
SO_3, %	-	0.09
Na_2O, %	0.21	-

Table 3.2 Specification of PVA fibers	
Fiber	PVA
Tensile strength, MPa	1620
Diameter, μm	38
Length, mm	12
Elastic modulus, GPa	42.8
Elongation, %	6.0
Density, kg/m^3	1300
Melting temperature, ℃	240

Table 3.3 Specification of steel fibers	
Fiber	Steel
Tensile strength, MPa	2000
Diameter, μm	160
Length, mm	13
Elastic modulus, GPa	200
Shape	Straight
Density, kg/m^3	7800
Melting temperature, ℃	1370

3.2.2 Design of experiments

The experimental program was designed following Taguchi method and utility concept. The selected parameters and their respective levels are given in Table 3.4. Since four parameters with three levels each were involved, only 9 trial experiments were needed to investigate the entire experimental parameters using the L9 (3^4) orthogonal array. The nine DFRCC mix proportions determined by L9 orthogonal array are given in Table 3.5. The multiple-characteristics optimization procedure using Taguchi method and utility concept is summarized in Fig. 3.2.

Table 3.4 Parameters and their variation levels

	Parameters			
Levels	Fly-ash/binder mass ratio (A)	Sand/binder mass ratio (B)	Water/binder mass ratio (C)	Fiber proportion (steel/PVA fibers) (D) (by volume)
1	0.45	0.25	0.28	0.0%/2.0%
2	0.55	0.35	0.32	0.5%/1.5%
3	0.65	0.45	0.36	0.8%/1.2%

Table 3.5 Mix Proportions of DFRCC*

Mix name	Cement	Fly ash	Sand	Water	PVA fiber	Steel fiber	Superplasticizer
M1	1	0.82	0.46	0.51	2%	0.00%	0.009
M2	1	0.82	0.64	0.58	1.50%	0.50%	0.005
M3	1	0.82	0.82	0.66	1.20%	0.80%	0.003
M4	1	1.22	0.56	0.71	1.20%	0.80%	0.005
M5	1	1.22	0.78	0.8	2%	0.00%	0.004
M6	1	1.22	1	0.62	1.50%	0.50%	0.011
M7	1	1.86	0.72	1.03	1.50%	0.50%	0.003
M8	1	1.86	1	0.8	1.20%	0.80%	0.012
M9	1	1.86	1.29	0.92	2%	0.00%	0.006

* Content of fibers is written as volume fraction of the mix, while the other ingredients are written as mass proportion of cement.
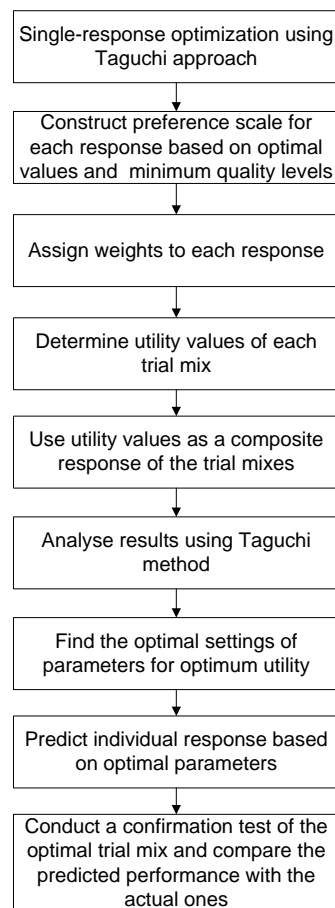
Fig. 3.2 Flowchart of systematic approach to application of Taguchi method and utility concept

3.2.3 Specimen preparation

To prepare the DFRCC specimens, cement, fly ash, and sand were dry mixed for 5 minutes in a Hobart mixer. Then water and superplasticizer were added and mixed for 5 minutes to achieve good workability. After that, PVA fibers and steel fibers were added slowly into the fresh mixture in sequence. Mixing was continued for 3 more minutes to ensure a uniform distribution of fibers.

Fresh DFRCC was poured into molds layer by layer and vibrated to get air bubbles out. After finishing casting, plastic sheets were used to cover the molds to prevent moisture evaporation. After 1 day of curing, the specimens were demolded and sealed in plastic sheets for 6 days, and then stored at ambient condition until 28 days for laboratory testing.

Dog-bone specimens were prepared for uniaxial tensile tests to characterize the tensile stress-strain constitutive relationships of DFRCC mixes. A typical specimen had a straight rectangular section (48 mm $\times$ 13 mm) with a length of 120mm (Fig. 3.3). Cube specimens (50mm) were also prepared for compressive strength tests of DFRCC at ambient and elevated temperatures. From each DFRCC mix, three specimens were prepared for measurements of tensile strain, compressive strength at ambient condition, and residual compressive strength after 200, 400, 600, and 800 ℃ of heating, respectively.
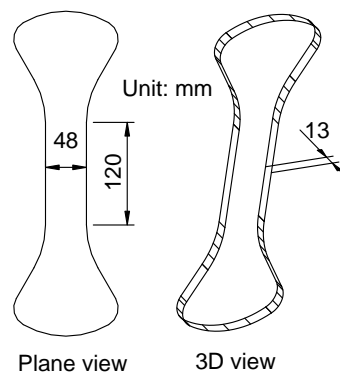
Fig. 3.3 Specimen geometry used in the assessment of tensile stress-strain curve

3.2.4 Test setup

Tensile tests were conducted using an Instron machine. Displacement-control loading regime was adopted and the loading rate was set to 0.2 mm/min. Two linear variable displacement transducers (LVDTs) were attached to the specimen surface with a gauge length of 100 mm to measure deformations. Compressive tests were conducted using a 3000 kN universal testing machine at a load velocity of 50 kN/min. The maximum force applied was recorded by a data acquisition machine. Details of the set-up for tensile tests and compressive tests are shown in Fig. 3.4 and Fig. 3.5(a), respectively. The specimens for the fire tests were heated in an electric furnace (Fig. 3.5(b)) to the target temperature at a heating rate of 10 ℃/min. The target temperature was maintained for 2 hours to allow the cubes to attain isothermal condition before cooling down. This isothermal state was validated by a recorded temperature history of a test cube heated to 800 ℃. Thermocouples were embedded in the interior core and attached on the surface of the cube. The temperature history during the heating duration is shown in Fig. 3.6. Clearly, after a 2-hour conditioning time, both the interior core and the surface temperatures of the sample attained 800 ℃, showing that the cube was in an isothermal state. After cooling the specimens down to ambient temperature, uniaxial compressive tests were conducted on the cubes.

1: Wedge
2: Dogbone specimen
3: LVDT
4: Instron machine
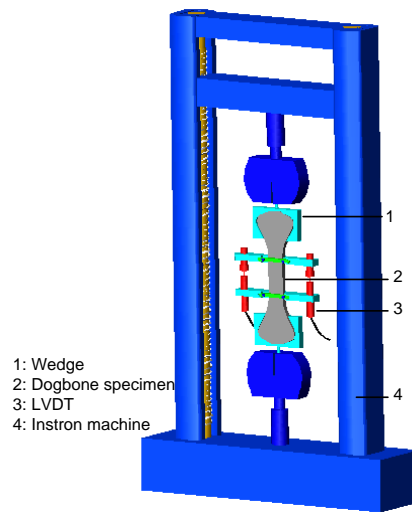
Fig. 3.4 Tensile test configuration

(a) View of a compressive test setup
for compression tests

(b) View of an electric furnace

Fig. 3.5 View of equipments for compression tests and heating
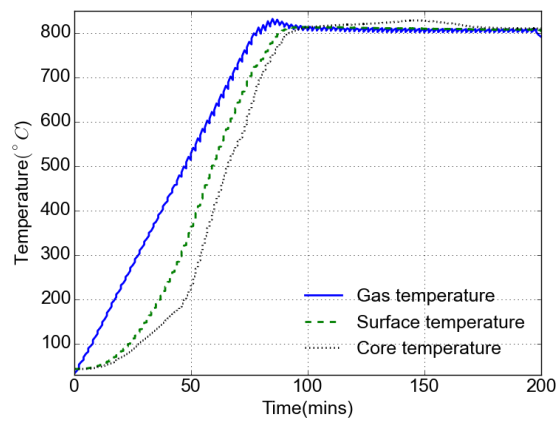
Fig. 3.6 Temperature history of one 50 mm cube

3.3 Results and discussion

Tensile stress-strain curves of the nine DFRCC mixes, i.e., M1-M9, are presented in Fig. 3.7(a)-(g), respectively. The six responses of DFRCC, namely, ultimate tensile strain, compressive strength at ambient and residual compressive strength after 200, 400, 600 and 800 ℃ of heating, are summarized in Table 3.6. The ultimate tensile strain is defined as the strain at softening point according to JSCE recommendation for high-performance cement fiber reinforced cement composites (JSCE 2008). Three specimens were tested for each response and the mean values are listed in Table 3.6.

(a) M1	(b) M2	(c) M3
(d) M4	(e) M5	(f) M6

(g) M7   (h) M8   (i) M9
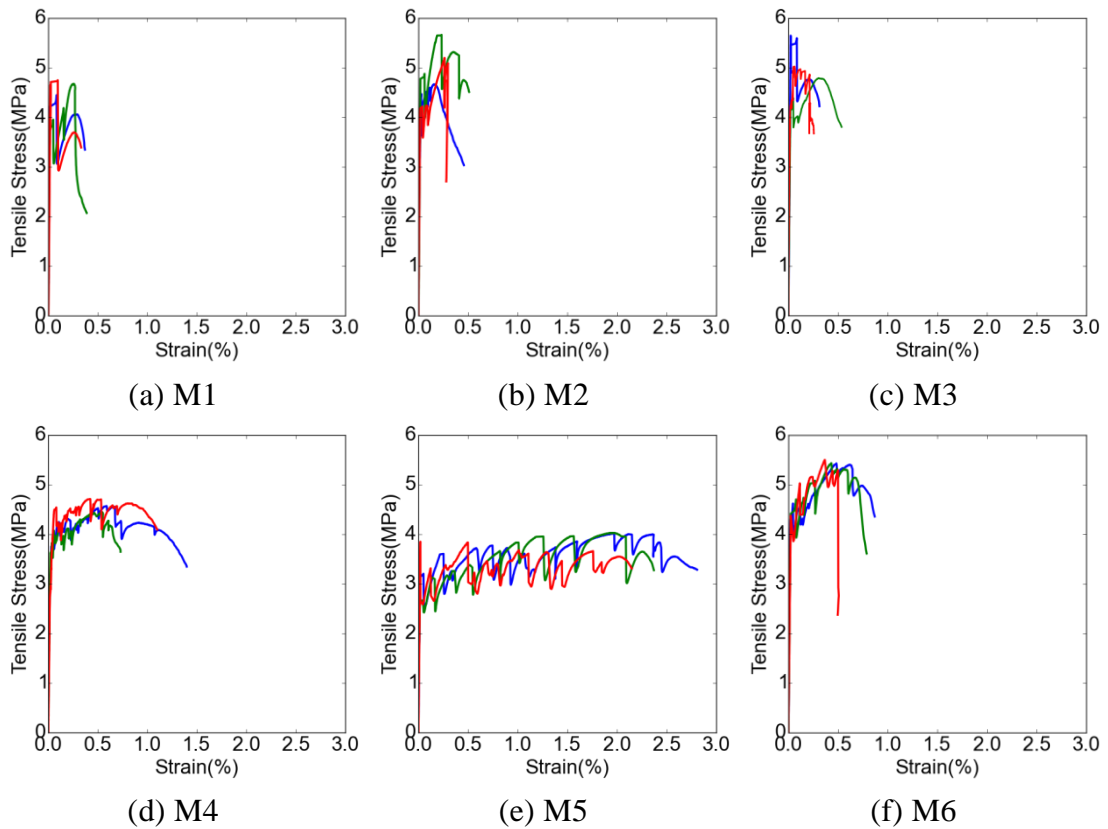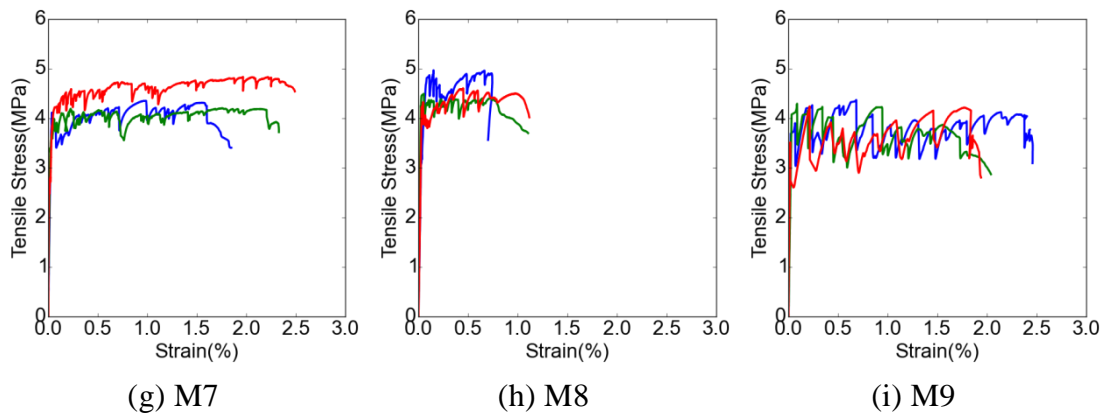
Fig. 3.7 Tensile stress-strain curves of nine DFRCC mixes

Table 3.6 Summary of multiple responses of DFRCC (based on 3 specimens for each value)

Mix name	Ultimate tensile strain (%)	Compressive strength (MPa)				
	Room temperature	Room temperature	200 ℃	400 ℃	600 ℃	800 ℃
M1	0.27	58.3	79.4	69.5	55.9	34.8
M2	0.30	53.1	75.3	45.7	44.0	24.8
M3	0.25	39.0	67.1	54.1	39.9	22.7
M4	0.86	44.7	49.9	48.7	41.1	21.6
M5	2.28	36.8	52.2	34.4	27.6	18.9
M6	0.63	63.9	85.1	65.9	58.9	31.3
M7	2.08	32.7	42.0	33.4	27.1	19.9
M8	0.82	51.0	67.8	59.8	45.7	29.0
M9	2.05	39.4	54.7	38.2	33.1	18.1

3.3.1 Application of Taguchi method

There are three types of quality characteristics for appraising the effects of process parameters, i.e., smaller-the-better, larger-the-better, and nominal-the-better (Chaulia and Das 2008). In this chapter, the objective was to determine the optimum DFRCC mix so as to achieve the maximum response, i.e. to satisfy larger-the-better criterion.

In Taguchi experiments, the trial tests corresponding to the most favorable working condition may be covered during the experimentation process. The optimal performance value can be predicted using the following equation (Roy 2010):

$$Y_{opt} = Y_{mean} + \sum_{j=1}^{n} X_j \qquad (3.1)$$

where Y_{mean} is the overall mean of performance values, and X_j is the fixed effect of jth parameter.

It should be noted that the corresponding confidence interval of optimal value for a chosen error level can be calculated using the following equation (Roy 2010):

$$CI = \sqrt{F(1, f_e)V_e(\frac{1}{N_{eff}} + \frac{1}{R})} \qquad (3.2)$$

where $F(1, f_e)$ is the computed value of F at a desired confidence level (95% in this study), f_e is the error DOF, V_e is the error variance, $N_{eff} = R/(1+f_f)$ is the effective number of repetitions, N is the total number of experiments, R is the number of repetitions for confirmation experiment and f_f is DOF of all factors.

The best possible mix design was selected to maximize the ultimate tensile strain, compressive strength, and residual compressive strength after heating to 200, 400, 600, and 800 ℃ by using Taguchi method. All these six quality characteristics were evaluated based on larger-the-better criterion. The interaction effects of the mix parameters in DFRCC were not considered in this study. The most favorable mix design of the DFRCC could be determined from the main effect plots as shown in Fig. 3.8(a)-(f) for ultimate tensile strain, compressive strength at ambient condition and compressive strength after 200, 400, 600, and 800 ℃ of heating, respectively. The labels of x-axis were defined according to Table 3.4, with A, B, C and D representing fly-ash/binder ratio, sand/binder ratio, water/binder ratio and fiber proportions by column, with numerals 1, 2, 3 representing three levels of

each parameter. Take A1 for example, this DFRCC mix has a fly-ash/binder ratio of 0.45.

From Fig. 3.8(a), the maximum tensile strain capacity was obtained for fly-ash/binder ratio at level A3, for sand/binder ratio at level B2, for water/binder ratio at level C3 and for fiber proportion at level D1. The fly-ash/binder ratio, water/binder ratio, and fiber proportion were the main parameters affecting tensile strain capacity, while sand/binder ratio did not show any significant effect.

It can be observed from Fig. 3.8(b)-(c) that the maximum compressive strength at room temperature and after 200 ℃ was obtained for fly-ash/binder ratio at level A1, for sand/binder ratio at level B3, for water/binder ratio at level C1 and for fiber proportion at level D2. Thus, the main influencing factors were fly-ash/binder ratio and water/binder ratio. The optimum conditions for specimens exposed to 400 ℃ were obtained for fly-ash/binder ratio at level A1, for sand/binder ratio at level B3, for water/binder ratio at level C1 and for fiber proportion at level D3. Thus, Fly-ash/binder ratio and water/binder ratio were also the main parameters affecting compressive strength of DFRCC exposed to 400 ℃ (Fig. 3.8(d)). The optimum conditions at 600 ℃ exposure were reached for fly-ash/binder ratio at level A1, for sand/binder ratio at level B3, for water/binder ratio at level C1 and for fiber proportion at level D2. The water/binder ratio was the main parameter shown in Fig. 3.8(e). The nine trial mixes could maintain about half of their original strength as the temperature increased to 800 ℃, much better than normal concrete (Rahim et al. 2013). The maximum residual strength of DFRCC at this temperature was obtained for fly-ash/binder ratio at level A1, for sand/binder ratio at level B1, for water/binder ratio at level C1 and for fiber proportion at level D2. Again, the water/binder ratio was the main parameter shown in Fig. 3.8(f). The optimum settings of mix parameters and respective optimum performance values calculated using Eqn. (3.1) are included in Table 3.7.

Confirmation tests were done to validate the predicted optimum performance values. The tensile stress-strain curves of DFRCC mix using the optimum set of parameters are given in Fig. 3.9. The mean results of confirmation tests are given in Table 3.7, and they generally fall within the 95% confidence interval of the predicted optimal values.
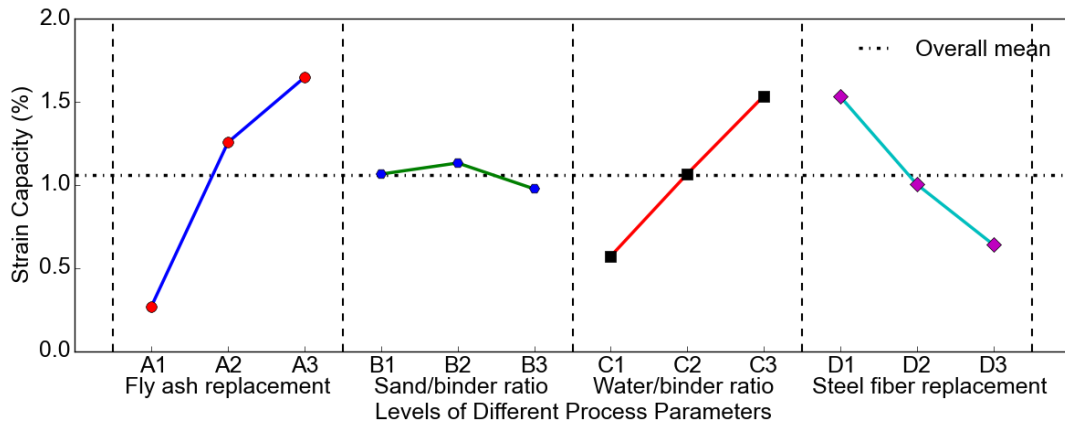
(a) Main effect plot for ultimate tensile strain
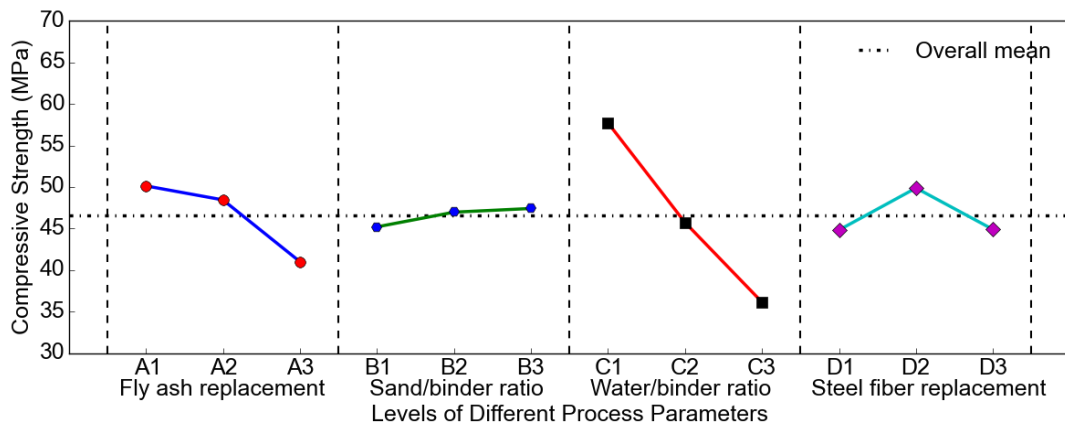
(b) Main effect plot for compressive strength
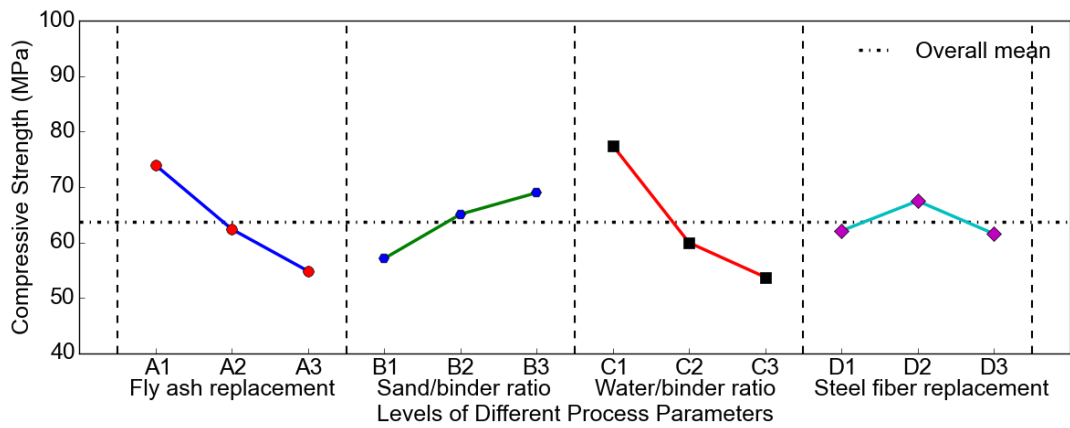
(c) Main effect plot for compressive strength after 200 ℃
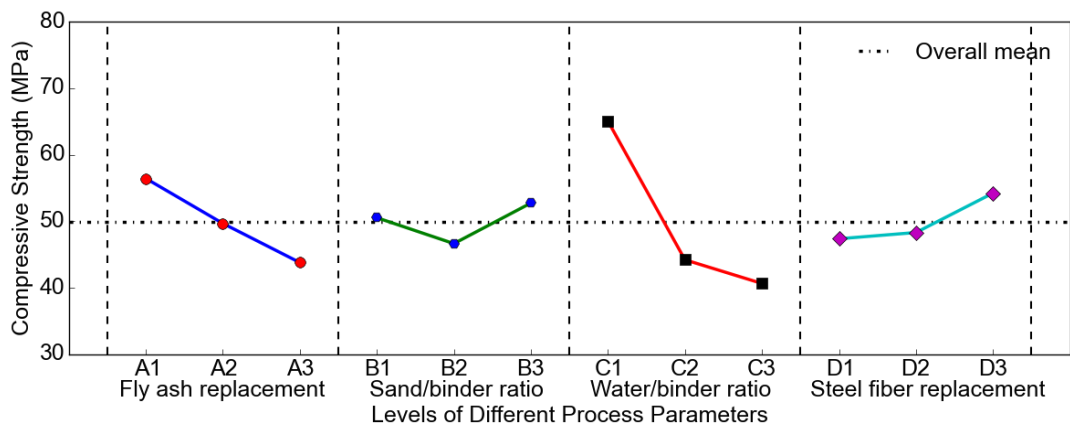
(d) Main effect plot for compressive strength after 400 ℃
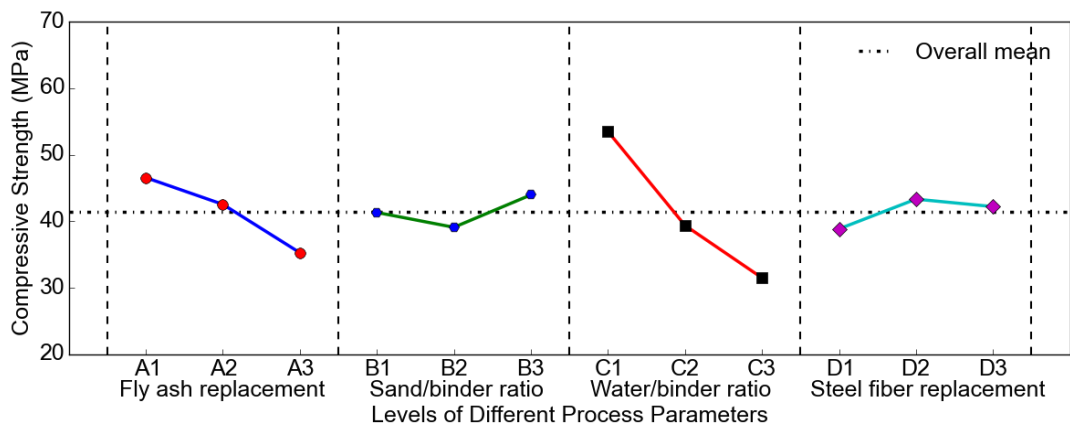
(e) Main effect plot for compressive strength after 600 ℃
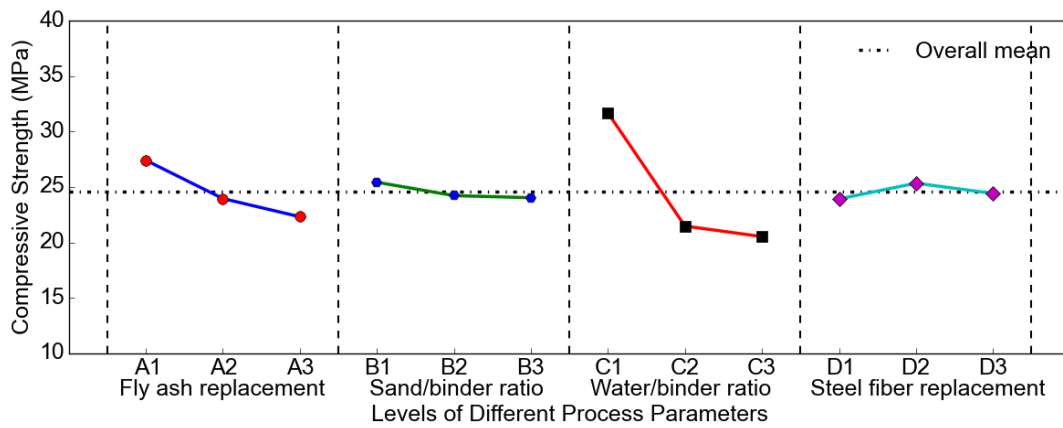
(f) Main effect plot for compressive strength after 800 ℃

Fig. 3.8 Main effect plot for the performance characteristics of DFRCC

Table 3.7 Optimal setting of parameters and optimal performance value

Quality characteristics	Optimum setting of mix parameters	Predicted optimum value	95% confidence interval of predicted optimal value	Mean value of confirmation results
Ultimate tensile strain (%)	A3, B2, C3, D1	2.7	[2.3, 3.1]	2.8
Compressive strength (MPa)	A1, B3, C1, D2	64.6	[59.7, 69.6]	65.8
Compressive strength after 200 ℃ (MPa)	A1, B3, C1, D2	96.7	[90.5, 102.9]	92.6
Compressive strength after 400 ℃ (MPa)	A1, B3, C1, D3	78.5	[73.0, 84.0]	80.8
Compressive strength after 600 ℃ (MPa)	A1, B3, C1, D2	63.0	[59.2, 66.7]	59.1
Compressive strength after 800 ℃ (MPa)	A1, B1, C1, D2	36.1	[32.4, 39.8]	37.3
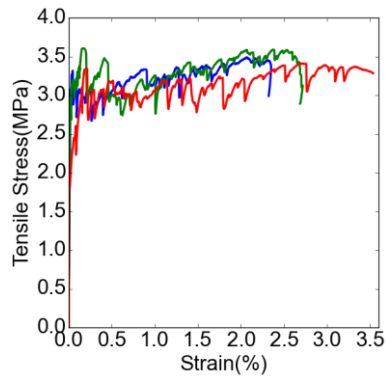
Fig. 3.9 Tensile stress-strain curves of optimal DFRCC mix

3.3.2 Application of utility concept for multiple response optimization

Taguchi approach was used to optimize the six individual responses of DFRCC respectively. From Table 3.7, four different optimum mix proportions were obtained for maximizing different responses. Conventional trial-and-error method would require many more tests to get the optimal set of mix parameters, because there was more than one response to be optimized. The objective of multi-response optimization problem was to find the optimal parameters to optimize multiple responses simultaneously. Taguchi method using utility concept was introduced to optimize the multi-responses of DFRCC mix parameters. Applying the utility concept, a composite index was established to evaluate the overall response of different quality characteristics. This composite index is known as the utility of a product. The overall utility of a product measures the effectiveness of multiple quality characteristics. The utility of a product on one specific characteristic measures the effectiveness of the specific characteristic only. It is assumed that the overall utility of a product is the sum of utilities of each quality characteristic.

So if X_i measures the effectiveness of a quality characteristic i (say tensile strain capacity) and there are n (6 in this case) characteristics assessing the outcome space, then the overall utility function of a product can be written as (Bunn 1982)

$$U(X_1, X_2, \cdots, X_n) = f(U(X_1), U(X_2), \cdots, U(X_n)) \qquad (3.3)$$

where $U(X_i)$ represents the utility of the ith characteristic.

Assuming little interactions among these quality characteristics, and the overall utility function is a linear sum of individual utilities, the overall utility function can then be expressed as

$$U(X_1, X_2, \cdots, X_n) = \sum_{i=1}^{n} W_i U_i(X_i) \qquad (3.4)$$

where W_i is the weight assigned to quality characteristic i and the sum of weights for all characteristics must be equal to 1.

The overall utility is based on individual utility. To determine individual utility, a preference scale is proposed for each attribute of a product. The minimum acceptable value for quality characteristic is assigned a preference number of 0 and the best available quality is set at a preference number of 9. Given that a log scale is chosen, the preference number of (P_i) is written as (Bunn 1982)

$$P_i = A \log \frac{X_i}{X_i^{'}} \qquad (3.5)$$

where A is a constant, X_i is the value of ith quality characteristic and $X_i^{'}$ is the minimum acceptable value of the ith quality characteristic. Then A is determined such that the preference number is equal to 9 when X_i is equal to the optimum value of quality characteristic i.

In this study, there are six characteristics for evaluation. Thus, the utility value of the composite responses against each trial condition and for each repetition is calculated using the following equation (Bunn 1982):

$$U(n,R) = P_1(n,R) \times W_1 + P_2(n,R) \times W_2 + P_3(n,R) \times W_3 + P_4(n,R) \times W_4 +$$
$$P_5(n,R) \times W_5 + P_6(n,R) \times W_6 \tag{3.6}$$

where n is the trial number, n = 1, 2, 3…9 in this case, and R is the replication number, R = 3 in this case. The meaning of P_i and the meaning and values of W_i are tabulated in Table 3.8. Since fire events are accidental design conditions and are rare events, the fire properties of DFRCC were assigned a weight coefficient of 0.1 while the ambient properties of DFRCC were assigned a weight coefficient of 0.3. The weightings of these quality characteristics can be determined according to the actual demand of DFRCC. In the extreme case, for example, the weight coefficients for ambient properties of DFRCC can be 0.5 each, while the weight coefficients for fire properties of DFRCC are 0, if the residual compressive strength after a fire accident is not important.

Table 3.8 Meaning of P_i and the meaning and values of W_i

i	P_i	W_i	
	Meaning	Meaning	Value
1	Preference number for tensile strain capacity	Weight for tensile strain capacity	0.3
2	Preference number for compressive strength at ambient	Weight for compressive strength at ambient	0.3
3	Preference number for compressive strength after 200 ℃	Weight for compressive strength after 200 ℃	0.1
4	Preference number for compressive strength after 400 ℃	Weight for compressive strength after 400 ℃	0.1
5	Preference number for compressive strength after 600 ℃	Weight for compressive strength after 600 ℃	0.1
6	Preference number for compressive strength after 800 ℃	Weight for compressive strength after 800 ℃	0.1

The experimental results of nine trial mixes of L9 (3^4) orthogonal array are summarized in Table 3.6. The minimum acceptable values were chosen based on the experimental results for each individual attribute. The optimum values for each quality characteristic can be found in Table 3.7. A summary of minimum acceptable values and optimum values for each characteristic is given in Table 3.9. The calculated utility data for various trial mixes based on six quality characteristics is presented in Table 3.10.

Table 3.9 Minimum acceptable values and optimal values for characteristics of DFRCC

Quality characteristics of DFRCC	Minimum acceptable value	Optimum value
Ultimate tensile strain (%)	0.1	2.7
Compressive strength (MPa)	30	64.6
Compressive strength after 200 ℃ (MPa)	30	96.7
Compressive strength after 400 ℃ (MPa)	30	78.5
Compressive strength after 600 ℃ (MPa)	20	63.0
Compressive strength after 800 ℃ (MPa)	15	36.1

Table 3.10 Utility data for different DFRCC mixes

Mix name	Utility value			
	Replications			Mean
	1	2	3	
M1	5.93	6.19	6.71	6.28
M2	5.47	4.84	4.75	5.02
M3	3.99	3.69	3.60	3.76
M4	5.17	5.10	4.41	4.89
M5	4.17	4.24	4.52	4.31
M6	7.08	7.17	7.51	7.25
M7	3.81	3.63	3.53	3.66
M8	6.17	6.25	6.01	6.14
M9	4.61	4.68	4.74	4.68

3.3.3 Data analysis and determination of optimal mix proportions

The main effect of utility values for different levels of parameters is given in Table 3.11, respectively. The mean responses of utility values for each level of four parameters are plotted in Fig. 3.10. The figure indicates the second level of fly-ash/binder ratio (0.55), the third level of sand/binder ratio (0.45), the first level of water/binder ratio (0.28) and the second level of fiber proportion (0.5% vol. steel fibers + 1.5% vol. PVA fibers) will give the optimal performance value of the utility function, i.e. overall six quality characteristics of DFRCC. The optimum levels of parameters for achieving multi-responses of DFRCC are presented in Table 3.12. If the weighting factors for fire responses are all set to 0 and for strain capacity and compressive strength at room temperature are assigned 0.5, the optimal levels of mix parameters are A2, B2, C1 and D1 (Fig. 3.11). It means that addition of steel fibers can increase residual compressive strength of DFRCC after fire.

Table 3.11 Main effects of utility values

Level	Fly-ash/cement ratio (A)	Sand/binder ratio (B)	Water/binder ratio (C)	Fiber combination (D)
1	5.02	4.94	6.56	5.09
2	5.49	5.16	4.86	5.31
3	4.82	5.23	3.91	4.93
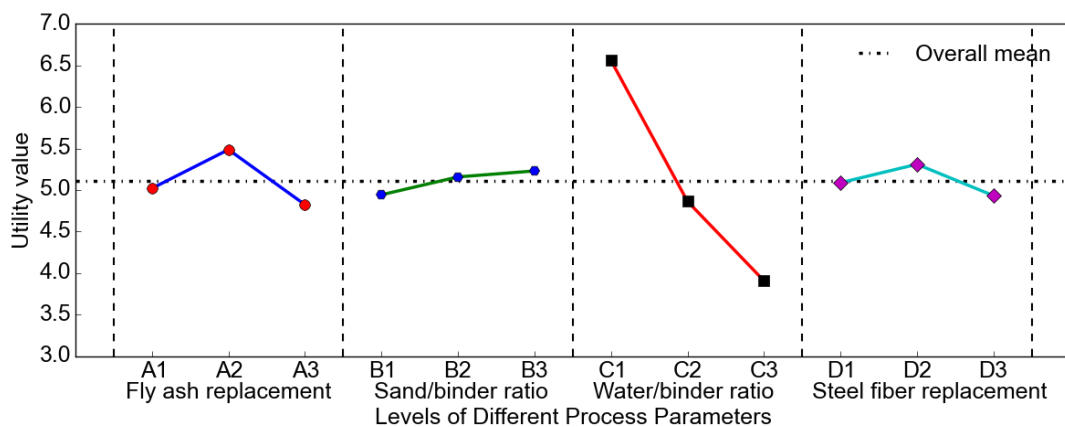
Fig. 3.10 Mean responses of utility values of mix parameters
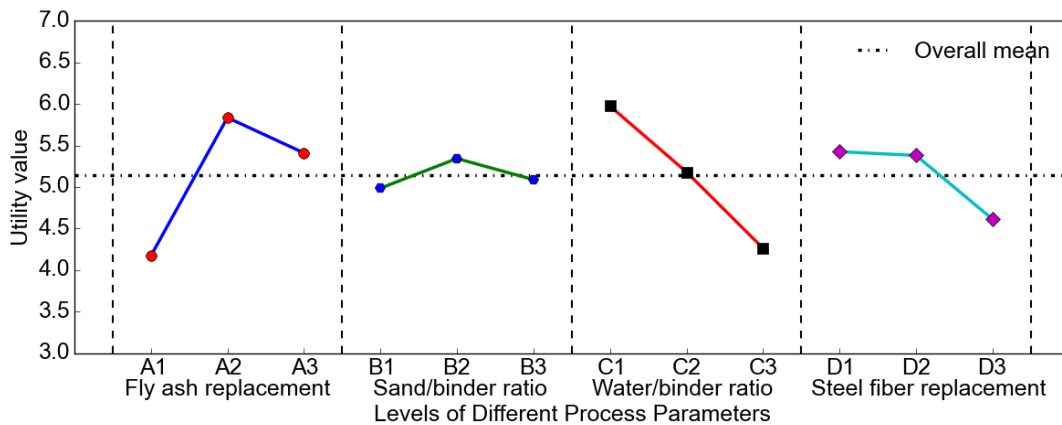
Fig. 3.11 Mean responses of utility values of mix parameters neglecting fire responses

Table 3.12 Optimal setting of parameters for achieving multiple-response optimization

Mix parameter	Level	Value
Fly-ash/binder ratio	A2	0.55
Sand/binder ratio	B3	0.45
Water/binder ratio	C1	0.28
Fiber proportion	D2	0.5% vol. steel fibers + 1.5% vol. PVA fibers

The optimum utility value was predicted at different levels of parameters as shown in the Table 3.12 viz. fly-ash/binder ratio (A2), Sand/binder ratio (B3), Water/binder ratio (C1) and fiber proportion (D2). The predicted mean of the optimum utility value maximized can be calculated as:

$$U_{opt} = U_{A2} + U_{B3} + U_{C1} + U_{D2} - 3U_{mean} \tag{3.7}$$

where U_{mean} is the overall mean of utility value and U_{A2}, U_{B3}, U_{C1}, U_{D2} are respectively utility values at level A2, B3, C1, D2 given in Table 3.12. The corresponding confidence interval was calculated using Eqn. (3.2).

An analysis of variance was conducted to find out relative importance of these four parameters and identify promising direction for future experiments. Fig. 3.12 shows the percentage contribution of the mix parameters on the multiple responses of

DFRCC. As shown clearly from Fig. 3.12, water/binder ratio is of utmost importance for multiple responses of DFRCC. This is because the six responses, i.e. tensile strain capacity, compressive strength, and residual compressive strength after subjecting to 200, 400, 600, 800 ℃ of heating are particularly sensitive to the variations of water/binder ratio. The fly-ash/binder ratio is the second most important factor with 5.6% contribution. The contributions of sand/binder ratio and steel fiber replacement percentage are negligible, since compressive strength, and residual compressive strength after subjecting to 200, 400, 600, 800 ℃ of heating are insensitive to the variations of steel fiber amount and sand/binder ratio.
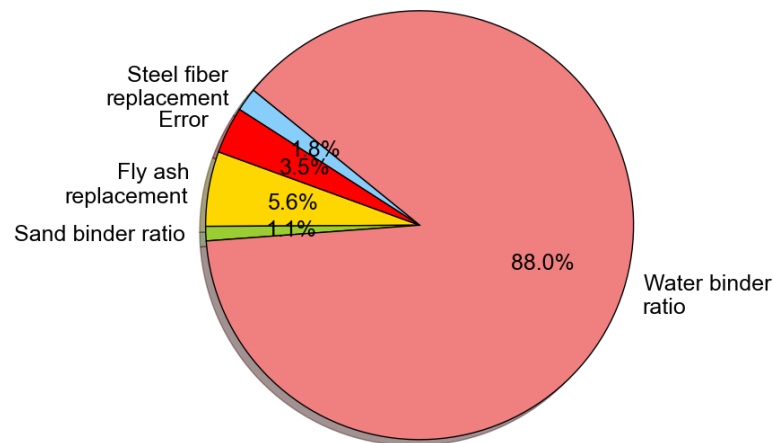
Fig. 3.12 Percentage-contribution of the mix parameters on the utility value of DFRCC

3.3.4 Confirmation experiment

One important aspect of Taguchi approach using utility concept is conducting confirmation tests to validate the predicted results. Usually, the optimal mix proportions are not included in the orthogonal array experiment. In this case, the probability that the optimal mix is within the orthogonal array experiment is 11.1%, since nine out of 81 full factorial conditions in a L9 (3^4) experiment were tried. In this case, the optimal mix happened to be M6. To further validate the finding,

another set of specimens using M6 were cast and tested following the same condition mentioned in Materials and Methods section. The confirmation results and utility values are shown in Table 3.13 and Table 3.14, respectively. The test values are found to fall within the predicted 95% confidence interval of optimal utility value. Fig. 3.14 gives the compressive strengths of nine trial mixes (including the optimal mix) against elevated temperatures. Obviously, the optimal mix, namely M6, had the largest compressive strengths against elevated temperatures in general. At 200 ℃, a strength increase was observed due to pozzolanic reaction under moderate heating. The cubes still had residual compressive strengths of around 35 MPa after exposure to 800 ℃, more than half of its original compressive strength.
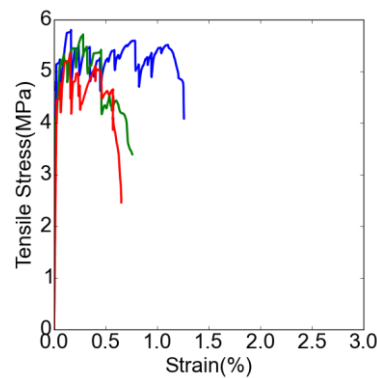
Fig. 3.13 Tensile stress-strain curves of confirmed DFRCC mix

Table 3.13 Confirmation test results

Quality characteristics of DFRCC	Confirmation test results			
	1	2	3	Mean
Ultimate tensile strain (%)	1.1	0.6	0.6	0.8
Compressive strength (MPa)	63.4	63.7	60.6	62.6
Compressive strength after 200 ℃ (MPa)	85.0	82.9	79.0	82.3
Compressive strength after 400 ℃ (MPa)	74.7	70.7	69.4	71.6
Compressive strength after 600 ℃ (MPa)	63.1	56.1	57.6	59.0
Compressive strength after 800 ℃ (MPa)	37.4	39.7	35.8	37.6

Table 3.14 Confirmation test results of utility values

Quality characteristics of DFRCC	Optimal setting of mix parameters	Predicted Optimum value	95% confidence interval of the predicted optimal value	Mean value of confirmation
Strain Room temp. 200 ℃ 400 ℃ 600 ℃ 800 ℃	A2, B3, C1, D2	7.25	[6.79, 7.71]	7.57

Fig. 3.14 Compressive strengths of mix trials against elevated temperature

3.4 Summary

An experimental program was conducted to optimize the mix parameters of DFRCC to maximize combined performance of compressive strength, tensile strain at room temperature and post-fire compressive strength. Based on the results and analysis, specific findings of this research are outlined below.

The Taguchi approach using utility concept is an effective method to optimize multiple responses of DFRCC, i.e. tensile strain capacity, compressive strength, and residual compressive strength after subjecting to 200, 400, 600, 800 ℃ of heating. An optimal DFRCC mix in terms of these six quality characteristics is achieved from 81 possible trial mixes through statistical analysis.

The most influencing parameter for achieving an optimal condition of multiple responses is water/binder ratio with a contribution percentage of 88.0%.

Fly-ash/binder ratio is found to be the second most important factor, followed by fiber proportion and sand/binder ratio. Further optimization of DFRCC can be made according to this finding by varying the level of significant parameters.

With 2% vol. PVA fibers, DFRCC shows the best tensile ductility. However, the overall post-fire performance of this DFRCC mix is not the most favorable. Replacement of 0.5% vol. PVA fibers with steel fibers improves the overall performance in the six quality characteristics.

CHAPTER 4. MECHANICAL PROPERTIES OF

OPTIMIZED DFRCC AFTER FIRE EFFECT

4.1 Introduction

In the previous chapter, an optimized DFRCC mix, which has optimal combined performance of compressive strength, tensile strain at room temperature and post-fire compressive strength, was developed. In this chapter, residual compressive and tensile properties of this optimized DFRCC mix were investigated in detail. Compressive property tests were conducted on DFRCC specimens at 30 ℃ (room temperature in Singapore), and exposed to 200, 400, 600, and 800 ℃. Direct uniaxial tensile tests were conducted on DFRCC specimens exposed to temperature up to 600 ℃ at an increment of 100 ℃. Scanning Electron Microscope (SEM) and Digital Image Correlation (DIC) techniques were employed to examine the morphology of DFRCC materials, fiber state and crack patterns to obtain better understanding of residual mechanical properties. This work sheds more light on residual mechanical behavior of the optimal DFRCC mixture after heating and adds knowledge to positive roles of steel fibers in tensile behavior of DFRCC after melting of PVA fibers.

4.2 Materials and method

4.2.1 Materials

The optimized DFRCC developed in CHAPTER 3 was taken as the research object in this chapter. Its mix proportion is shown in Table 4.1, i.e., mix M6 in Table 3.5. The binder selected was a combination of ordinary Portland cement (42.5 N) conforming to EN 197-1 (2000) and Class F fly ash corresponding to ASTM 618 (2003). The chemical compositions of cement and fly ash are listed in Table 3.1 and

the properties of PVA and steel fibers are listed in Table 3.2 and Table 3.3. Particle size distributions of cement, fly ash, and silica sand are shown in Fig. 3.1. The third generation polycarboxylic type superplasticizer Sika ViscoCrete-2044 was used in the DFRCC mix design.

Table 4.1 Mix Proportions of DFRCC (by mass)

Mix name	Cement	Fly ash	Sand	Water	PVA fiber (by volume)	Steel fiber (by volume)	Superplasticizer
DFRCC	1	1.22	1	0.62	1.50%	0.50%	0.011

4.2.2 Specimen preparation

Cylinder specimens (ϕ100mm$\times$200mm) were prepared for uniaxial compressive tests and 50 mm cube specimens were used for mass loss tests. Dog-bone specimens (see Fig. 3.3) were used for uniaxial direct tension tests. The same procedure as specified in Section 3.2.3 was followed to prepare these test specimens.

4.2.3 Compressive test & mass loss test

Compressive tests were conducted on ϕ100mm$\times$200mm cylinder specimens after exposure to temperature up to 800 ℃ at an increment of 200 ℃. For each temperature exposure, three cylinders were tested. The compressive tests were conducted after at least 28 days. The residual compressive tests were conducted after the specimens were respectively heated to 200, 400, 600, and 800 ℃. The specimens were heated to target temperatures at a heating rate of 10 ℃/min, and then kept at that temperature for 2 h. After that, the specimens were kept in furnace and naturally cooled to ambient temperature. The specimens were loaded to failure at a displacement rate of 0.2mm/min using a hydraulic universal testing machine shown in Fig. 4.1. The measurement system included three 10mm linear variable

displacement transducers (LVDTs) attached onto the center region of the specimen with a gage length of 100mm and two 50mm LVDTs measuring the deformation of the specimen.

The cube specimens used for mass loss tests went through the same heating regime as the cylinder specimens for compressive tests. Prior to and after heating, the masses of the cube specimens were recorded to determine mass loss. Mass loss ratio was calculated using the mass difference of the cube specimen before and after heating normalized by the initial mass of the specimen.

Fig. 4.1 Test setup for compressive test

4.2.4 Tensile test

Uniaxial tensile tests were conducted on specimens after exposure to temperature up to 600 ℃ at an increment of 100 ℃. For each temperature exposure, three specimens were tested and the average value was obtained. Tensile tests at ambient condition were conducted at an age of 28 days, while residual tensile tests were conducted one or two days after subjecting the specimens to a heating rate of 10 ℃/min, and then conditioned for 2 h after reaching the target temperature.

Subsequently, the specimens were allowed to cool down naturally in the furnace. The tensile test setup is given in Fig. 4.2. Prior to testing, a small tension force (maximum 30 N) was applied to eliminate gaps between the specimen ends and the clamping wedges. Two linear variable differential transformers (LVDTs) were attached on both sides of the dog-bone specimen (Fig. 4.2) to record deformations of the straight segment with a 100 mm gage length. Displacement-controlled loading scheme at 0.2 mm/min was used. Tensile force was recorded by a load cell embedded in the Instron machine. A high-resolution digital camera was mounted on a tripod at about 1m in front of the tensile specimen. DIC technique was used for one of the three specimens for each temperature exposure. During the tests, the digital camera was remotely controlled using a tablet computer connected to Wi-Fi to avoid physical contact of the camera. Digital photographs were taken at 10 s interval in the first 2 min and then at 30 s interval to capture the crack pattern until the specimen softened.

The working mechanism of DIC system is based on calculating the differences in light density as a gray-scale pattern at each pixel between subsequent captured photographs (Mauroux et al. 2012). To form the speckle pattern for displacement and strain field analysis, one surface of the specimen was white washed, followed by uniformly spraying random small black spots on it.

1: Wedge
2: Dogbone specimen
3: LVDT
4: Digital camera
5: Instron machine
6: Tripod
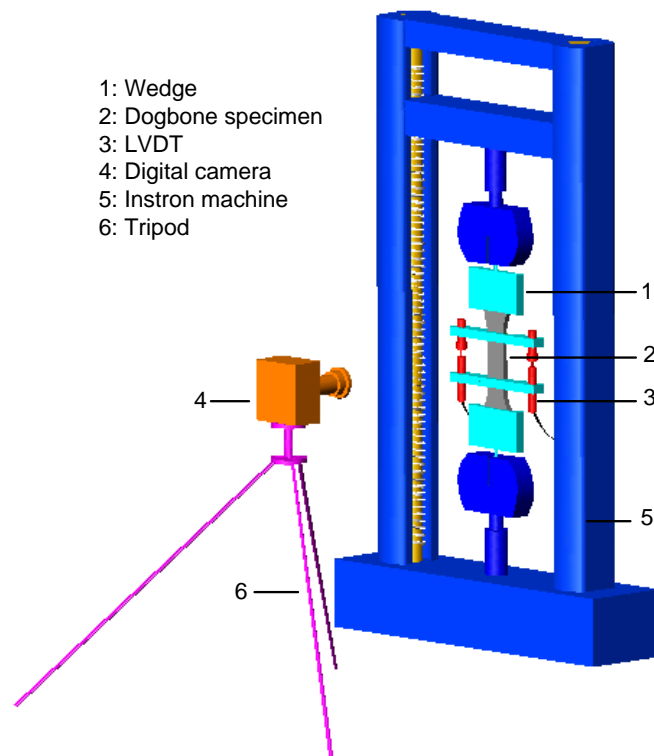
Fig. 4.2 Configuration of uniaxial tensile test setup

4.2.5 SEM observation

Field Emission Scanning Electron Microscope (FE-SEM) was used to observe the microstructure of DFRCC samples. The samples were taken from additional dog-bone specimens heated to 200, 400, 600, and 800 ℃ at 10 ℃/min.

4.3 Results and discussion

4.3.1 Compressive tests

There were no visible cracks on the specimens heated up to 600 ℃. However, some micro-cracks were found on the surfaces of specimens heated to 800 ℃. No spalling of cylinders was observed after heating. Explosive spalling is influenced by the dimensions of specimens (Sanjayan and Stocks 1993, Hertz 2003, Kodur and

Phan 2007). Hence, larger specimens should be prepared specifically for examining the spalling resistance of DFRCC under fire.

Fig. 4.3(a)-(e) shows the typical failure patterns of the DFRCC specimens heated to different temperatures. Different failure modes were observed for specimens exposed to different temperatures. For specimens exposed to 200 ℃, the same failure mode as unheated specimens was observed. The failure pattern was characterized by a major inclined shear crack forming along the height of the specimens with the cracking plane approximately at 80° from the horizontal plane as shown in Fig. 4.3(a) and (b). After heated to 400 ℃ and above, the failure pattern showed multiple interacting cracks as shown in Fig. 4.3(c)-(e). This behavior was expected since a majority of bridging forces between fibers and matrix were lost due to melting of PVA fibers at 240℃. Even though the heated specimens showed different failure patterns, they still exhibited a ductile failure mode as shown by the stress-strain curves shown in Fig. 4.4.
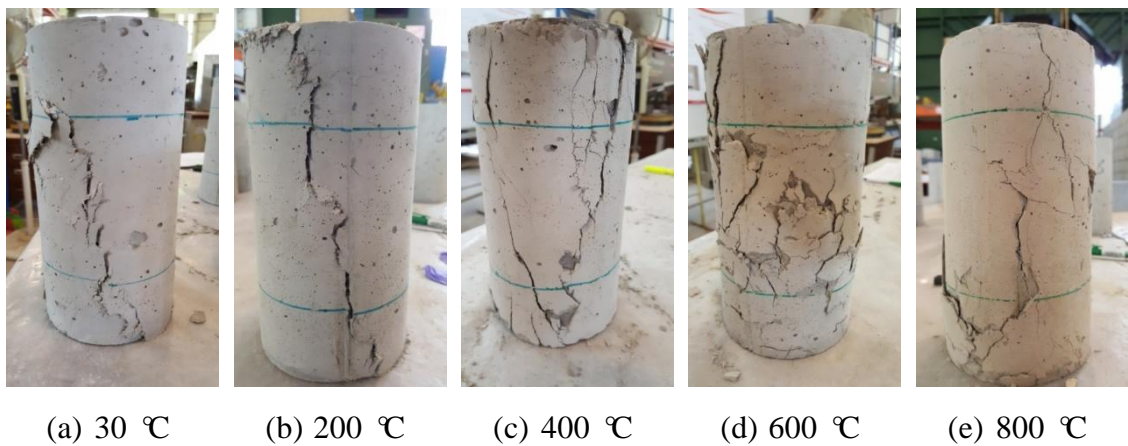
(a) 30 ℃   (b) 200 ℃   (c) 400 ℃   (d) 600 ℃   (e) 800 ℃
Fig. 4.3 Failure patterns of heated DFRCC cylinder specimens

(a) 30 ℃

(b) 200 ℃

(c) 400 ℃

(d) 600 ℃

(e) 800 ℃
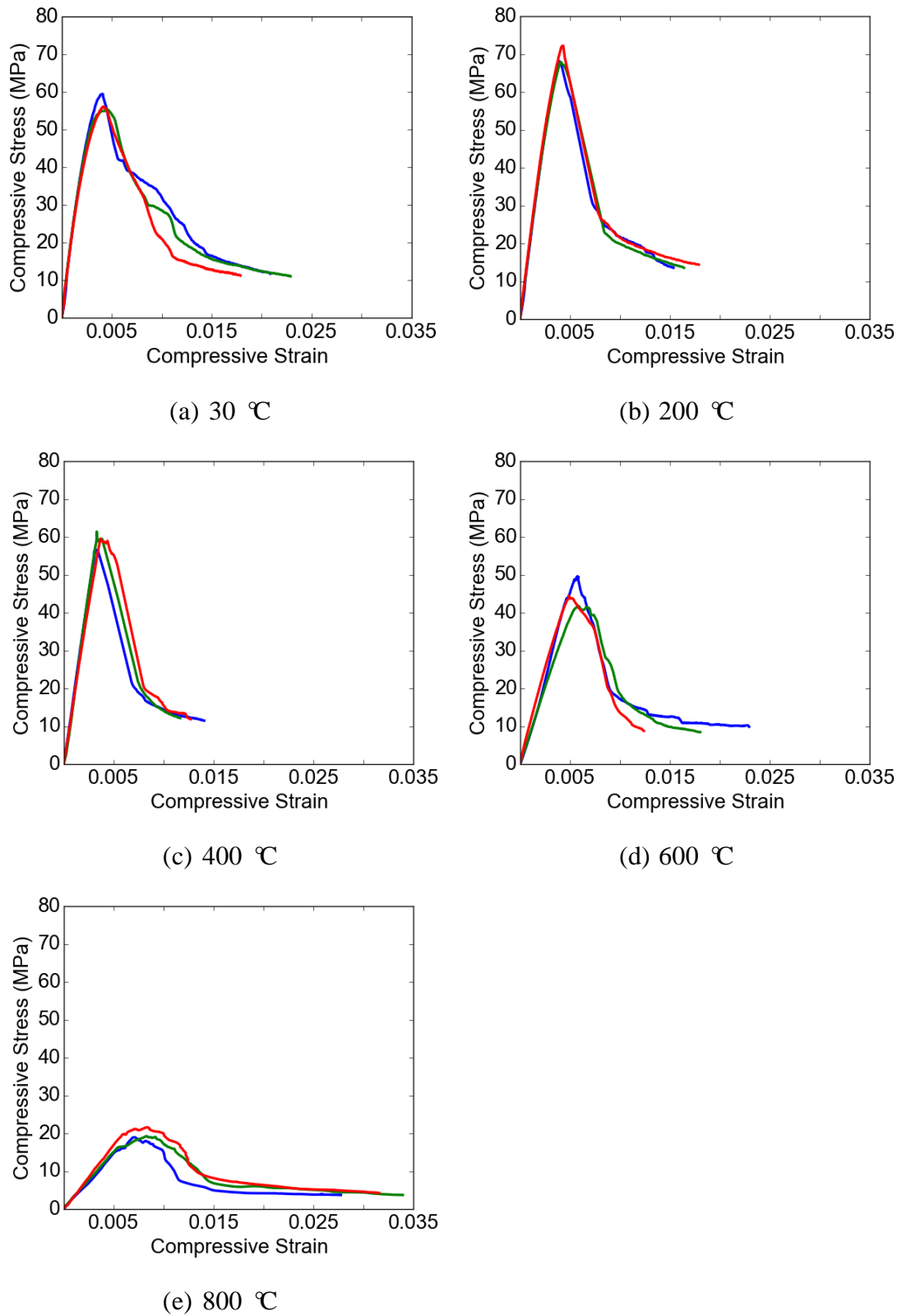
Fig. 4.4 Compressive stress-strain curves of the DFRCC mix at ambient
temperature and after heating to different temperatures

The compressive stress-strain curves of the DFRCC mix at ambient temperature and after heating to 200, 400, 600, and 800 ℃ are given in Fig. 4.4(a)-(e). The compressive strength of DFRCC cylinders was 57.0 MPa as shown in Fig. 4.4(a). After exposure to 200 ℃, the compressive strength increased to 69.4 MPa as shown in Fig. 4.4(b), 12.1% greater than that at ambient. Up to 400 ℃, the residual compressive strength reduced to 59.2 MPa (Fig. 4.4(c)), which was close to its ambient compressive strength, and further reduced to 45.3 MPa after exposure to 600 ℃ (Fig. 4.4(d)). At 800 ℃, the compressive strength of DFRCC suffered a steep drop to 20.0 MPa as shown in Fig. 4.4(e), about 35% of its original strength.

Fig. 4.5 shows the compressive strength reduction coefficients of DFRCC compared to those of siliceous and calcareous concrete specified in Eurocode 2 (Institution 2004). Obviously, DFRCC outperformed normal concrete in terms of compressive strength retention after exposure to temperature up to 800 ℃. At 200 ℃, there is a slight strength decrease for normal concrete, while for DFRCC there is an increase in compressive strength. At 400, 600, and 800 ℃, the compressive strength reduction coefficients are larger than those of normal concrete made from either siliceous or calcareous aggregates (Institution 2004). The significant improvement in compressive strength of DFRCC at 200 ℃ can be explained by pozzolanic reaction between fly ash and calcium hydroxide accelerated by heating at moderate temperature (Mengxiao et al. 2015). The CSH resulting from the pozzolanic reaction fills the micropores and forms a denser microstructure. At 400, 600, and 800 ℃, higher retention of strength may be due to absence of damage induced by thermal incompatibility between cement paste and coarse aggregate as experienced in normal concrete.
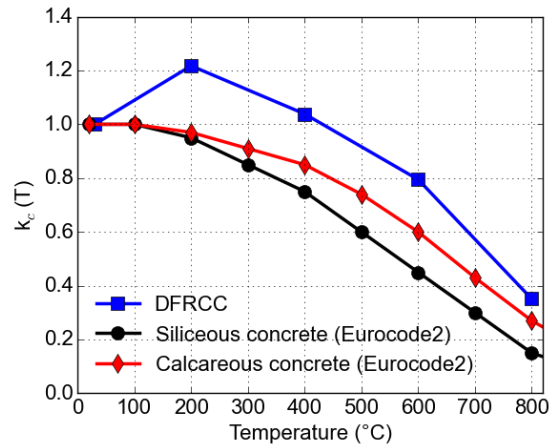
Fig. 4.5 Coefficient k$_c$(T) allowing for decrease of compressive strength at elevated temperatures

Table 4.2 lists the elastic modulus of DFRCC at room temperature and after exposure to 200 ℃, 400 ℃, 600 ℃, and 800 ℃. Fig. 4.7 shows the coefficient k$_E$(T) allowing for decrease of elastic modulus of DFRCC at elevated temperature compared to those of siliceous and calcareous concrete specified in Eurocode 2 (Institution 2004). The elastic modulus is calculated using Eqn. (4.1) according to ASTM C469 (2014).

$$E = (\sigma_2 - \sigma_1) / (\varepsilon_2 - 0.00005) \tag{4.1}$$

where E is elastic modulus, σ_2 is the stress corresponding to 40% of ultimate load, σ_1 is the stress corresponding to a longitudinal strain of 50 millionths, and ε_2 is the longitudinal strain produced by stress σ_2.

Table 4.2 Elastic modulus of DFRCC at room temperature and after exposure to high temperature

Temperature	Elastic modulus
30 ℃	21004 MPa
200 ℃	19838 MPa
400 ℃	17354 MPa
600 ℃	8759 MPa
800 ℃	2770 MPa

As seen from Fig. 4.7, both DFRCC and concrete experience degradation in elastic modulus as temperature increases. However, DFRCC shows a slower reduction trend in elastic modulus than concrete. This is possibly mainly due to that DFRCC has less micro-cracks induced by thermal loading than concrete. DFRCC does not contain coarse aggregates, and is, therefore, not beset with thermal incompatibilities that occur between cement paste and aggregates due to differential thermal volume changes. It was noted in Fig. 4.6 that no microcracks were induced around the perimeter of PVA fiber channels. And according to Lau and Anson (2006), there was no obvious change in residual elastic modulus of concrete with or without steel fibers after exposure to different high temperatures. Therefore, addition of PVA and steel fibers do not have a negative effect on residual elastic modulus of fire-damaged DFRCC.
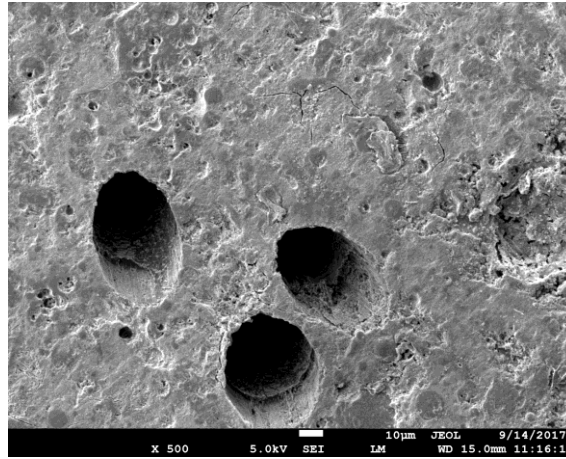
Fig. 4.6 SEM image of DFRCC after PVA fibers melted

At 200 ℃, modulus of elasticity of DFRCC was reduced by 5.5% of those of unheated control specimens. It was further reduced to 82.6% of those of control specimens after heating up to 400 ℃. After heating up to 600 ℃ and above, the modulus of elasticity of DFRCC decreases dramatically. An average of 41.7% of the elastic modulus of the unheated DFRCC was retained after exposure to 600 ℃. After exposure to 800 ℃, it was further reduced to 13.2%. The rapid degradation of elastic modulus is most likely due to the physical changes (increase in porosity, pore coarsening of DFRCC matrix, and cracking density) taking place in the matrix.
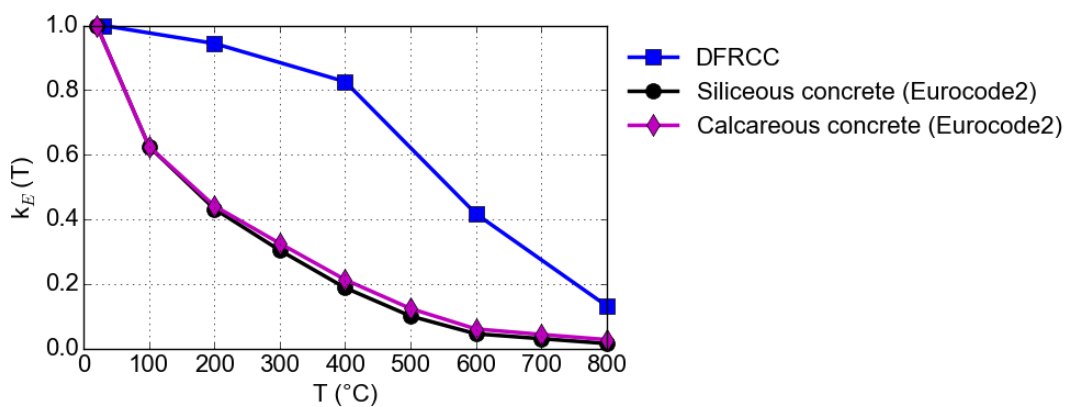
Fig. 4.7 Coefficient $k_E(T)$ allowing for decrease of elastic modulus at elevated temperatures

A typical morphology of DFRCC after exposure to 200 ℃ and 600 ℃ is presented in Fig. 4.8. Micrographs of DFRCC at 200 ℃ consisted of amorphous C-S-H gels and well-crystallized CH crystals as shown in Fig. 4.8(a). At 600 ℃, the crystalline structure of CH was destroyed and the morphology of resultant products showed an amorphous mass structure as shown in Fig. 4.8(b). This matched well with the macro phenomenon that compressive strength of DFRCC specimens decreased from 200 ℃ to 600 ℃.

Fig. 4.9 shows the mass loss of DFRCC and normal concrete as described in Eurocode 2 (Institution 2004) and thermogravimetry (TG) curve of PVA fiber. The TG analysis of PVA fibers was performed with a heating rate of 10 ℃/min, from 30 ℃ to 800 ℃ in nitrogen flow (20 mL/min). To compare the mass loss of DFRCC to that of concrete, the moisture content of DFRCC (4.8%) was deducted as shown in Fig. 4.9. The moisture content of DFRCC was determined by the average mass loss of three DFRCC cube specimens after drying at 105 ℃ for four days. At 200 ℃, the difference between the mass loss of DFRCC (moisture removed) and normal concrete is about 0.5%; at 400 ℃, the difference becomes 0.91%. This increased difference is believed to be caused by decomposition of 1.5% vol. PVA fibers (68% mass lost up to 400 ℃ as seen in Fig. 4.9). However, decomposition of PVA fibers have a limited influence on the mass loss of DFRCC and the mass loss of DFRCC is similar to that of normal concrete in general.

(a) 200 ℃   (b) 600 ℃
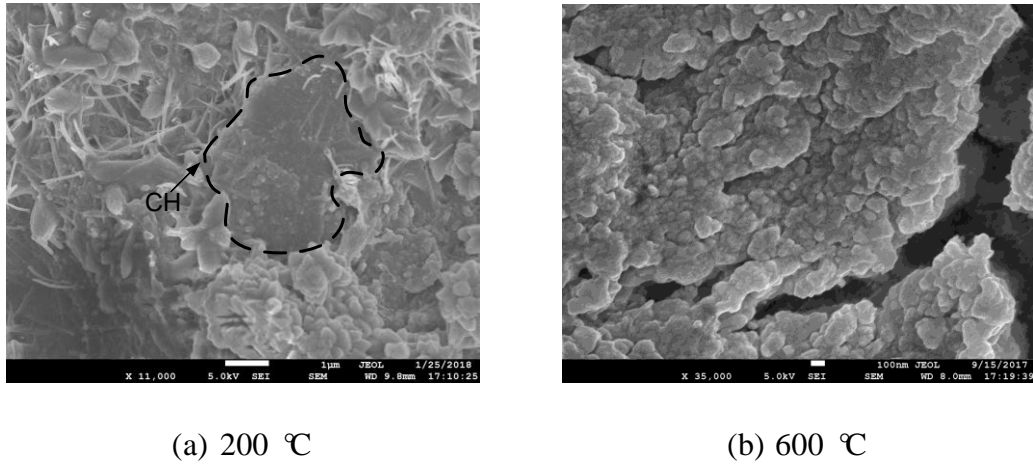
Fig. 4.8 Morphology of DFRCC after heat treatment at 200 ℃ and 600 ℃
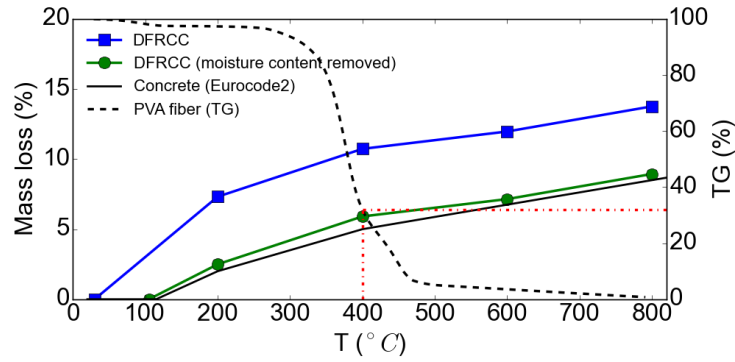
Fig. 4.9 Mass losses at elevated temperatures

4.3.2 Tensile test

Typical tensile stress-strain curves of the DFRCC mixture with hybrid fibers at room temperature are shown in Fig. 4.10. The DFRCC mix (Table 4.1) had an ultimate tensile strength of 5.5MPa and an average strain capacity of 0.8%. Fig. 4.11(a)-(f) give the stress-strain curves of DFRCC specimens after exposure to 100, 200, 300, 400, 500, and 600 ℃, respectively. The DFRCC specimens exhibited tensile strain hardening behavior up to 200 ℃ as seen in Fig. 4.11(a)-(b). However, their tensile strain capacities decreased with temperature increase. At 300 ℃, DFRCC lost its strain hardening feature, and instead showed strain softening behavior as shown in Fig. 4.11(c). After initiation of one crack (characterized by a

sudden drop in the tensile load in the figure), the tensile load was carried by the friction bond between steel fibers and matrix across the cracked section. At 400, 500, and 600 ℃, DFRCC lost the strain softening feature and showed similar behavior to normal concrete as shown in Fig. 4.11(d)-(f). The friction bond between steel fibers and matrix was too small to carry any tensile load. It is noteworthy that from 300 ℃ onwards the strain corresponding to peak tensile stress increased slightly as temperature increased. This was caused by degradation of tension stiffness of DFRCC resulting from different degrees of thermal decomposition.
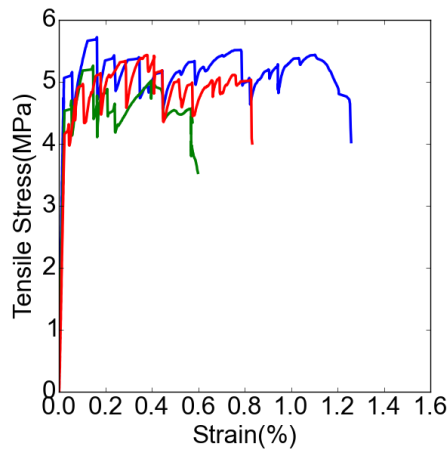
Fig. 4.10 Tensile stress-strain curve of the DFRCC mix at ambient temperature

(a) 100 ℃

(b) 200 ℃

(c) 300 ℃   (d) 400 ℃

(e) 500 ℃   (f) 600 ℃
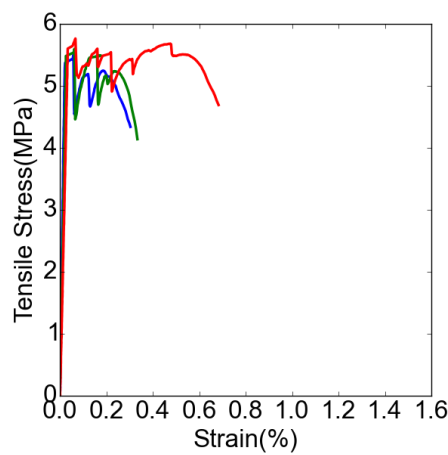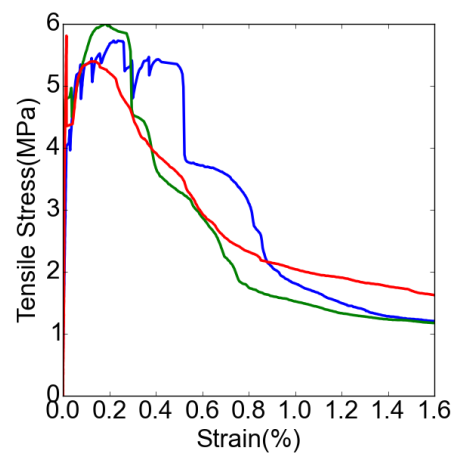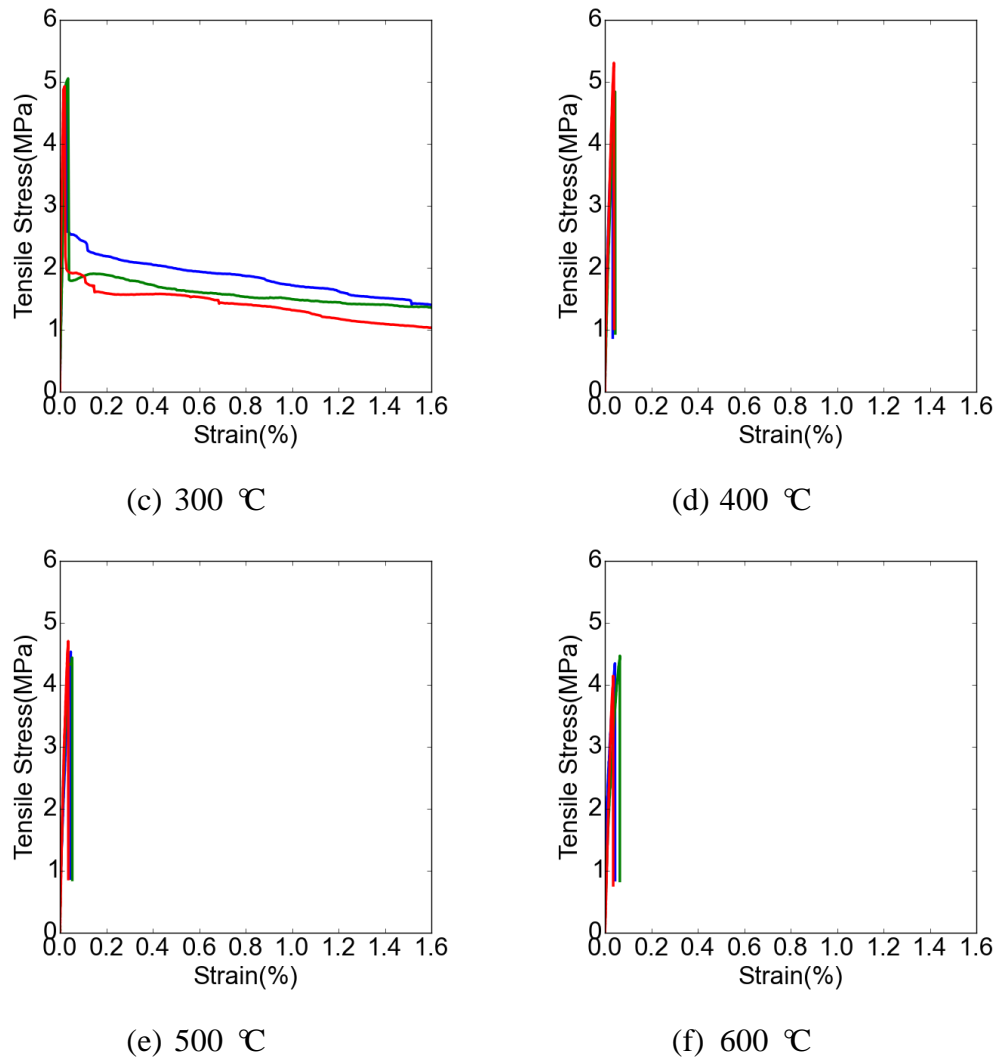
Fig. 4.11 Tensile stress-strain curves of the DFRCC mix after heating to different temperatures

The effect of temperature on ultimate tensile strength of DFRCC is shown in Fig. 4.12(a). It can be observed that temperature increase augmented ultimate tensile strength of DFRCC initially. At 100 ℃, the tensile strength increased by 2% compared to that at 30 ℃. At 200 ℃, the tensile strength reached a peak value of 5.9 MPa, 107% of that at 30 ℃. However, the tensile strength of DFRCC specimens exposed to 300 ℃ decreased to 4.99 MPa, 91% of that at 30 ℃. With increasing temperature from 300 ℃ to 600 ℃, the tensile strength decreased steadily. Fig. 4.12(b) shows the influence of temperature on tensile strain capacity of DFRCC. As can be seen from Fig. 4.12(b), the capacity decreased significantly after exposure to

100 ℃ and 200 ℃, and then reached the minimum value at 300 ℃. Beyond 300 ℃, a very slight increase in strain capacity was observed as temperature increased, although these strain capacities were at least one order of magnitude lower than those of specimens exposed to temperature below 200 ℃. That the strain capacities of DFRCC showed one-order-of-magnitude difference was caused by distinct tensile failure mechanisms. The specimens exposed to temperature below 200 ℃ exhibited multiple-fine-cracks failure mode. The strain capacity is closely related to the number of fine cracks occurring on the specimen. The fewer the number of fine cracks, the smaller is the strain capacity, and vice versa. The specimens exposed to 300 ℃ and higher temperature failed in a single-crack mode. It is noteworthy that although the specimens at 300 ℃ failed in a single-crack mode, they still retained some tensile capacity after the occurrence of the single crack (Fig. 4.11(c)). It should be noted that PVA fibers (43 μm thick) have a melting point at about 240 ℃. So after 200 ℃ exposure, residual PVA fibers (see Fig. 4.13(a)) could still contribute to bridging action across a cracked section. But at 300 ℃ and beyond, PVA fibers had melted and steel fibers (183 μm thick) were the only source of bridging stress across the crack (see Fig. 4.13(b)). Based on physical observation of ruptured cross sections of tensile specimens, steel fibers remained intact after failure. This was because bridging stress across a crack was controlled by the bond stress between steel fibers and DFRCC matrix, rather than tensile strength of steel fibers. At 400 ℃ and beyond, the specimens lost their load-carrying capacity completely once a crack occurred (Fig. 4.11(d)-(f)). Although steel fibers did not melt at these temperatures, the solid DFRCC matrix deteriorated due to decomposition of hydrated products, further weakening the bond strength between the steel fibers and the matrix to such an extent that it became negligible. This explained the quasi-brittle fracture of DFRCC specimens subject to tension at 400 ℃ and beyond. In contrast, DFRCC with 2% vol. PVA fibers only exhibited brittle fracture under tension at 300 ℃ (Bhat et al. 2014). Clearly, steel fibers can

improve residual tensile performance of DFRCC by delaying the occurrence of brittle tensile behavior to a higher temperature.

To account for the tensile behaviors of DFRCC after elevated temperatures as shown in Fig. 4.11, the micromechanics model for tailoring strain-hardening behavior of composites (Kim et al. 2003) is extended to incorporate the effect of temperature. According to micromechanics design guidelines (Kim et al. 2003), two conditions are required to achieve pseudo strain-hardening. The first condition is related to the formation of steady-state cracking, which requires the crack tip toughness J_{tip} not to exceed the complementary energy $J_b^{'}$ determined by the bridging stress σ versus crack opening δ curve (Li et al. 2001). The relationship is defined in Eqn. (4.2):

$$J_{tip} = \frac{K_m^2}{E_c} \le \sigma_0 \delta_0 - \int_0^{\delta_0} \sigma(\delta)d\delta = J_b^{'} \tag{4.2}$$

where σ_0 is the maximum bridging stress corresponding to opening width δ_0, K_m is the matrix fracture toughness, and E_c is the composite elastic modulus.

The second condition is that tensile cracking strength of the matrix σ_c must be smaller than the maximum bridging stress σ_0 as shown in Eqn. (4.3):

$$\sigma_c < \sigma_0 \tag{4.3}$$

The complementary energy $J_b^{'}$ and the maximum bridging stress σ_0 are dependent on bridging stress σ versus crack opening δ curve of fibers. The curve can be obtained by averaging over the contributions of fibers that cross the matrix crack plane as a single crack opens up (Lin et al. 1999):

$$\sigma(\delta) = \frac{V_f}{A_f} \int_0^{\frac{\pi}{2}} \int_0^{\frac{l_f}{2}\cos\phi} P(z,\phi) \frac{\sin\phi}{l_f} dz d\phi \tag{4.4}$$

For the DFRCC mix with hybrid fibers exposed to elevated temperatures, Eqn. (4.4) can be rewritten as

$$\sigma(\delta) = \frac{V_P}{A_P} \int_0^{\frac{\pi}{2}} \int_0^{\frac{l_P}{2}\cos\phi} P_P(z,\phi,T) \frac{\sin\phi}{l_P} dz d\phi + \frac{V_S}{A_S} \int_0^{\frac{\pi}{2}} \int_0^{\frac{l_S}{2}\cos\phi} P_S(z,\phi,T) \frac{\sin\phi}{l_S} dz d\phi \quad (4.5)$$

where V_P, V_S are respectively the volume fractions of PVA and steel fibers; A_P, A_S are respectively the cross-sectional areas of PVA and steel fibers; l_P, l_S are the lengths of PVA and steel fibers, respectively; ϕ is the fiber inclination angle; z is the centroidal distance of a fiber from the crack plane; $P_P(z,\phi,T)$ and $P_S(z,\phi,T)$ are respectively the temperature-dependent bridging forces contributed by a single PVA and a single steel fiber.

At 100 ℃ and 200 ℃, a possible degradation in $P_P(z,\phi,T)$ reduced the maximum bridging stress. The reduced bridging stress resulted in reduced complementary energy J_b' and reduced peak bridging stress σ_0. In contrast, crack tip toughness J_{tip} and matrix tensile cracking strength σ_c increased after exposure to 100 ℃ and 200 ℃. Consequently, pseudo strain-hardening (*PSH*) performance indices (Kanda and Li 2006) decreased, which accounted for smaller strain capacities of SHCC at 100 ℃ and 200 ℃.

From 300 ℃ onwards, the first term in Eqn. (4.5) contributed by PVA fibers diminished due to melting of PVA fibers. It caused a significant loss in bridging force across the crack plane. The J_b' in Eqn. (4.2) and σ_0 in Eqn. (4.3) are dependent on bridging stress-strain relationships of fibers, so absence of the PVA fibers results in a significant reduction of J_b' and σ_0. The conditions to achieve strain-hardening required by Eqn. (4.2) and (4.3) can no longer be satisfied. Therefore, DFRCC specimens exhibited strain-softening behavior at 300 ℃. At 400 ℃ and above, the

bond strength between the steel fibers and the matrix further deteriorated, leading to brittle tensile failure of DFRCC specimens.

(a) Ultimate tensile strength   (b) Strain capacity
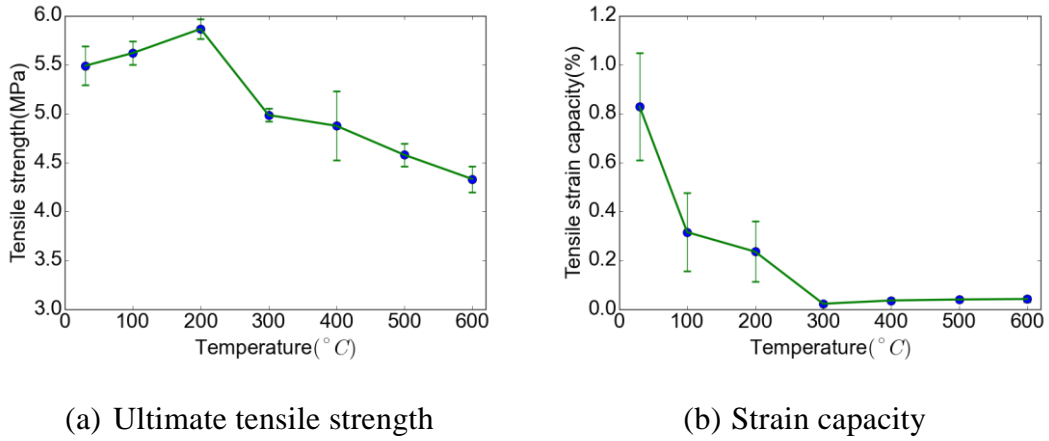
Fig. 4.12 Influence of temperature on (a) ultimate tensile strength and (b) strain capacity of DFRCC

(a) 200 ℃   (b) 300 ℃
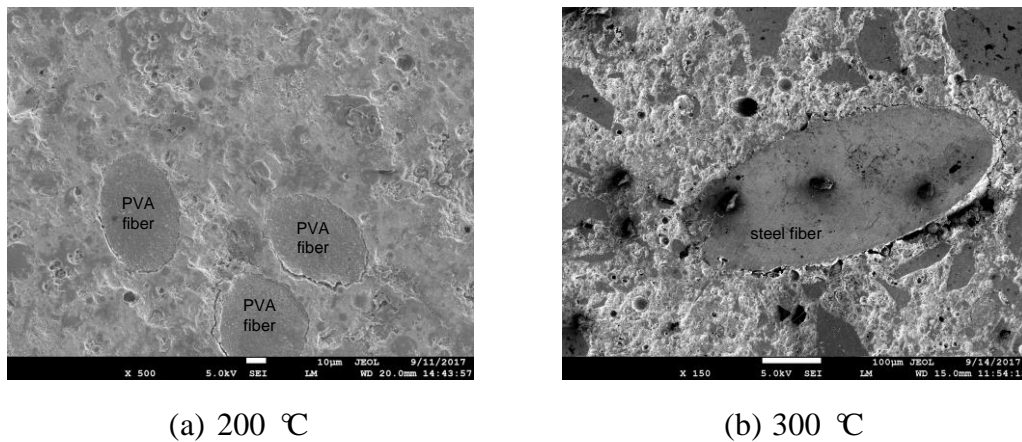
Fig. 4.13 SEM micrographs of status of PVA and steel fibers after 200 ℃ and 300 ℃

Fig. 4.14 plots the reduction factor for tensile strength of DFRCC at elevated temperatures, together with that of concrete prescribed in Eurocode 2 (Institution 2004). It can be observed that the strength reduction factor of DFRCC was smaller than that of concrete at these six temperatures. At 600 ℃, the strength reduction factor of concrete became zero, while that of DFRCC was 0.79, indicating that a

large portion of tensile strength remained even after exposure to 600 ℃. The reason for the improvement in tensile strength of DFRCC compared to normal concrete is similar to that for compressive strength.
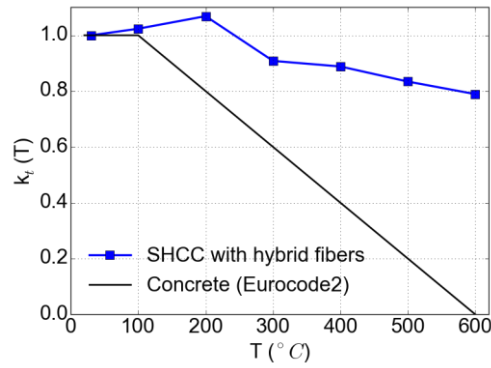
Fig. 4.14 Coefficient $k_t(T)$ allowing for decrease of tensile strength at elevated temperatures

Fig. 4.15(a)-(g) shows the maximum normal strain contours of DFRCC specimens exposed to 30, 100, 200, 300, 400, 500, and 600 ℃, respectively. In the strain contours, a crack was characterized by strain localization. It was found that the number of fine cracks reduced with an increase of temperature up to 200 ℃ (Fig. 4.15(a)–(c)), which was consistent with the trend of reducing strain capacity. Single crack was observed on the surface of DFRCC specimens from 300 ℃ onwards (Fig. 4.15(d)–(g)), corroborating with the trend in Fig. 4.11, which shows the disappearance of tensile strain hardening characteristic with increasing temperature.

(a) 30 ℃

(b) 100 ℃   (c) 200℃   (d) 300 ℃

(e) 400 ℃   (f) 500 ℃   (g) 600 ℃
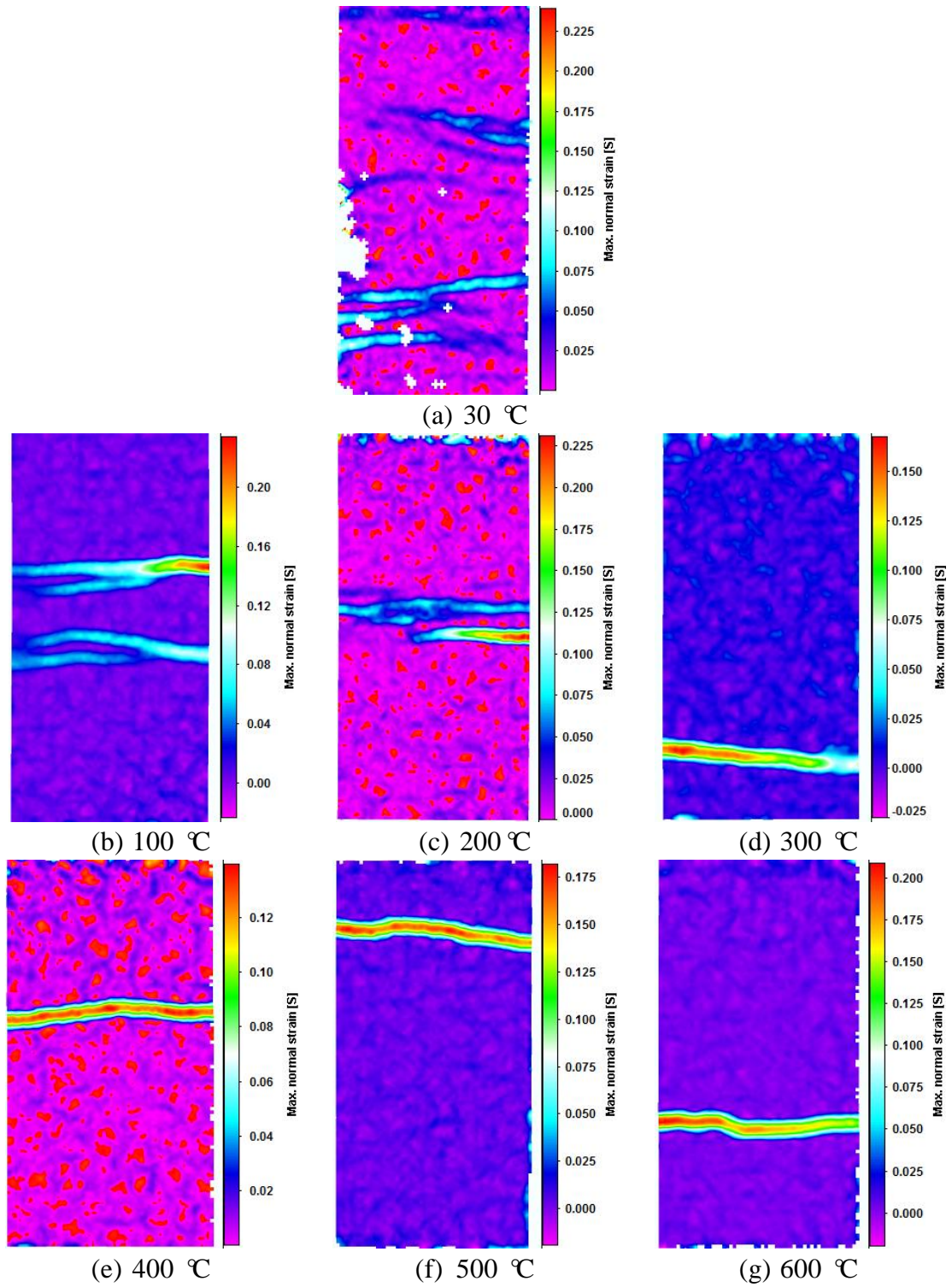
Fig. 4.15 Maximum normal strain fields of DFRCC specimens at failure after different temperatures

4.4 Summary

Based on the presented work on residual mechanical properties and spalling resistance, the following conclusions can be drawn:

- The residual compressive strength of DFRCC with hybrid fibers showed an increase after 200 ℃ heating. Beyond 200 ℃, the residual compressive strength reduced with temperature increase. Even so, the compressive strength of DFRCC with hybrid fibers after 800 ℃ heating can retain about 35% of its original strength. The residual elastic modulus of DFRCC decreased with temperature increase. The decreasing trend in residual elastic modulus was aggravated after exposure to 600 ℃ and above. After 800 ℃, 13.2% of elastic modulus of unheated DFRCC was retained. In general, the studied DFRCC outperformed concrete in terms of compressive strength and elastic modulus reduction against elevated temperature.

- At 300 ℃, DFRCC specimens with hybrid fibers showed strain softening tensile behavior instead of brittle nature exhibited by DFRCC specimens with PVA fibers only. It demonstrated the beneficial effect of addition of steel fibers in resisting tensile brittle failure after high temperature exposure. The DFRCC specimens with hybrid fibers exhibited tensile brittle failure beyond 400 ℃. More steel fibers are recommended to transfer the brittle behavior beyond 400 ℃ to ductile behavior.

- DIC analysis results showed that the number of fine cracks of DFRCC specimens under tension reduced with temperature rise up to 200 ℃. Beyond 300 ℃, only one crack occurred at the failure of DFRCC specimens. These DIC figures corroborated well with diminishing tensile strain capacity shown by tensile stress-strain curves.

CHAPTER 5. UNIFIED THEORY OF FIRE SPALLING

IN CONCRETE

5.1 Introduction

Fire-induced deterioration in mechanical performance and fire-induced spalling are two major issues faced by concrete materials. DFRCC, as a special type of bendable concrete, also has to face these two issues. The previous two chapters focus on fire-induced deterioration in mechanical performance of DFRCC and present an experimental program to improve and examine mechanical performance of fire-damaged DFRCC. Then it brings up the question of whether the optimized DFRCC suffers from fire-induced spalling. But before examining thermal spalling resistance of DFRCC, the first priority is to work out fire-induced concrete spalling mechanism.

Fire-induced spalling is a phenomenon which occurs in concrete structures under fire. It is characterized by violent or non-violent dislodgement of pieces or chunks of concrete from heated concrete surface. Consequently, spalling results in loss of concrete section, reduction in loading-bearing capacity and fire resistance of concrete members (Lee et al. 2012, Wu et al. 2013).

Understanding the physics behind this phenomenon is significant for prediction of spalling and advancement in protective measures against spalling. So far mainly three theories have been proposed to explain fire spalling of concrete materials. The first theory assumes that concrete spalling is caused by pore pressure buildup, known as pore pressure spalling (Kanéma et al. 2011). The second assumes that concrete spalling is caused by thermal stress, known as thermal stress spalling (Zhao et al. 2014). There is also a third school that combines the effects of thermal

stress and pore pressure to account for concrete spalling (Connolly 1995). However, no consensus has been reached on spalling mechanism to date.

This chapter compiles conflicting and common views from previous research works on fire-induced concrete spalling. Based on the analyses of these contradictory and concordant test results, a unified and consistent spalling theory is proposed. According to the driving mechanisms, fire-induced spalling can be categorized into three types: thermo-hygral spalling, thermo-mechanical spalling, and thermo-chemical spalling. The mechanisms of these three types of spalling are explained and the criteria to forecast each of them are established in this chapter. They are found to occur within different temperature ranges. The factors that influence them, solutions to prevent them and interactions between them are also discussed.

5.2   Conflicting views regarding previous work on fire-induced concrete spalling

5.2.1 Spalling mechanism

Fire spalling of concrete is commonly explained by two distinct mechanisms:

- Pore pressure buildup: the heating of concrete involves moisture migration inside the porous medium. Moisture in concrete is moving inwards and outwards driven by pressure gradient. For moisture that migrates into the deep, unheated region, water vapor condenses and a "moisture clog" is gradually formed due to accumulation of liquid water. This formation of "moisture clog" inhibits inward moisture flow, leading to an increase in pore pressure at the front of the "moisture clog". Locally, induced pore pressure can exceed tensile strength of concrete and thus lead to spalling (Tenchev et al. 2001, Benmarce and Guenfoud 2005).

● Thermal stress: the heating of a concrete element involves high temperature gradient, particularly in the first few centimeters from the heated surface. There are two kinds of views concerning how thermal gradient induces spalling. Some researchers believe that spalling is initiated by thermal gradient-induced radial tensile stress (Zhao et al. 2014), while others hold that compressive stresses resulting from restrained thermal expansion can locally exceed compressive strength of concrete and cause spalling (Msaad and Bonnet 2006).

So far, there is no consensus on which of the two processes is dominant.

5.2.2 Influence of factors

● Degree of restraint (DOR)

Many experimental results have shown that unrestrained and unloaded concrete specimens experienced explosive spalling under high temperature. DOR is defined as a ratio between the actual axial force generated in the element induced by thermal expansion to the hypothetical stress at total restraint. The DOR in these tests was zero. If spalling was indeed induced by restrained thermal dilation, there should not be any spalling in these unrestrained concrete specimens. This inference is obviously contradicted by experimental results (Noumowe et al. 1996, Klingsch 2014). Therefore, it can be concluded that compressive stresses generated from restrained thermal dilation is not a necessary condition for occurrence of spalling at high temperature.

● Thermal gradient

According to thermal gradient-induced thermal stress spalling theory, a high thermal gradient across a section leads to a high spalling risk, and vice versa

(Jansson and Boström 2010). Hence, concrete subjected to a higher heating rate should be more prone to spalling than concrete under a lower heating rate.

However, Noumowe et al. (2006) found severe spalling in concrete at a heating rate as low as 0.5 ℃/min. Klingsch (2014) studied the influence of heating rate on the occurrence of thermal spalling. Low heating rates were used to minimize thermal gradient-induced thermal stress. Nonetheless, some concrete specimens still spalled even at 0.5 ℃/min. These experimental facts did not support gradient-induced thermal stress spalling mechanism.

Furthermore, it was reported that concrete with certain amounts of PP fibers subject to extreme high heating rate was free from thermal spalling (Han et al. 2005, Phan 2008). In contrast, explosive spalling occurred in concrete without PP fibers even at a slow heating rate of 0.5 ℃/min. Kaného et al. (2011) found that spalling extent of HSC was greater than NSC, although in their tests thermal gradient in HSC specimens was lower than that in NSC specimens. These experimental results could not be explained by thermal gradient-induced thermal stress spalling mechanism.

On the other hand, spalling in concrete was observed to occur in different manners. At low heating rates (0.5-1 ℃/min, or insulated with thermal barrier), concrete specimens could explode violently characterized by a loud bang (Phan et al. 2001), whereas at high heating rates (such as in a hydrocarbon fire), concrete specimens could scale off progressively accompanied by popping sounds (Hertz 2003, Jansson 2013). It would be far-fetched to rely on thermal gradient-induced thermal stress spalling theory to explain these two different spalling patterns exhibited by concrete under different heating rates.

These aforementioned experimental results were in conflict with the theory that concrete spalling was governed by gradient-induced thermal stress. Therefore, gradient-induced thermal stress may not be the only critical factor contributing to concrete spalling.

● Steel fibers

Different conclusions were made about the effectiveness of steel fibers in mitigating spalling of concrete under fire (Tan et al. 2015). Klingsch (2014) conducted spalling tests on unrestrained and unloaded concrete cylinders with steel fibers and found that steel fibers had no beneficial effect in minimizing explosive spalling. However, Kodur et al. (2003) conducted fire endurance tests on HSC columns and found that steel fibers reduced spalling in concrete columns and enhanced fire resistance of HSC columns. The quantities of steel fibers used in the concrete mixes of Klingsch (2014) and Kodur et al. (2003) were 195 kg/m^3 and 42 kg/m^3, respectively.

● Time of spalling

Mindeguia et al. (2009) observed that thermal spalling occurred in unrestrained and unloaded concrete slabs between 10 and 20 minute of ISO fire test. Coincidently, Ko et al. (2011) observed that spalling occurred in unrestrained and unloaded concrete slabs within 10 min of ISO 834 (similar to ASTM E119) fire heating.

However, Franssen and Dotreppe (2003) observed surface spalling in concrete columns between 20 and 60 minutes of fire test. Kodur and Mcgrath (2003) observed significant spalling at the corners of concrete columns after about 1 hour of ASTM E119 fire heating towards the end of fire endurance test. Besides, Han et al. (2014) found that spalling in steel reinforced concrete columns occurred at the intermediate and later stage of ISO 834 fire that lasted about 2.5 hour.

According to the pore pressure spalling mechanism, spalling tends to occur when the tensile stress induced by the vapor pressure surpasses the hot tensile strength of concrete. At 374 ℃, the saturated vapor pressure reaches about 22 MPa. It only takes a few minutes for the exposed concrete cover to reach this critical temperature under fire, so it is reasonable that concrete spalling was observed to occur at the

early stage of a fire. However, occurrences of concrete spalling at intermediate or even much later stage of a fire cannot be explained by pore pressure spalling mechanism.

It is noted that, in cases that late spalling (Kodur and Mcgrath 2003, Han et al. 2014) was observed, the tested elements were restrained. This indicates that restraint stress, instead of pore pressure, is possibly the cause for the observed late spalling.

● Section size

Explosive spalling of large concrete cylinders was observed under a heating rate of 1 °C/min. However, reduction of cylinder size by either 75% or 50% eliminated the risk of explosive spalling (Hertz 1984). Kanéma et al. (2011) examined the size effect on thermal spalling risk of concrete. He observed that for the same concrete mixture and heating rate, spalling occurred only in large specimens ($\Phi160$ mm $\times$ 320 mm), although thermal gradient in small specimens ($\Phi110$ mm $\times 220$ mm) was similar to that of large specimens. These experimental evidences were in conflict with thermal gradient-induced spalling theory. Restrained thermal dilation-induced thermal stress also could not explain this phenomenon, since these tested concrete specimens were unrestrained. However, this could be reasonably explained by the pore pressure spalling theory. Smaller dimensions of specimens facilitate quicker escape of moisture out of the concrete, consequently resulting in a lower pore pressure compared to that of larger specimens. Therefore, the spalling risk is reduced as the specimen size decreases.

● Post-cooling spalling

Spalling has been observed in concrete not during the heating phase but after cooling down Klingsch (2014). This type of spalling is referred to as post-cooling spalling (Khoury 2008). It is possibly caused by 44% volume expansion resulting from rehydration of calcium oxide after cooling (Annerel and Taerwe 2009). This

rehydration process takes place when moisture is available for heated concrete. Post-cooling spalling cannot be explained by either thermal stress or pore pressure buildup.

● Others

Arioz (2009) observed partial spalling in unloaded and unrestrained concrete specimens exposed to 1200 ℃ for 2 hours. However, no spalling was observed in concrete specimens exposed to 200, 400, 600, 800, and 1000 ℃ for 2 hours. Both pore pressure spalling theory and thermal spalling theory on their own could not explain this phenomenon. This type of spalling is more likely a result of complete destruction of aggregate-cement bond due to significant decomposition of the cement matrix.

5.3 Common views regarding previous work on fire-induced concrete spalling

5.3.1 Influence of permeability

It is widely accepted that permeability has a significant effect on fire-induced concrete spalling. Concrete with a lower permeability is more prone to spalling under heating, while concrete with a higher permeability has a decreased propensity for thermal spalling.

● PP fibers

Addition of PP fibers has been found to decrease spalling risk of concrete under fire (Khoury and Willoughby 2008, Jansson and Boström 2013). Different hypotheses (Table 5.1) are proposed to explain the mechanism of PP fibers in mitigating spalling. Although no consensus has been reached on the mode of action of PP fibers in preventing spalling, all these hypotheses lead to a common consequence,

which is a significant increase in permeability of concrete. The significant increase in permeability of PP fiber-reinforced concrete has been confirmed by a number of tests (Zeiml et al. 2006, Bošnjak et al. 2013).

Table 5.1 Different modes of action of PP fibers in combating spalling

Hypotheses	Description
Vacated micro-channels theory (Kalifa et al. 2001)	Micro-channels left by melted fibers facilitate the escape of steam.
Interfacial Transition Zones (ITZ) theory (Zeiml et al. 2006)	The ITZ between hydrophobic fibers and cement matrix facilitate the escape of steam.
Pressure-induced tangential space (PITS) theory (Khoury 2008)	The PITS between hydrophobic fibers and cement matrix facilitates the escape of steam.
Micro-cracks theory (Pistol et al. 2011)	The micro-cracks induced by melting of fibers facilitate the escape of steam.

● Silica fume

Published test data shows that concrete with silica fume has a higher risk of thermal spalling than concrete without silica fume (Hertz 1984). Studies show that concrete with silica fume contains dense pore structure and has low permeability (Ramezanianpour and Malhotra 1995), which explains the higher propensity for spalling.

5.3.2 Influence of moisture

It is widely recognized that moisture content of concrete is one critical factor influencing thermally-induced explosive spalling. The higher the moisture content, the greater is the spalling risk, especially when the moisture content exceeds a threshold limit (Ko et al. 2011).

5.4   Unified and consistent fire-induced concrete spalling theory

Analysis of experimental results in Section 5.2 rules out the possibility that thermal gradient-induced thermal stress is a critical factor contributing to concrete spalling. Spalling phenomena of many unloaded and unrestrained concrete specimens, together with the effect of permeability and moisture content, confirm that pore pressure build-up is mainly responsible for these observed spalling.

However, spalling of concrete cover in columns, occurring at intermediate or later stage of fire tests, can hardly be explained by the pore pressure spalling theory. On the other hand, similar cover spalling has been observed in concrete columns loaded in concentric compression at room temperature before the columns attained the ultimate capacity (Foster et al. 1998, Foster 2001). Hence, in these cases, initial applied compressive stress and thermal stress generated from restrained thermal dilation other than pore pressure contribute to this type of spalling.

Sloughing-off spalling at extremely high temperature and post-cooling spalling are due to complete chemical decomposition of major concrete constituents, and much less related to pore pressure build-up and thermal stress.

Therefore, there are three types of fire-induced spalling based on three distinct mechanisms, viz., thermo-hygral, thermo-mechanical, and thermo-chemical spalling. All these three types of spalling are possible to occur in concrete elements under fire but most often at different temperature ranges.

5.4.1 Thermo-hygral spalling

● Mechanism

Thermo-hygral spalling, also known as pore pressure spalling, is related to thermal-hygral behavior in concrete. Concrete is a composite building material with porous microstructure. Fig. 5.1 shows a schematic representation of volumetric proportion of concrete components before and during hydration. Hardened concrete contains aggregate, unhydrated cement, hydrated products, free water, gel water, and pores. The hydrated products contain chemically-bound water. This is similar for concrete containing pozzolans (silica fume, fly ash, GGBS etc.) which involves a pozzolanic reaction between portlandite and silicic acid.
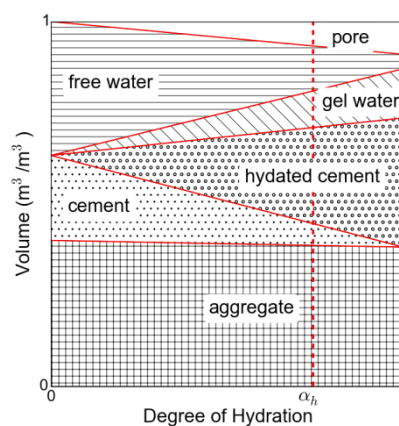
Fig. 5.1 Schematic representation of volumetric proportions of concrete components before and after hydration
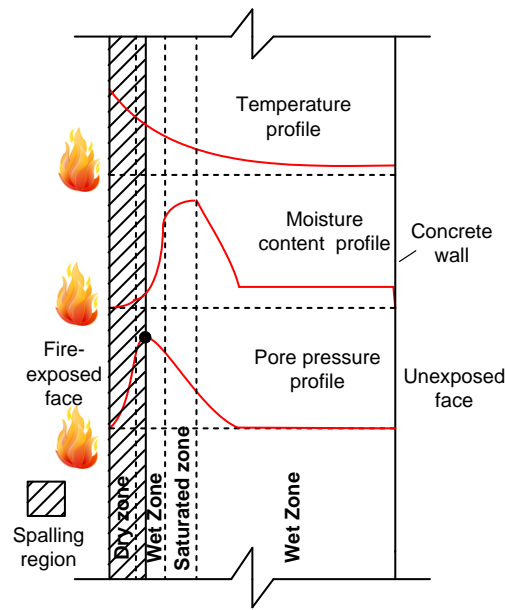
Fig. 5.2 Schematic representation of thermo-hygral spalling of a concrete wall exposed to fire on one face

A schematic description of thermo-hygral spalling in a concrete wall heated from one face is presented in Fig. 5.2. When concrete is under fire, a temperature gradient is formed in the area near fire-exposed face. Gel water and chemically-bound water will be released into micropores of concrete and added to free water as temperature rises. Pore pressure gradually develops as a consequence of temperature rise and presence of moisture (mixed liquid and vapor). A pressure gradient is formed due to the temperature gradient and degree of pore saturation. Moisture is driven by the pressure gradient to two opposite directions, one direction towards the heated dried face while the other towards the deeper, cooler region. As a consequence, three zones will be generated, i.e., dry zone, wet zone and saturated zone (the so-called "moisture clog"). When the peak pressure exceeds hot tensile strength of concrete, bursting failure of concrete occurs (Fig. 5.3). The peak pressure is developed at the saturation front, i.e. the wet zone in front of the saturated zone (Bangi and Horiguchi 2012, Ozawa et al. 2012). In the wet zone, water exists as a mixture of water vapor and liquid water, and the pore pressure is equal to the sum of saturated vapor pressure and air pressure. Considering that the

air pressure is negligible compared to saturated vapor pressure, this peak pressure can be approximately taken as saturated vapor pressure, which is consistent with the experimental findings (Kalifa et al. 2000, Mindeguia et al. 2010).
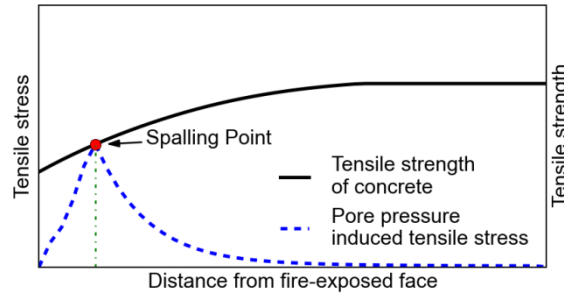
Fig. 5.3 Pore pressure-induced tensile stress profile at the time of spalling

● Spalling temperature

Thermo-hygral spalling of concrete is induced by tensile stress $\sigma_{p,t}$ caused by peak pore pressure. When the tensile stress exceeds temperature-dependent tensile strength of concrete (Eqn. (5.1)), spalling occurs.

$$\beta_t p_p \geq f_t(T) \tag{5.1}$$

The peak pore pressure p_p at the time of spalling is equal to saturation vapor pressure. The scaling factor β_t is used to calculate tensile stress induced by the pore pressure. If the hollow spherical model is adopted to approximate concrete microstructure, the scaling factor is calculated using Eqn. (5.2), in which ϕ is porosity (Ichikawa and England 2004).

$$\beta_t = \frac{(1+2\phi)}{2(1-\phi)} \tag{5.2}$$

However, the micro-pores in concrete are not spherical, and using Eqn. (5.2) to calculate β_t tends to underestimate $\sigma_{p,t}$. According to Tenchev and Purnell (2005) and Klingsch (2014), β_t is more reasonably taken as unity. If tensile strength

reduction factor $k_t(T)$ and concrete tensile strength are known, the concrete temperature at the spalled location (spalling temperature) can be determined.

The compressive strength of concrete in research works lies in the range of 30-200 MPa. Assuming that the tensile strength of concrete is 1/10 of its corresponding compressive strength, the lower and upper bound values of tensile strength are 3 MPa and 20 MPa, respectively. The temperature-dependent tensile strength reduction factor specified in Eurocode 2 (Institution 2004) is adopted. According to the criterion for thermo-hygral spalling, spalling temperature would lie within the range between $T_{THS,l}$ (220 ℃) and $T_{THS,u}$ (320 ℃) as shown in Fig. 5.4, if thermo-hygral spalling were to occur.
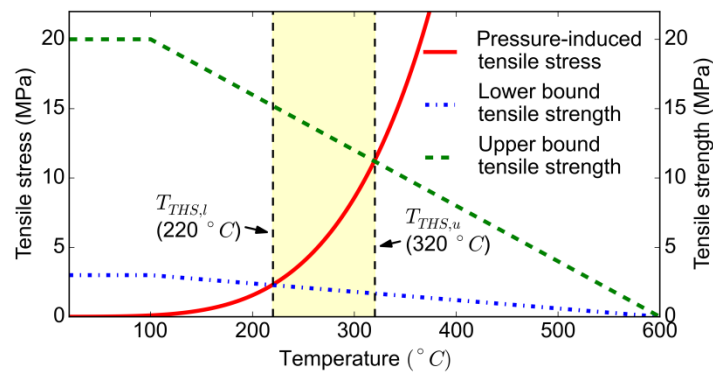
Fig. 5.4 Thermo-hygral spalling temperature range

Table 5.2 shows the temperature information at spalling of unrestrained and unloaded specimens provided by different researchers. Although it is difficult to measure the temperature at the spalled location, the spalling temperature should fall between the surface temperature and the interior core temperature. It can be seen that the theoretical thermo-hygral spalling temperature range generally matches those observed from experiments.

In a fire, the temperature of cover concrete would quickly reach the thermo-hygral spalling temperature. If thermo-hygral spalling occurs, it will occur at the early

stage of the fire. Consequently, it tends to reduce fire resistance of concrete members significantly.

Table 5.2   Temperature information at spalling of unrestrained and unloaded specimens

Source	Gas temperature	Surface temperature	Core temperature	Spalling temperature*
Hertz (1984)	300, 400 ℃	-	-	<400 ℃
Noumowe et al. (1996)	-	-	-	250 - 300 ℃
Phan et al. (2001)	300, 450 ℃	-	240 - 280 ℃	240 - 450 ℃
Kalifa et al. (2001)				190 - 250 ℃
Fares et al. (2009)	315 ℃	-	-	<315 ℃
Kanéma et al. (2011)	-	355 ℃	-	<355 ℃
Debicki et al. (2012)	-	245, 291, 319 ℃	150, 223, 262 ℃	150 - 319 ℃
Klingsch (2014)	-	297 - 433 ℃	256 - 304 ℃	256 - 433 ℃
Akturk et al. (2015)	425, 455 ℃	-	-	<455 ℃

* Spalling temperature means the temperature of concrete at the spalled location at the time of spalling.

● Spalling pattern

The occurrence of thermal-hygral spalling is accompanied with a release of energy. Hence, the spalled-off concrete pieces break away from concrete elements at a certain initial velocity. In the experiments conducted by Zeiml et al. (2008), the maximum observed initial velocity of spalled-off pieces reached up to 14 m/s. Hence, the term "explosive spalling" mentioned in previously published works refers to thermal-hygral spalling in the current framework. When concrete is under slow heating, spalling tends to be a sudden bursting failure accompanied by a loud

bang. When concrete is under fast heating, spalling is dominated by progressive peeling-off with continuous popping sounds. Both the one-time explosive spalling with slow heating and progressive spalling associated with fast heating occur in a violent manner.

● Influencing factors

Permeability: Moisture migration is dependent on permeability of concrete. Low permeability means the trapped moisture in concrete evacuates slowly and facilitates pore pressure development. Therefore, concrete with a lower permeability has a higher susceptibility to thermo-hygral spalling, and vice versa. Density and compressive strength of concrete in most cases serve as indicators of permeability. High density and high compressive strength usually indicate a low permeability, but this is not always the case.

Degree of pore saturation (DPS): Moisture content of concrete has been widely used as a parameter for assessing the thermo-hygral spalling risk. Eurocode 2 recommends that explosive spalling is less likely to occur if the moisture content of concrete is less than 3% by weight. However, moisture-rich concrete may be free from thermo-hygral spalling if the porosity of concrete is high; moreover, concrete with moisture content less than 3% may still suffer from thermo-hygral spalling if the porosity is low. Therefore, it is more scientific to use the DPS to assess risk of explosive spalling. A larger DPS tends to increase the thermo-hygral spalling risk. The DPS also influences permeability of concrete. Increased DPS decreases the permeability and vice versa. In practice, the DPS of indoor concrete elements decreases as concrete ages, and consequently, explosive spalling risk decreases. However, this is not the case for other situations where concrete elements are exposed to natural environment, such as tunnels and offshore structures.

Heating rate: A high heating rate tends to result in an early spalling of concrete characterized by progressive scaling-off. The extent of thermo-hygral spalling of concrete specimens when subjected to a high heating rate is normally higher than when subjected to a low heating rate. But it is not the case for ultra high performance concrete (UHPC) with extremely low permeability. For UHPC specimens under a low heating rate, one-off explosive spalling may occur which completely disintegrates the specimens. Under a low heating rate, it takes a long time for one specimen to reach the critical spalling temperature. By the time when the critical spalling temperature is reached in the shallow region, moisture has been driven into the core region. The core region thus has adequate moisture to build up large pressure. When the critical temperature is reached, spalling initiates at the core region of the specimen.

Section dimension: The risk of thermo-hygral spalling increases with the specimen dimension. This is due to the fact that it takes a longer time for the trapped moisture to evacuate for a thicker specimen. The dimensions of concrete elements used in practice are large. Hence, it is more realistic to use full-scale specimens to evaluate thermo-hygral spalling risk of concrete than lab scale samples.

Aggregate: Using flint as the aggregate of concrete induces aggregate spalling. This aggregate spalling results from thermal instability of flint, which is due to high vapor pressure that builds up inside the laminar microstructure of flint (Xing et al. 2011). So this type of spalling is categorized as thermo-hygral spalling.

● Protective measures

The protective measures to mitigate thermo-hygral spalling with their disadvantages are presented in Table 5.3. Based on the influencing factors, adequate measures can be taken to minimize thermo-hygral spalling. There is little flexibility to change DPF and section dimensions. But concrete permeability,

heating rate, and aggregate type are within the control of engineers. It should be noted that although increasing concrete permeability reduces explosive spalling risk, it is adverse to durability of concrete. Therefore, a balanced approach is needed between spalling resistance and durability when undertaking concrete mix design.

Table 5.3 Solutions for preventing different types of thermal spalling*

Type of thermal spalling	Methods	Protective measures	Deficiency
Thermo-hygral spalling	Increase permeability	Add PP fibers, PVA fibers, jute fibers, raw rice husk, air-entraining agent etc.	Compromise in durability; disposable and poor resilience.
		Use no or less silica fume.	Compromise in durability; limited application.
	Reduce heating rate	Adopt thermal barrier.	Costly; may lead to spalling in deep sections.
	Selection of aggregate	No flints or other similar aggregates.	
Thermo-mechanical spalling	Selection of aggregate	Use calcareous aggregate instead of siliceous aggregate.	Restrictive.
	Decrease initial stress	Decrease load level.	Costly.
	Lower the temperature	Adopt thermal barrier.	Costly.
	Overcome brittleness	Add steel fibers.	Costly.
Thermo-chemical spalling	Selection of aggregate	Avoid use of calcareous aggregate.	Restrictive.
	Limit the amount of cement	Avoid excessive cement amount.	
	Lower the temperature	Adopt thermal barrier.	Costly.

* Only passive protective measures are given; active protective measures such as fire suppression system are not covered in this thesis.

5.4.2 Thermo-mechanical spalling

● Mechanism

A schematic description of thermo-mechanical spalling in concrete is presented in Fig. 5.5. When a concrete member is under fire, thermal stress develops inside the concrete due to temperature gradients across the member section and restrained thermal expansion. Therefore, the exterior surface layer of concrete is in a triaxial tension-compression-compression stress state. At first, restrained thermal dilation-induced compressive stress on exterior surface layer is the largest and increases with temperature. When the exterior surface concrete layer reaches its ultimate capacity, the peak of compressive stress profile moves inwards and acts on adjacent interior layer. This process repeats itself until the peak of compressive stress profile moves inwards to the interface between the concrete cover and the core. As shown in Fig. 5.5, a point at the interface is subjected to axial compressive stress $\sigma_{c,a}$, circumferential compressive stress $\sigma_{c,c}$ and tensile stress normal to the interface between the concrete cover and the core $\sigma_{t,ni}$. The tensile stress arises partly from thermal gradient-induced tensile stress, and partly from tensile stress set up at the cover-core interface due to confined effect provided by hoops. When the tensile stress reaches a critical value, approximately vertical cracks will form between concrete cover and concrete core. Interface cracking in itself is not sufficient for concrete cover to break away from the core. Inspection of concrete columns after fire tests conducted by Bailey (2002) showed that vertical cracks, about 50 mm into the column, had formed. This outer layer of concrete, although not spalled off yet, could be easily removed by hand. Therefore, for thermo-mechanical spalling to occur, a driving force is required. The driving force

may be the axial compressive stress exerting on cracked concrete cover, volumetric expansion of concrete core, or bending in longitudinal reinforcement.
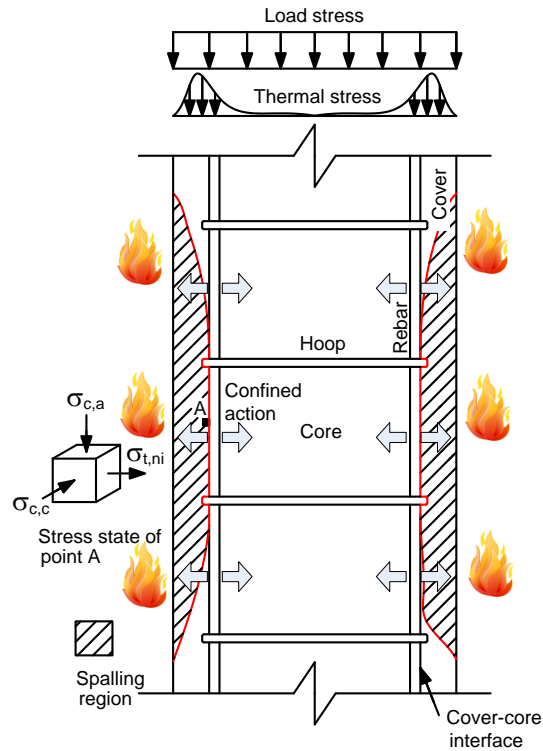
Fig. 5.5 Schematic representation of thermo-mechanical spalling of a concrete member

● Spalling temperature

Two conditions are needed for the occurrence of thermo-mechanical spalling in a concrete member. The first condition is the formation of longitudinal cracks, and the second is the driving force to separate the concrete cover from the interior core. It is difficult to judge when thermo-mechanical spalling occurs in the finite element model, and in fact currently no numerical model is available to predict the occurrence of this type of spalling. A simplified method is proposed here to predict roughly the spalling temperature.

The compressive stress in concrete at service condition is typically in the range of $0.1f_c$-$0.3f_c$. The maximum recorded compressive stresses in concrete with an initial

stress of $0.1f_c$ and $0.3f_c$ under fully restrained condition are $0.63f_c$ and $0.75f_c$, respectively, upon heating to 800 ℃ (RILEM 2007). Knowing that the compressive stress in heated concrete with no restraint is in the range of $0.1f_c$-$0.3f_c$, it is reasonable to assume that the peak compressive stress in heated concrete under realistic restraint condition is in the range of $0.5f_c$ and $0.7f_c$. The compressive strength reduction factor $k_c(T)$ specified in Eurocode 2 is adopted to account for the deterioration in compressive strength of concrete. It is believed that spalling tends to occur when the concrete cover reaches its compressive strength and enters post-peak stage. Then the concrete temperature at the cover-core interface would be roughly in the range between $T_{TMS,l}$ (430 ℃) and $T_{TMS,u}$ (660 ℃) as shown in Fig. 5.6, if thermo-mechanical spalling were to occur.
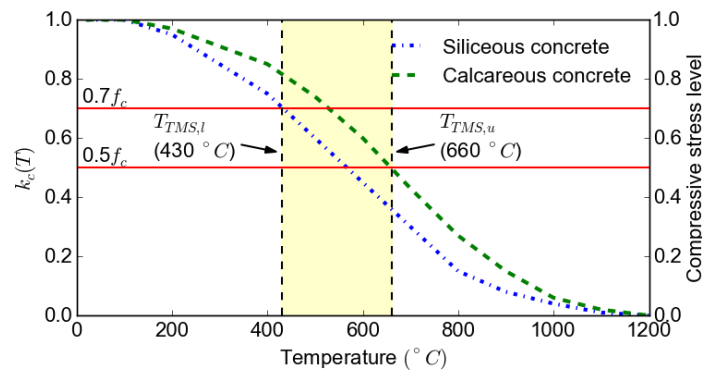
Fig. 5.6 Thermo-mechanical spalling temperature range

Thermo-mechanical spalling, if occurs in a fire, will occur at the intermediate or later stage of the fire. So it also reduces fire resistance of concrete members. But the negative influence of thermo-mechanical spalling on fire resistance of concrete members is smaller that of thermo-hygral spalling.

● Spalling pattern

Thermo-mechanical spalling of concrete occurs in the form of cover spalling or corner spalling. It is not explosive although popping sounds from the formation of longitudinal cracks can be alarming.

● Influencing factors

Aggregate: Concrete with siliceous aggregate is more susceptible to thermo-mechanical spalling than concrete with calcareous aggregate, since thermal expansion of siliceous concrete is larger than calcareous concrete and strength degradation of siliceous concrete is more severe than calcareous concrete (EN 2004).

Load level: Increasing load level tends to increase the severity of thermo-mechanical spalling, and vice versa.

DOR: Increasing DOR tends to increase the severity of thermo-mechanical spalling, and vice versa.

Exposure temperature level: Limit the temperature below potential threshold temperature for thermo-mechanical spalling can reduce spalling risk to a minimum.

Brittleness: Good ductility of concrete materials at high temperature reduces thermo-mechanical spalling risk, since fiber bridging action can maintain integrity after the formation of longitudinal cracks in concrete elements. Also the existence of fibers can delay the formation of longitudinal cracks. Keeping the concrete cover attached to the concrete core after crack formation is beneficial for fire resistance of structural members. Although the surface concrete layer contributes little to bearing capacity, it protects longitudinal reinforcement from directly exposing to fire and increases fire resistance of the member.

● Protective measures

The protective measures to mitigate thermo-mechanical spalling and their disadvantages are presented in Table 5.3. Based on the factors influencing thermo-mechanical spalling, using calcareous aggregate instead of siliceous

aggregate, decreasing load level, adopting fire-proof coating and adding steel fibers can combat thermo-mechanical spalling.

5.4.3 Thermo-chemical spalling

● Mechanism

There are two types of thermo-chemical spalling, viz. sloughing-off spalling at extremely high temperature, and post-cooling spalling after exposure to very high temperature. Both types of spalling are related to breakdown of calcium hydroxide, calcium-silicate-hydrates, calcareous aggregate etc. Internal cracking due to different thermal expansion of aggregate and cement-based paste could be one important condition to initiate thermo-chemical spalling. In addition, for sloughing-off spalling, significant destruction in aggregate-cement bond is also an important factor. Rehydration of calcium oxide (44% increase in volume) is believed to be the main cause of post-cooling spalling of concrete (Annerel and Taerwe 2009). So far, the knowledge of detailed post-cooling spalling mechanism is rather limited. But it reduces service life of concrete buildings, and could even lead to collapse of concrete buildings. Therefore, it is necessary to delve deeper into post-cooling spalling mechanism of concrete.

● Spalling temperature

Decomposition of calcium carbonate typically occurs between 700 °C and 900 °C (Chen et al. 2009). In the experiment conducted by Xing et al. (2011), post-cooling spalling occurred in concrete cylinders after heating to 750 °C. Thus, it is assumed that the threshold temperature $T_{TCS,t}$ for thermo-chemical spalling is about 750 °C (Fig. 5.7). When the temperature of concrete exceeds $T_{TCS,t}$, thermo-chemical spalling is likely to occur, especially for calcareous concrete.

Thermo-chemical spalling tends to occur at the later stage of a fire or after a fire. The negative influence of themo-chemical spalling on fire resistance of concrete members is very limited. However, the negative influence of themo-chemical spalling on residual load-bearing capacity of concrete members after a fire can be signifcant and therefore cannot be neglected.
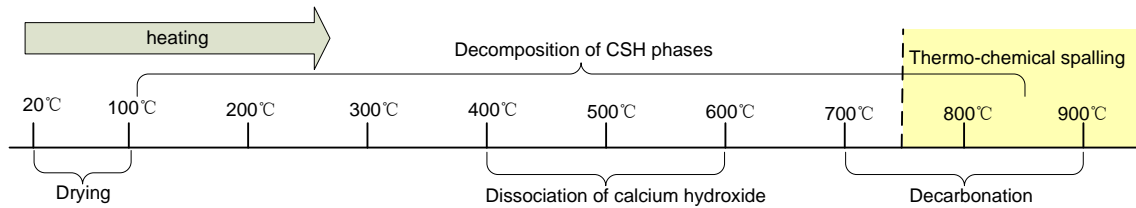
Fig. 5.7 Thermo-chemical spalling temperature range

● Spalling pattern

Thermo-chemical spalling of concrete occurs in the form of gentle sloughing-off. Although post-cooling spalling is not explosive, if neglected, it could possibly lead to unexpected failure of concrete structures. Therefore, assessment of fire-damaged concrete must include evaluation of post-cooling spalling risk.

● Influencing factors

Calcareous aggregate: Decomposition of calcareous aggregate generates calcium oxide. Rehydration of calcium oxide with subsequent volumetric expansion is believed to be the main cause for post-cooling spalling.

Cement content: Dehydration of calcium hydroxide generates calcium oxide, so it is not recommended to use excessive cement in a unit volume of concrete.

Exposure temperature level: Limiting the temperature to below 750 ℃ can reduce thermo-chemical spalling risk to a minimum.

● Protective measures

Table 5.3 presents the protective measures to mitigate thermo-chemical spalling and their disadvantages. Based on the influencing factors, avoiding using calcareous aggregate, limiting cement content and using fire-proof coating can mitigate thermo-chemical spalling.

5.5 Discussion

Behavior of structural concrete under fire is a coupled thermo-hygro-chemo-mechanical problem. There is interaction between thermo-hygral, thermo-mechanical, and thermo-chemical spalling. Under the effect of applied stress, there is a small decrease in permeability up to a certain threshold level. When the threshold stress is exceeded, there will be a significant increase in concrete permeability (Hoseini et al. 2009). Therefore, mechanical damage induced by external load is beneficial to mitigate thermo-hygral spalling. Thermo-hygral spalling reduces cross-section area and increases eccentricity of loading, which tends to induce thermo-mechanical spalling. Damage induced by internal pore pressure and external load increases thermo-chemical spalling risk. Previous research work focuses more on spalling of unstressed concrete members, and much less is done on spalling of stressed or restrained concrete. Thermo-hygral spalling and thermo-mechanical spalling are commonly mistaken as the same type of spalling. Future research should be conducted on spalling in stressed or restrained concrete members, since results from unstressed spalling tests can be misleading and impractical.

Current codes of practice only prescribe some measures against thermo-hygral spalling of concrete. But no measures are given to combat thermo-mechanical spalling and thermo-chemical spalling. Multiple defense lines against fire-induced material deterioration (strength deterioration and three types of spalling) can be used in engineering. For example, hybrid PP and steel fibers can be used in UHPC columns to minimize thermo-hygral spalling and thermo-mechanical spalling.

Fire-proof coating and hybrid PP and steel fibers can be used simultaneously in UHPC tunnel linings, considering much more intense hydrocarbon fire scenarios and economic loss as a result of failure of a tunnel.

5.6 Summary

This chapter presents a new perspective on fire-induced spalling in concrete. The main conclusions are summarized as follows.

- There are three types of fire-induced concrete spalling depending on the mechanisms, viz., thermo-hygral, thermo-mechanical, and thermo-chemical spalling.

- Thermo-hygral spalling is induced by moisture clogging and pore pressure buildup inside heated concrete. It typically occurs within 220 ℃ and 320 ℃ (concrete temperature at the spalled location).

- Thermo-mechanical spalling is caused by applied stress and restraint-induced thermal stress in heated concrete. It typically occurs within 430 ℃ and 660 ℃ (concrete temperature at the spalled location).

- Thermo-chemical spalling is related to decomposition of hydrated products and calcite, and rehydration of calcium oxide. It typically occurs at or after temperature greater than 750 ℃ (concrete temperature at the spalled location).

- There is strong interaction among these three types of spalling. There is a lack of research work on spalling behavior of stressed or restrained concrete specimens, especially on full-scale structural members. Test results on stressed or restrained concrete is much more useful for designing structural concrete against thermal spalling.

- There is a lack of research work on post-cooling spalling, although it is a potential threat to post-fire performance of concrete structures.

- Current codes of practice only recommend protective measures against thermo-hygral spalling. Countermeasures against these three types of spalling

are presented in this chapter. The concept of "multiple defense line against fire-induced concrete spalling" is introduced for the highest level of protection.

● Future predictive tools aiming to assess spalling risk and to determine spalling extent should consider all three types of spalling and interactions among them.

CHAPTER 6. THERMO-HYGRAL SPALLING RESISTANCE OF DFRCC

6.1 Introduction

The previous chapter advanced a unified fire-induced concrete spalling theory, in which fire spalling of concrete is categorized into three types based on distinct driving mechanisms. They are thermo-hygral spalling, thermo-mechanical spalling, and thermal-chemical spalling, respectively. Among them, thermo-hygral spalling reduces load-bearing capacity of concrete members in the early stage of a fire, making it one of the most detrimental problems for concrete in fire condition. This chapter presents an experimental program to assess thermo-hygral spalling resistance of DFRCC and the role of hybrid fibers in resisting thermo-hygral spalling. Thermo-hygral spalling resistance was evaluated by conducting 1D spalling tests. To gain an in-depth insight into the role of PVA fibers to mitigate thermo-hygral spalling, hot permeability measurements, microstructure analysis, and Energy Dispersive X-Ray (EDX) analyses were conducted.

6.2 Materials and method

6.2.1 Materials

Two mixes were prepared in this study. One was the optimized DFRCC mix developed in Chapter 3 (i.e., mix M6 in Table 3.5), and the other was cementitious mortar. The optimized DFRCC and mortar mixes are given in Table 6.1. The DFRCC matrix has the same composition as the mortar. However, the DFRCC incorporates PVA and steel fibers. This is to study the roles of fibers, especially

PVA fibers, in resisting thermo-hygral spalling by comparing the behaviors of DFRCC and mortar under elevated temperature.

Table 6.1 Mix Proportions of DFRCC and mortar*

Mix name	Cement	Fly ash	Sand	Water	PVA fiber	Steel fiber	Superplasticizer
DFRCC	1	1.22	1	0.62	1.50%	0.50%	0.011
Mortar	1	1.22	1	0.62	-	-	0.011

* Content of fibers is written as volume fraction of the mixture, while all the other ingredients are written as weight proportion of cement.

The preparation of the DFRCC and the mortar follows a similar procedure specified in Section 3.2.3.

6.2.2 1D spalling test

For 1D spalling tests, two 200mm×200mm×140mm block specimens were used. One was made of DFRCC, and the other was prepared using the mortar. The 1D spalling test setup is shown in Fig. 6.1. Both moisture transfer and heat transfer were confined in the thickness direction of the specimen block. To ensure 1D moisture transfer, high-temperature silicone was applied on four faces of the block followed by copper foil wrapping. To ensure 1D heat transfer, the block was wrapped with rock wool on four faces (see Fig. 6.1). The specimen was then placed on the furnace opening with the interior face exposed to heating and the exterior face to ambient environment. A perforated steel cage was attached inside the furnace to keep the spalled debris from damaging the electric furnace. The applied heating curve followed the ISO 834 standard fire curve up to 600 ℃ (Han and Lin 2004). Then this temperature was kept constant and the heating duration was set to 2.5 hours so that explosive spalling, if occurred, would take place in this duration. Type K thermocouples were embedded in the center of the block specimen at a depth of 10, 20, 30, 40 and 50mm from the interior heated face. The tests were conducted on the specimens after air curing in laboratory for 56 days.

(a) View of test setup   (b) Sketchup of 1D spalling test
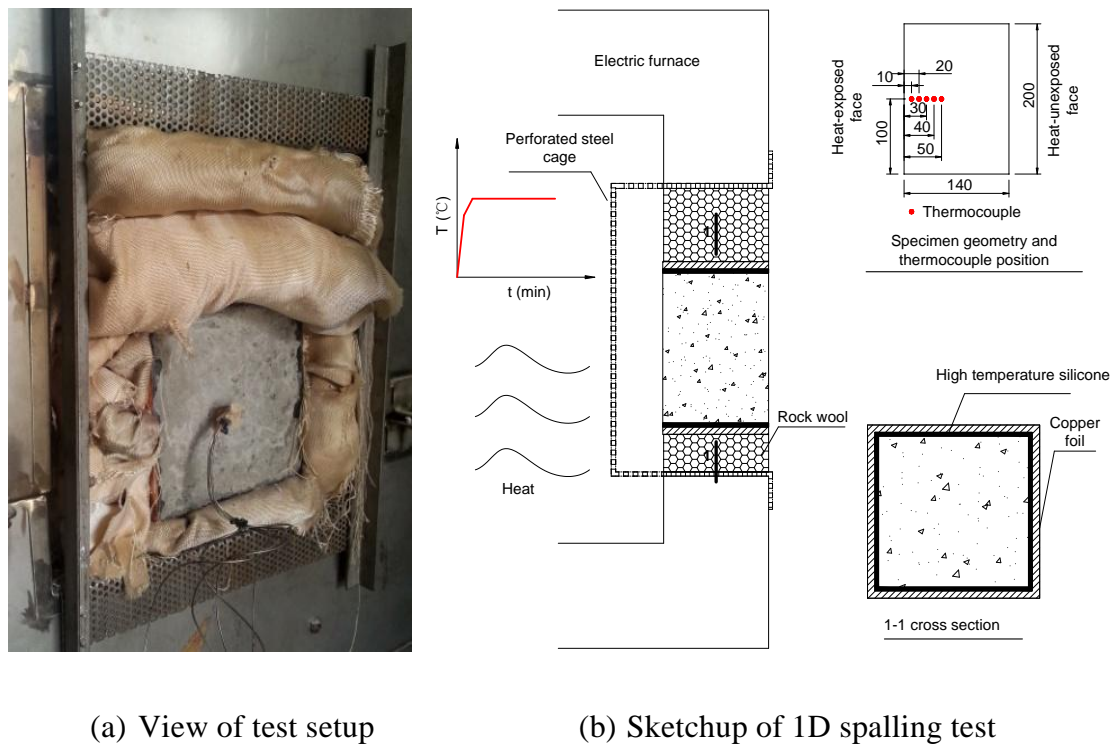
Fig. 6.1 1D spalling test setup

6.2.3 Thermal property test

Thermal conductivity, heat capacity and thermal diffusivity of SHCC and mortar were measured using a Hot Disk TPS 2500S thermal constant analyzer. This equipment uses a transient plane source (TPS) technique to measure thermal properties of materials (Kodur and Khaliq 2010). A flat source Kapton sensor was placed between one pair of disk specimens as shown in Fig. 6.2. Then a constant heating power was applied, the temperature in the sensor rose and heat flowing started in the specimen. Thermal conductivity, heat capacity, and thermal diffusivity were analyzed and recorded by the data acquisition system. Three pairs of cylinder specimens (ϕ150 mm $\times$ 40 mm) were prepared for measuring thermal properties of DFRCC and mortar, respectively.
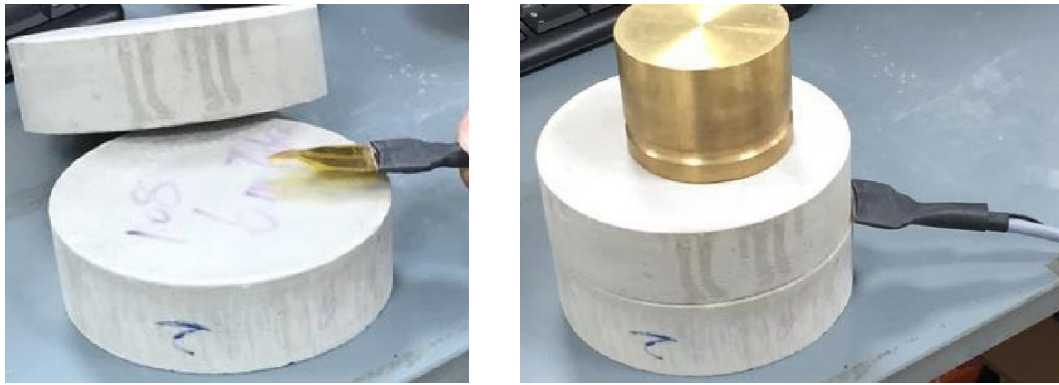
(a) Kapton sensor being placed between two specimens

(b) Kapton sensor in position ready for testing

Fig. 6.2 Senor positioning before thermal property measurement

6.2.4 Water porosity test

The evolution of water porosity is studied to understand the role of PVA fibers. Cube specimens with an edge length of 50 mm were prepared for water porosity test. To remove the influence of moisture, all the specimens were dried at 105 ℃ until constant mass was achieved. Porosity was measured after exposure to 105, 150, 200, 250, and 300 ℃, since thermo-hygral spalling most likely occurs within this range of temperature. The samples were heated to these target temperature levels at 1 ℃/min, and the heating was not stopped until the masses of the samples became constant. Porosities of samples were calculated according to ASTM C642 (2013) via Eqn. (6.1), where $m_{dry,T}$ is the sample mass heated under a constant target temperature T to constant mass (measured after cooling), $m_{sat,T}$ is the heated sample mass saturated with water and V is the sample volume calculated by measuring sample dimensions with a Vernier scale.

$$p = \frac{m_{sat,T} - m_{dry,T}}{V} \times 100\%$$
(6.1)

6.2.5 Hot permeability test

Apparent permeability was measured according to the Cembureau method, which is easy to operate and reasonably accurate (Kollek 1989). The test device and experimental setup for measuring high-temperature permeability of DFRCC are shown in Fig. 6.3 and Fig. 6.4. Cylinder specimens with a height of 40mm and a diameter of 150mm were prepared for initial and residual permeability tests. The hot permeability tests were conducted after the specimens were cured for at least 90 days. The test specimen was placed inside the pipe segment which was sandwiched in between the upper lid and the lower lid. Bolts and nuts were used to assemble and tighten the upper lid, lower lid and pipe segment. High-temperature sealant was used to seal the gaps between the test specimen and the lids in case that air flow escaped from the gaps and did not penetrate into the specimen. There is one leakage hole in both the upper and lower lids. The purpose of these two openings is to check leakage conditions at ambient temperature. After confirming that there is no leakage, the upper lid is connected to a compressor through a steel tube, and the lower lid is connected to an air bubble counter through a steel tube.
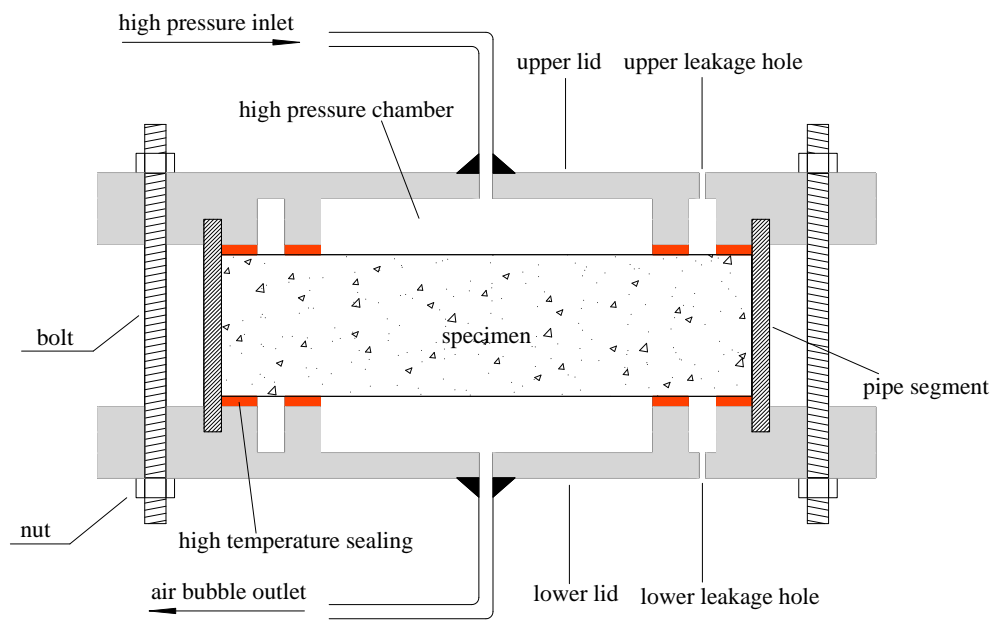
Fig. 6.3 Sectional view of test device for measuring hot permeability

Fig. 6.4 Hot permeability setup

The apparent permeability value was calculated according to Darcy's law as modified by the Hagen-Poiseuille relation (Gallé and Sercombe 2001):

$$k_a = \frac{Q}{A} \frac{2\mu L p_{atm}}{\left(p_i^2 - p_{atm}^2\right)}$$

(6.2)

where k_a is the apparent permeability, Q is the gas flow rate, A is the specimen cross-sectional area, p_i is the inlet pressure, p_{atm} is the outlet pressure equal to atmospheric pressure, L is the length of a specimen, μ is the dynamic viscosity of the gas used.

Viscous flow and slip flow occur during gas percolation through a tight porous media. When the average pore diameter is large compared to the mean free path of gas molecules (average distance between collision), viscous flow plays a major role. However, when the average pore size is of the same order of magnitude as the mean free path of gas molecules, slip flow cannot be neglected (Sun et al. 2015). The mean free path of gas molecules is influenced by pressure levels. Therefore, the gas transport and the measured permeability value are dependent on pressure levels. Klinkenberg proposed a correction factor to take account of the influence of pressure (Klinkenberg 1941). Consequently, the relation between apparent permeability and intrinsic permeability can be written in the following form:

$$k_a = k_{int}\left(1 + \frac{b}{p_m}\right)$$

(6.3)

where k_{int} is the intrinsic permeability when the mean pressure p_m approaches infinity, b is the Klinkenberg constant, and $p_m = \left(p_i + p_{atm}\right)/2$ is the average value of the inlet and outlet pressures on the two sides of the specimen.

Test procedure for measuring the hot permeability of DFRCC and mortar specimens is presented in Fig. 6.5. Permeability was first measured at ambient

temperature. To remove the influence of moisture, all the specimens were dried at 105 ℃ until constant in mass. Permeability was measured at temperature levels of 105, 150, 200, 250, and 300 ℃, since thermo-hygral spalling most likely occurs within this range of temperature. The heating rate was set to be 1 ℃/min to minimize temperature gradients and thermal stresses developing inside the specimen. After reaching the prescribed temperature level, the temperature was kept constant for two hours to reach an isothermal steady state. At temperature levels lower than 200 ℃, three different pressure levels (9 bar, 6 bar, and 3 bar) were applied to calculate intrinsic permeability. For higher temperature levels, lower pressure levels (5 bar, 4 bar and 3 bar) were adopted so that gas flow rate was measurable and good tightness was maintained. One complete measurement at one temperature level took about 18 to 36 hours. This was to remove the influence of dehydrated water released from the specimen on the permeability. The air volume coming from the outlet pipe was measured every 60 min. Permeability at one temperature level was finalized when the air flow rate became steady, i.e. when three consecutive readings were constant.

```
┌──────────────┐
│ Prepare the  │
│  specimens   │
└──────────────┘
        │
        ▼
┌──────────────┐
│ Assemble the test │
│  device with the  │
│ specimen inside   │
└──────────────┘
        │
        ▼
┌──────────────┐
│    Check     │
│ tightness of │
│  the device  │
└──────────────┘
        │
        ▼
┌────────────────────────┐
│ Heat the specimen to target │◄──┐
│ temperature and maintain at that │   │
│       temperature       │   │
└────────────────────────┘   │
        │                     │
        ▼                     │
┌──────────────┐             │
│ Apply the air │             │
│ pressure by the│            │
│  compressor  │             │
└──────────────┘             │
        │                     │
        ▼                     │
┌──────────────┐             │
│ Measure the volume of │──────┘
│  air bubbles out in a │
│  fixed time range  │
└──────────────┘
        │
        ▼
┌──────────────┐
│ Finish the test │
└──────────────┘
```
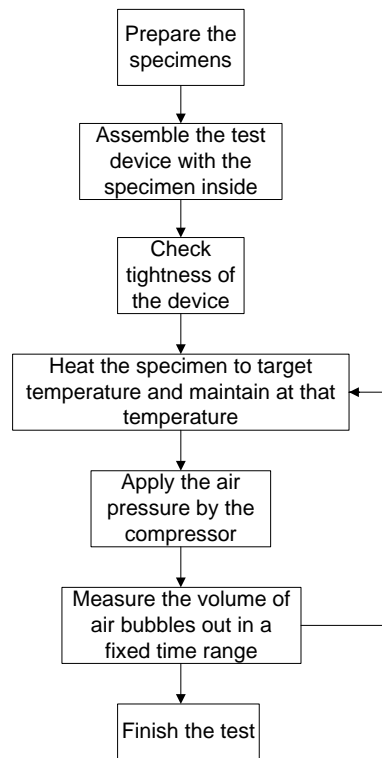
Fig. 6.5 Procedure for measuring hot permeability

6.2.6 Microstructure

To study the behavior of fibers and fiber/matrix interaction before and after melting of PVA fibers, observations were made on one polished DFRCC sample that was subjected to elevated temperature levels (30, 105, 150, 200, 250, and 300 ℃) via a Field Emission Scanning Electron Microscope (FE-SEM). The same heating rate of 1 ℃/min used for porosity and permeability tests was also adopted here.

To study where the melted PVA fibers have gone, i.e. (a) left in the fiber channel bed, (b) partially attached to the channel wall and partially penetrated to neighboring matrix around the channel or (c) simply diffused into the matrix, Energy Dispersive X-ray (EDX) was used to track the location of melted products of PVA fibers.

6.3 Results and discussion

6.3.1 1D spalling test

The temperature evolutions of mortar and DFRCC specimens at different distances from the interior heated surface are given in Fig. 6.6 and Fig. 6.7, respectively. The thermocouples embedded at 50 mm from the heated surface for both specimens were damaged prior to testing, and the thermocouple to measure the fire temperature for the mortar specimen was also damaged during the spalling test, as seen in Fig. 6.6. For both specimens, as expected, the temperature at 10 mm away from the heated face was the largest, followed by recorded temperatures at 20, 30 and 40mm from the interior heated face. What was distinctive between these two specimens was that the mortar specimen suffered thermo-hygral spalling during heating. In contrast, the DFRCC specimen did not spall at all during the process. Progressive spalling of the mortar specimen was accompanied by a series of popping sounds. The first popping sound was heard at about 8th min of heating and the last at 130th min. It was interesting to observe that after each popping sound there was a decrease of temperature and then an increase in temperature, as indicated in Fig. 6.6. This phenomenon was possibly induced by the "moisture clog" inside the mortar specimen. The condensed liquid water near the spalling region was transformed to superheated vapor fairly quickly (Fig. 6.8), which consumed a lot of heat. This led to a temporary decrease in the temperature of the specimen. Upon further heating and with parts of the fire-exposed surface spalled off, temperature of the specimen quickly bounced back and continued increasing.
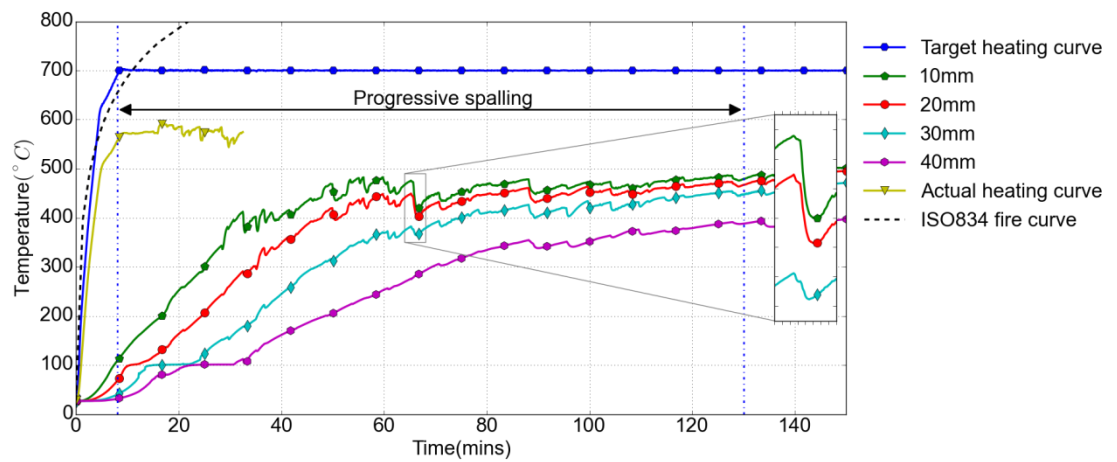
Fig. 6.6 Temperature evolutions of mortar specimen at different distances from the heated face
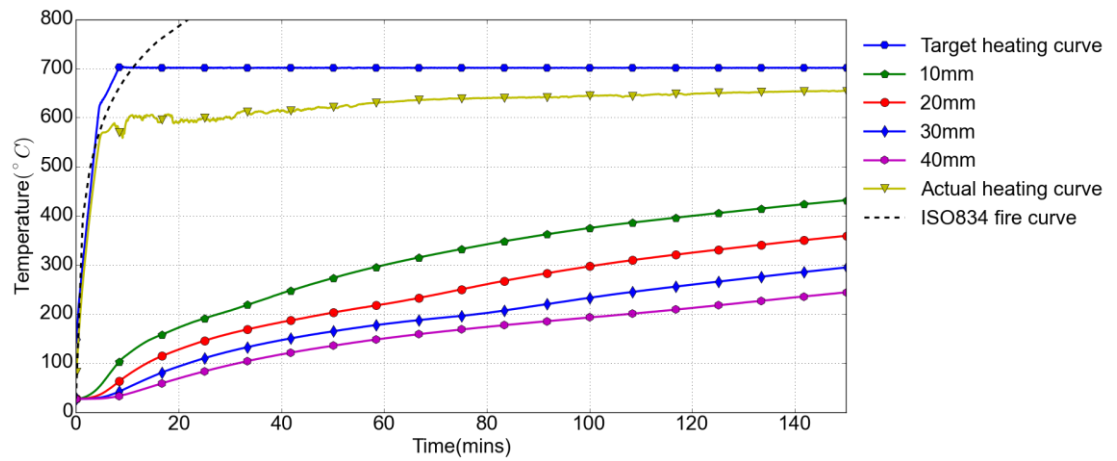
Fig. 6.7 Temperature evolutions of DFRCC specimen at different distances from the heated face
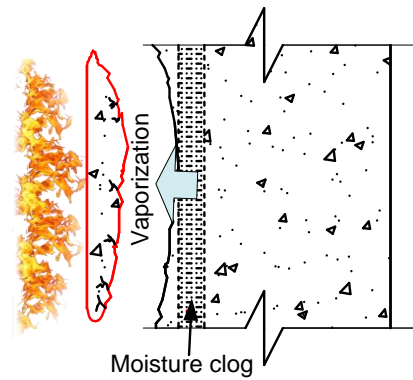
Fig. 6.8 Vaporization of liquid water near the spalled surface

Fig. 6.9(a)-(d) plot the comparisons between temperature evolutions of mortar and DFRCC specimens at different distances from fire-exposed surface. At 10 mm, the temperatures of both specimens were almost the same before the occurrence of first spalling as shown in Fig. 6.9(a). This is due to similar values of thermal diffusivity of mortar and SHCC which governs heat conduction inside the specimens. Thermal conductivities, volumetric heat capacities and thermal diffusivities of mortar and SHCC measured by TPS2500S hot disk device are listed in Table 6.2. After the first spalling, the temperature of mortar specimen rose sharply, increasing the temperature difference between mortar and DFRCC specimens. Until about 60 min after heating, the temperature increase of mortar specimen became small and the temperature difference between mortar specimen and DFRCC specimen gradually decreased with time. At the end of heating, the temperature difference at 10mm was 71 ℃. Similarly, at 20, 30 and 40mm, the temperatures of both specimens were almost the same before the occurrence of first spalling. After the first spalling, the temperatures of mortar specimen at these three locations rose sharply. For mortar specimens, there was a temperature plateau at about 100 ℃. However, for DFRCC specimens no obvious temperature plateau was observed. At 20 mm, the temperature plateau in the mortar specimen lasted for only 2 min as shown in Fig. 6.9(b). At 30 mm and 40 mm, the temperature plateau lasted about 9 min as shown in Fig. 6.9(c)-(d). This temperature plateau was caused by latent heat due to phase

change of water from liquid to vapor at about 100 ℃ inside the mortar specimen, which was beneficial in delaying the temperature rise. Subsequently, the temperatures at 20, 30 and 40mm from the heated face increased rapidly, enlarging the difference in temperature between the mortar and the DFRCC specimens. At the end of heating, the temperature differences at 20, 30 and 40mm were 136, 177 and 153 ℃, respectively.

(a) 10 mm

(b) 20 mm

117
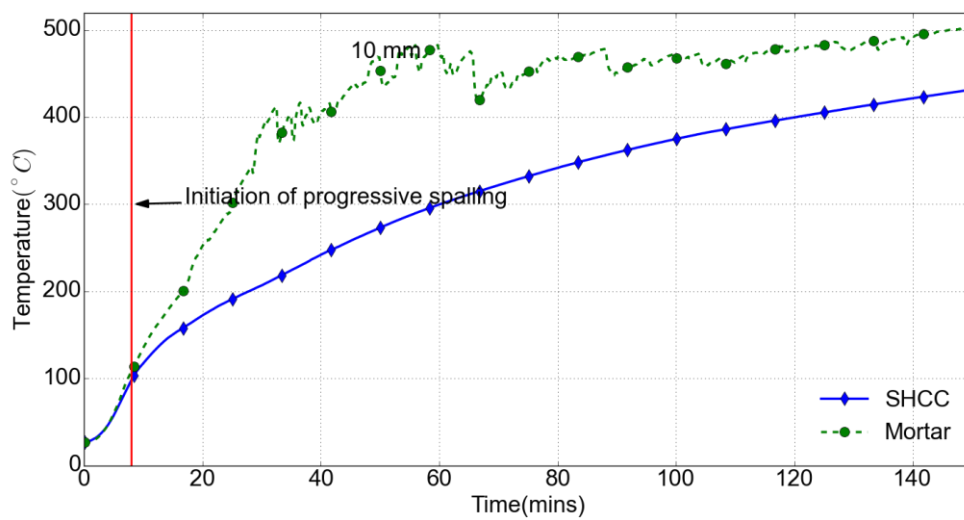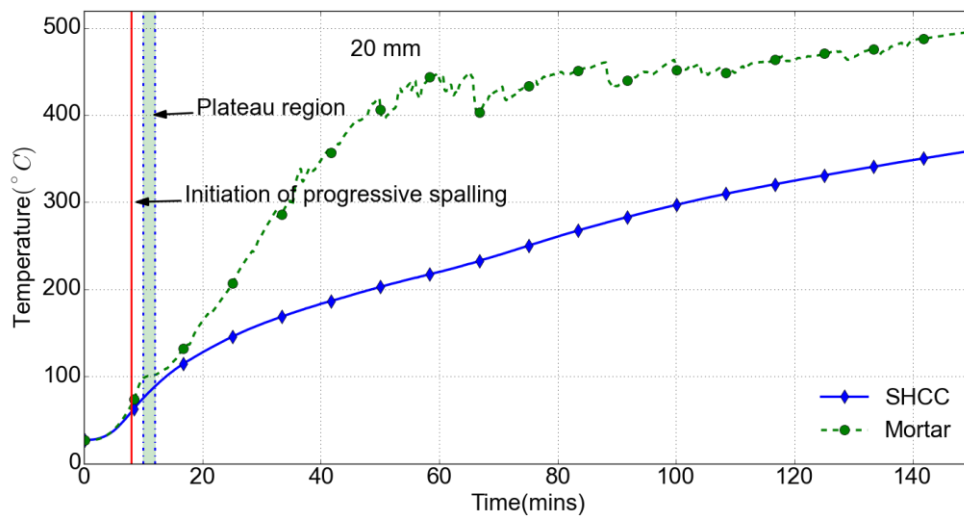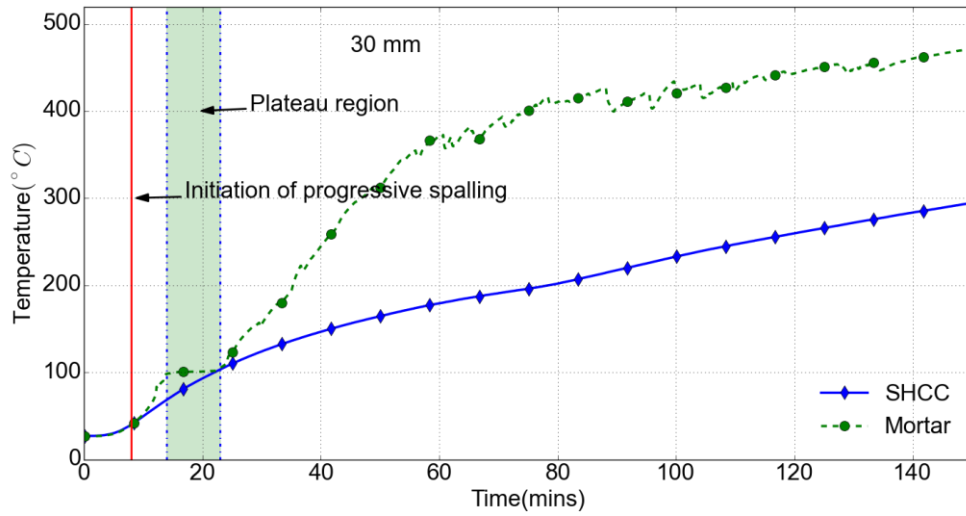
(c) 30 mm
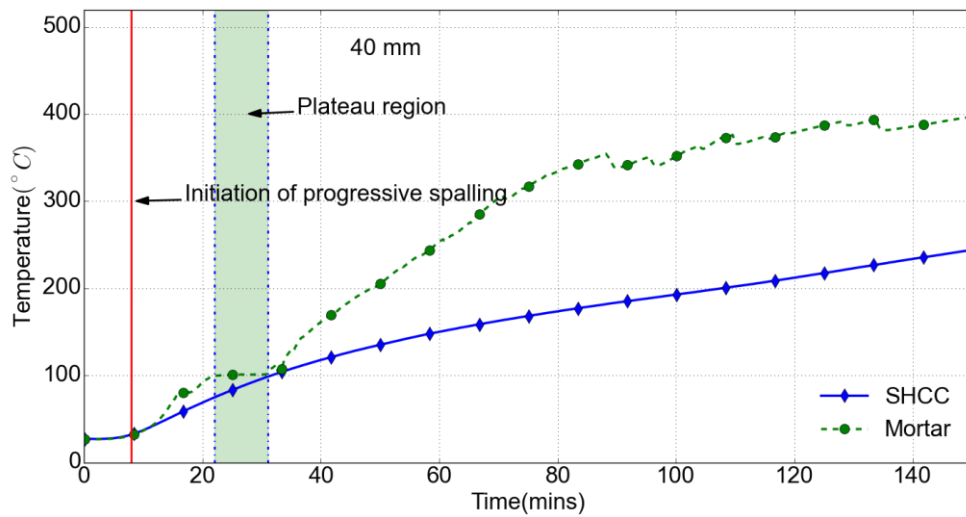
(d) 40 mm

Fig. 6.9 Temperature evolutions of DFRCC specimen and mortar specimen at different distances from fire-exposed surface

The mortar and DFRCC specimens after the spalling tests are shown in Fig. 6.10(a) and (b). It can be seen that a large portion of mortar block spalled off, while DFRCC specimen remained intact. Fig. 6.11 shows the spalling depth contour of mortar specimen. The spalling depths were measured at intervals of 25 mm and from this result the spalling depth contour was plotted. A further visual inspection of the

mortar block showed that two criss-crossing cracks penetrated the specimen depth. This test showed that spalling can lead to a rapid temperature increase and consequently an earlier failure. The hybrid PVA and steel fibers were effective in preventing thermo-hygral spalling of the DFRCC specimen under thermal exposure. It is because DFRCC has a larger hot permeability than mortar as evidenced by the hot permeability results in Section 6.3.3. Large permeability facilitated the release of vapor pressure inside the DFRCC specimen and at the same time mitigated the development of peak pore pressure.

Table 6.2 Thermal properties of Mortar and SHCC

Material	Thermal conductivity (W/mK)	Thermal diffusivity (mm^2/s)	Volumetric heat capacity (MJ/m^{3}K)
Mortar	1.60	0.83	1.93
SHCC	1.38	0.82	1.68

(a) Mortar specimen   (b) DFRCC specimen
Fig. 6.10 Mortar specimen and DFRCC specimen after spalling tests
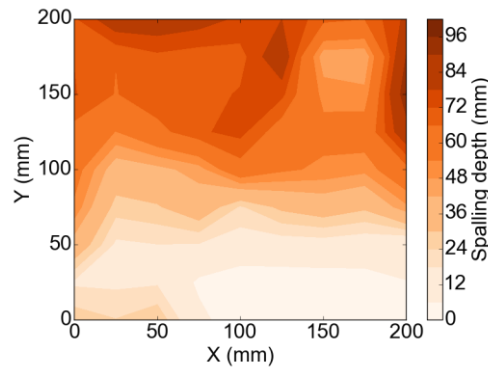
Fig. 6.11 Spalling depth contour of mortar specimen

6.3.2 Water porosity

Porosity values of DFRCC and mortar are displayed on Fig. 6.12 as a function of temperature. As expected, water porosities of DFRCC and mortar increase with temperature. This porosity increase is mainly caused by dehydration of cementitious matrix. However, it is noted that the initial porosity of DFRCC (23.4%) is larger than that of mortar (21.9%). This is due to air voids induced by addition of a large volume of fibers (2% volume) in DFRCC. After exposed to 300 ℃, the porosity of DFRCC becomes 27.8% and the porosity of mortar becomes 26.0%. The porosities of DFRCC and mortar increase by 4.4% and 4.1%, respectively. The melting point of PVA fibers is about 240 ℃ as shown in differential scanning calorimetry (DSC) in Fig. 6.13. This means PVA fibers in DFRCC melt after exposure to 300 ℃. However, there is little difference in porosity increases for DFRCC and mortar. Hence, the melted products from PVA fibers still remain inside DFRCC, which is corroborated by the TG result of PVA fiber as shown in Fig. 6.13. TG and DSC results were performed with a constant heating rate of 1 ℃/min in nitrogen flow (20mL/min).
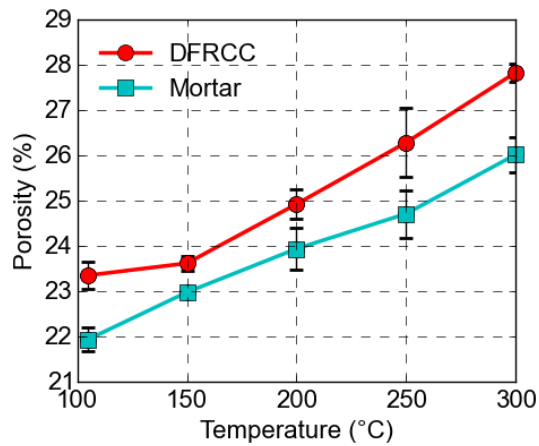
Fig. 6.12 Water porosity versus heat treatment
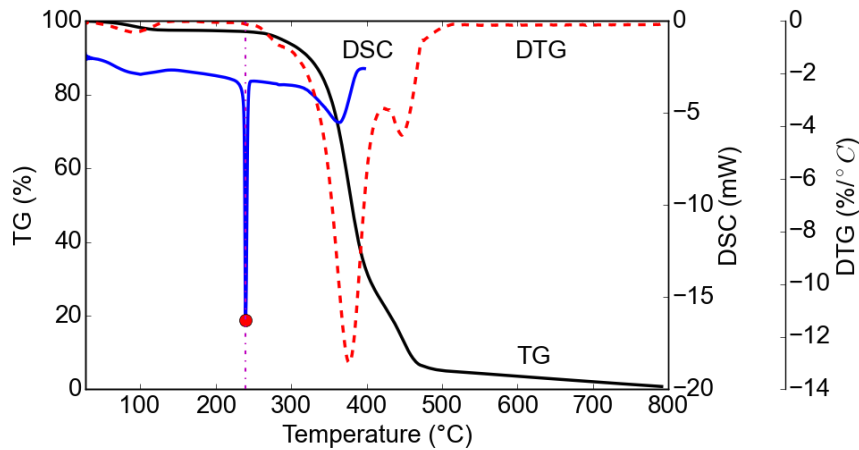
Fig. 6.13 TG and DSC results of PVA fiber

6.3.3 Hot permeability

Fig. 6.14 shows the intrinsic permeability values of DFRCC and mortar versus temperature. Each point in the figure represents the average permeability value measured from three specimens of the same mix. The intrinsic permeability is calculated based on the Klinkenberg relationship described in Section 6.2.5. As an illustration, Fig. 6.15 shows the evaluation of intrinsic permeability of DFRCC at 200 ℃ from the apparent permeability values at three different pressure levels. Intrinsic permeability values of mortar at 250 ℃ and 300 ℃ are not shown in the figure. This is because the pressure level could not be maintained during the

measurement. After cooling down, micro-cracks were visible on the surface of the mortar specimen as shown in Fig. 6.16. Therefore, the apparent permeability values of mortar at 250 ℃ and 300 ℃ could not be measured using current testing method.
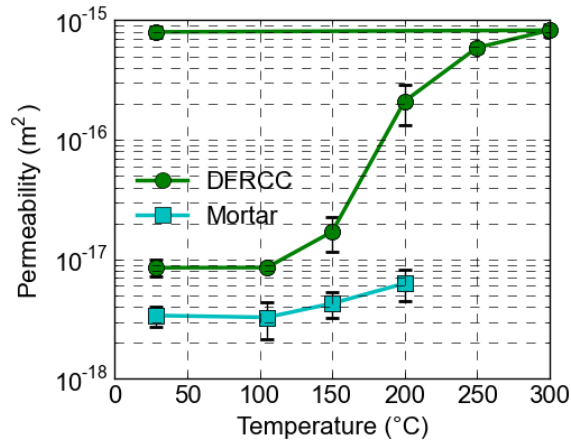
Fig. 6.14 Intrinsic permeability values of DFRCC and mortar versus temperature
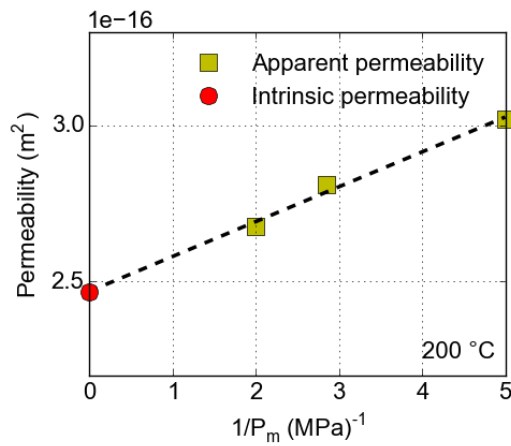
Fig. 6.15 Evaluation of intrinsic permeability of DFRCC at 200 ℃ based on Klinkenberg method

Fig. 6.16 Micro-cracks on the surface of a mortar specimen

As shown in Fig. 6.14, permeability values of DFRCC and mortar at 105 ℃ remain almost the same as those at ambient temperature. But the permeability of DFRCC at ambient temperature is larger than that of mortar at ambient temperature. This is probably caused by addition of 2% volume of fibers, since DFRCC has a higher porosity than mortar as shown in Fig. 6.12. Meanwhile, it is noted that the initial porosity of DFRCC (23.4%) is 1.5% more than that of mortar (21.9%), while the initial permeability of DFRCC (8.51e-18 m^2) is more than two times the initial permeability of mortar (3.39e-18 m^2). Therefore, in addition to total porosity, pore size distribution also plays an important role in determining permeability of DFRCC.

At temperature higher than 105 ℃, different trends in hot permeability values of DFRCC and mortar can be observed. From 105 ℃ to 150 ℃, hot permeability of DFRCC increases by 99.2%, while hot permeability of mortar increases by 30.8%. From 150 ℃ to 200 ℃, hot permeability of DFRCC increases by about 11 times. In contrast, hot permeability of mortar increases by only 47.1%. According to the DSC result of PVA fiber shown in Fig. 6.13, the melting point of PVA fiber is about 240 ℃. It means a large increase in permeability of DFRCC occurs before PVA fibers actually melt. Previous work concluded that explosive spalling of

DFRCC was reduced due to melting of PVA fibers (Sahmaran et al. 2010). However, from the hot permeability test results, it can be concluded that factors other than melting of PVA fibers contribute to combat explosive spalling.

According to unified fire-induced concrete spalling theory proposed in Chapter 5, thermo-hygral spalling of concrete tends to occur between 220 ℃ and 320 ℃. Therefore, the results presented in Section 6.2.2 can be explained by the evolution of hot permeability with temperature. Before 200 ℃, there is a tremendous increase in hot permeability of DFRCC. In contrast, there is little change in hot permeability of mortar. In addition to that, the initial permeability of DFRCC is 8.51e-18 m^2, which is more than twice that of mortar (3.39e-18 m^2). Therefore, the relatively larger initial permeability of DFRCC and the tremendous increase in its permeability before thermo-hygral spalling temperature range explained why DFRCC was free from explosive spalling.

6.3.4 Microstructure

Fig. 6.17 shows an SEM image of an unheated DFRCC sample. There was interfacial transition zone (ITZ) around the PVA fibers, and the thickness of the ITZ was in a range of 200-600 nm. The ITZs around PVA fibers accounted for higher initial porosity and permeability of DFRCC relative to those of mortar as presented in Section 6.3.2 and 6.3.3. After being heated to 150 ℃, a slight increase in the ITZs around PVA fibers were observed, which accounted for the increase in permeability of DFRCC from 105 ℃ to 150 ℃.
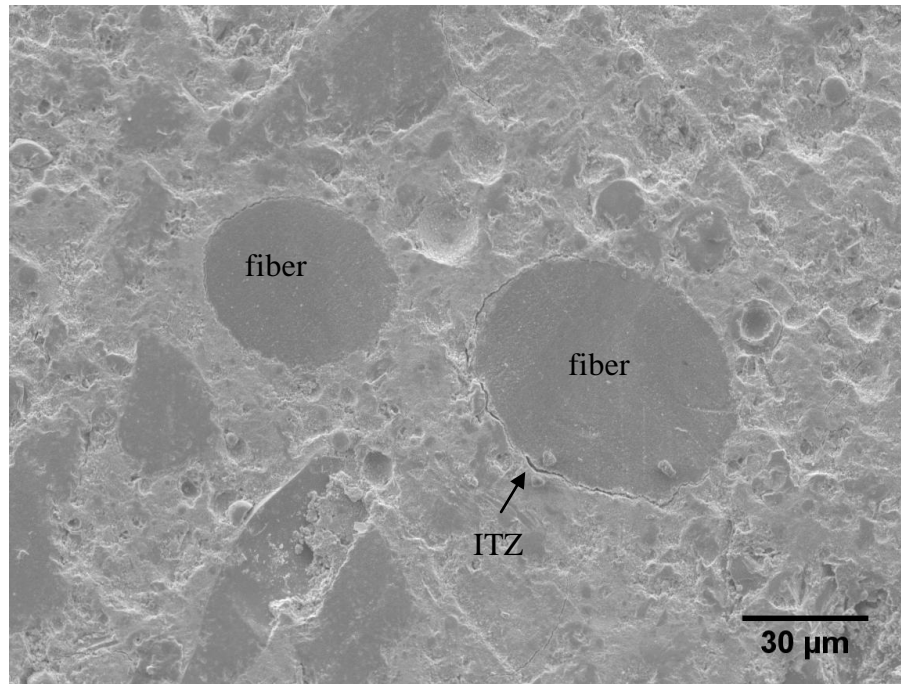
Fig. 6.17. SEM image of unheated DFRCC sample (500× magnification)

After heated to 200 ℃, shrinkage of PVA fibers was observed as shown in Fig. 6.18(a). In this case, disc-shaped empty spaces formed at the ends of the PVA fibers. On one hand, these empty spaces served as a 'reservoir' to store water vapor; on the other hand, they contributed to an increase in permeability from 150 ℃ to 200 ℃ as shown in Fig. 6.14. After exposure to 250 ℃, melted PVA fibers could still be found in their original fiber channels, although they could not maintain their original shape (Fig. 6.18(b)). After exposure to 300 ℃, PVA fibers were no longer in the fiber channels as shown in Fig. 6.18(c). However, residue from melted PVA fibers was found on the interior of fiber channel walls.
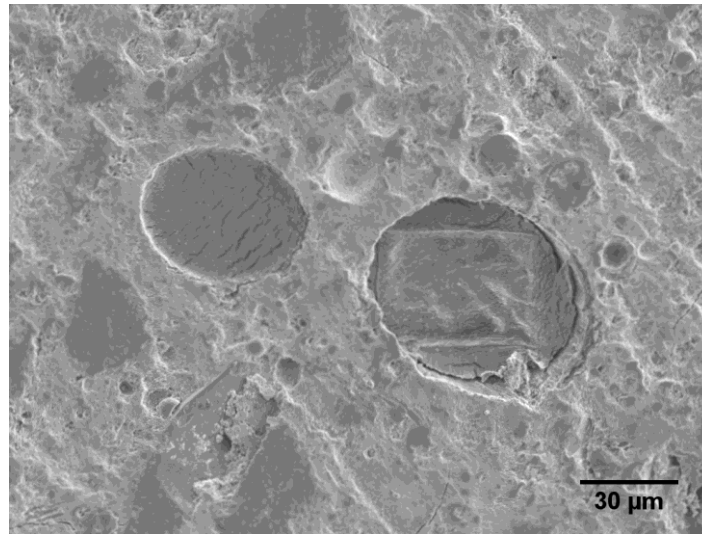
(a) 200 ℃
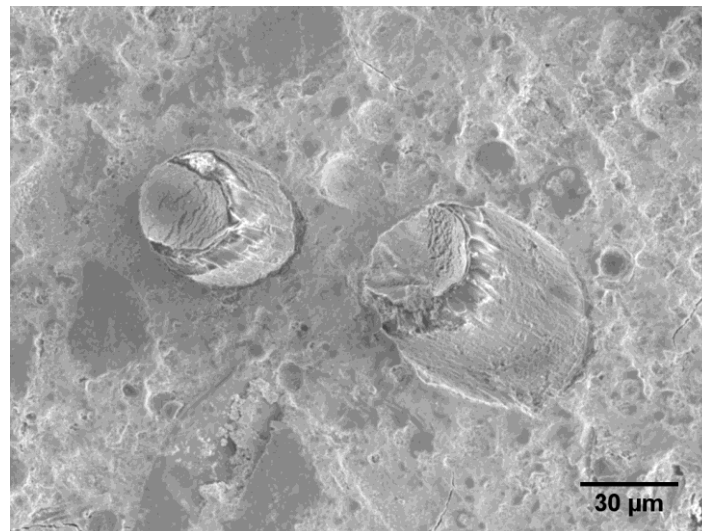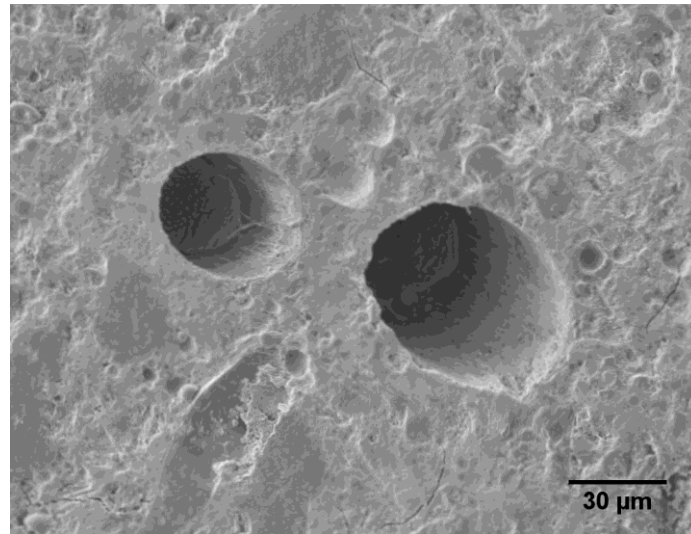
(b) 250 ℃

(c) 300 ℃

Fig. 6.18. SEM images of DFRCC sample after heated to (a) 200, (b) 250 and (c) 300 ℃

To find out where melted PVA fibers went after 300 ℃, EDX was used on the area shown in Fig. 6.18(c) to track the element distribution. The chemical structure for PVA is given in Fig. 6.19. PVA fibers are one source of carbon element in DFRCC. From the distribution of carbon element, the whereabouts of melted PVA fibers can be ascertained. Fig. 6.20 presents EDX elementary mapping of carbon corresponding to Fig. 6.18(c). Fig. 6.21 shows the corresponding EDX curve and elemental composition. It can be seen from Fig. 6.20 that the carbon element was well-dispersed in the matrix. High-concentration carbon element was also observed on the channel walls of fibers as shown in Fig. 6.18(c) and Fig. 6.20. This high-concentration carbon element was the products of melted PVA fibers. To confirm whether carbon element in the matrix was from PVA fibers, EDX was used on a region in a mortar sample (region A) and a region in the DFRCC sample where no PVA fibers were observed (region B). It was found that PVA fibers were not the only source of carbon element. The matrix itself also contained carbon element. And the atomic percentages of carbon element for region A and region B were approximately the same, 11.9 % and 11.6 %, respectively. Therefore, products of

melted PVA fibers were attached on walls of PVA fiber channels and did not diffuse through the matrix. The fiber channels offered connected paths for vapor to evacuate to the surface of the specimen. It was noted that the relative increase in hot permeability of DFRCC from 250 ℃ to 300 ℃ was not large (Fig. 6.14). This was reasonable, since a majority of melted products of PVA fibers were still in the fiber channels as shown by the EDX elemental mapping (Fig. 6.20) and TG curve of PVA fiber (Fig. 6.13).

$$\left[\begin{array}{cc} H & H \\ | & | \\ -C & -C- \\ | & | \\ H & OH \end{array} \right]_n$$
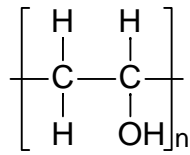
Fig. 6.19. Chemical structure for PVA
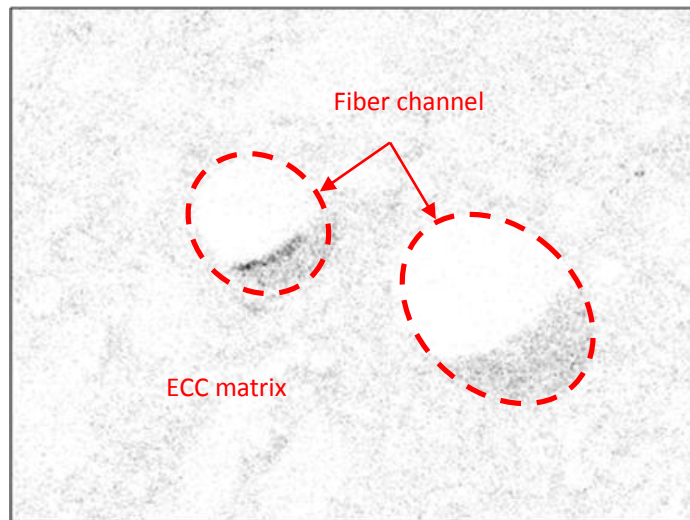
Fig. 6.20. EDX elemental mapping of carbon (denoted by black dots)
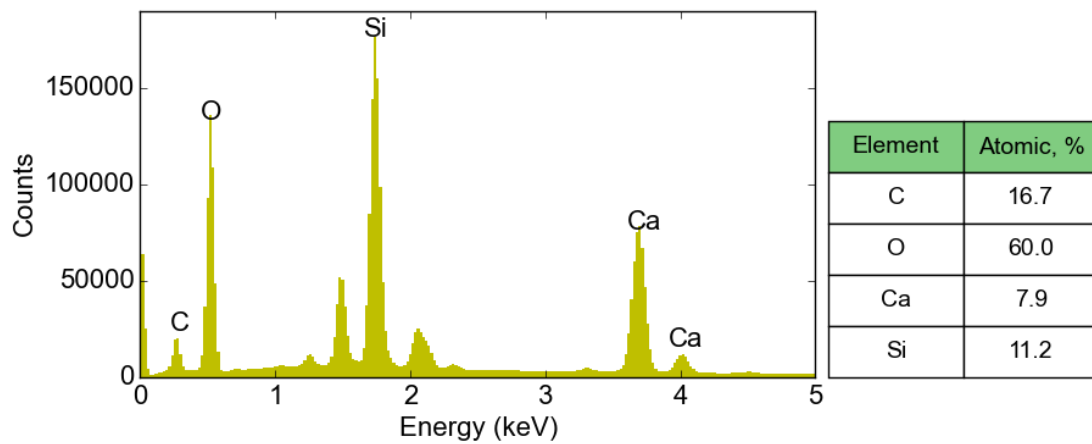
Fig. 6.21. EDX curve and elemental composition for the area shown in Fig. 6.18(c)

Re-examining SEM images of the DFRCC sample before and after heating to a target temperature (Fig. 6.17-Fig. 6.18) showed that there was no micro-crack around the perimeter of PVA fibers. Similar findings were observed around other PVA fibers in the sample. They were not shown here due to page limitation. Thus, clearly, thermal incompatibility between the PVA fibers and the matrix did not initiate micro-cracks around the fibers.

SEM observations were also made on a steel fiber in DFRCC before and after heating, as shown in Fig. 6.22(a)-(c). Before heating, no ITZ was found around the steel fiber (Fig. 6.22(a)). After heated to 200 ℃, no obvious change was found around the steel fiber (Fig. 6.22(a)). Steel fibers had a negligible contribution to the permeability increase from room temperature to 200 ℃ as shown in Fig. 6.14. After heated to 300 ℃, micro-cracks were observed around the steel fiber (Fig. 6.22(c)). This contributed to an increase in permeability of DFRCC at 300 ℃. Still, this contribution was rather limited considering the great changes in PVA fibers and the small amount of steel fibers present in the matrix (for every 57 PVA fibers, there was only 1 steel fiber). Overall, the contribution of steel fibers to the permeability increase in DFRCC (Fig. 6.14) was negligible. This conclusion was consistent with

previous experimental results, in which violent spalling was observed in UHPC with 195kg/m^3 steel fibers (Klingsch 2014).

(a) 30 ℃
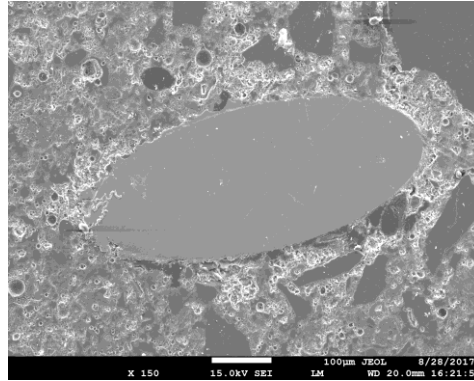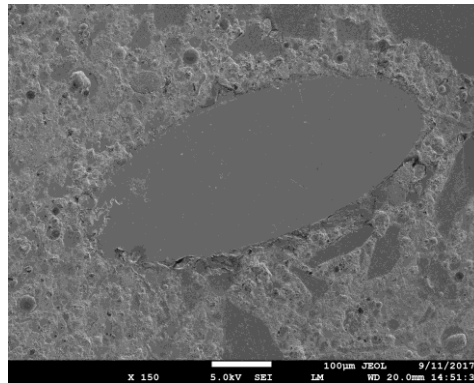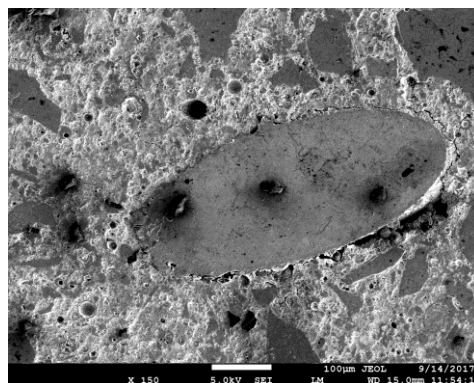
(b) 200 ℃

(c) 300 ℃

Fig. 6.22. SEM images of a steel fiber in DFRCC matrix after exposure to (a) 30, (b) 200, and (c) 300 ℃

6.4 Summary

Based on the study in this chapter, the following conclusions can be drawn:

● The addition of hybrid PVA and steel fibers is effective in resisting thermo-hygral spalling. The DFRCC specimen showed good spalling resistance under fire. In contrast, the mortar specimen suffered progressive spalling, ending in complete failure even without any mechanical load.

● The initial porosity and permeability of DFRCC are larger than those of mortar. The initial porosity of DFRCC is 23.4%, 1.5% more than that of mortar. However, the initial permeability of DFRCC is 8.51e-18 m^2, more than two times the initial permeability of mortar. A small increase in porosity can lead to a large increase in permeability. Therefore, in addition to total porosity, pore size distribution also plays an important role in determining permeability of DFRCC.

● There is little difference in porosity increases for DFRCC and mortar after exposure to 300 ℃. Therefore, a majority of melted products from PVA fibers are still present inside DFRCC, which is corroborated by the TG result of PVA fiber.

● The permeability values of DFRCC and mortar remain almost unvaried at 105 ℃ compared to at ambient temperature. However, the permeability of DFRCC quickly increases beyond 105 ℃, especially between 150 ℃ and 200 ℃. In contrast, the permeability of mortar increases slowly up to 200 ℃. Hot permeability of mortar at 200 ℃ is still of the same order of magnitude as that of mortar at room temperature. Beyond 200 ℃, micro-cracks were formed inside the mortar specimens, which made the measurements impractical.

● Permeability of DFRCC quickly increases from 150 ℃ to 200 ℃, before
   PVA fibers melt. Melting of PVA fibers does not play a critical role in
   reducing thermo-hygral spalling. After PVA fibers have melted, melted
   products are attached on fiber channel walls and cannot diffuse into the
   matrix.

● No microcracks initiated around the perimeter of PVA fibers up to 300 ℃.
   Increased ITZs around PVA fibers and voids formed at two ends of the fibers
   contribute to permeability increase in DFRCC, consequently spalling-free
   performance.

CHAPTER 7. MODELING THERMO-HYGRAL SPALLING OF CONCRETE AT HIGH TEMPERATURE

7.1 Introduction

As mentioned in CHAPTER 6, thermo-hygral spalling, often referred to as explosive spalling, is probably the most serious threat to safety of concrete structures under accidental fire conditions among the three types of thermal spalling, since it occurs in the very early stage of a fire. This is especially true for HPC and UHPC where spalling results in a rapid reduction of concrete section and exposes deeper layers of concrete to fire. In worse scenarios, thermo-hygral spalling exposes the rebars in the concrete directly to fire, leading to a premature failure of structural members. As HPC and UHPC are becoming more and more popular in construction, there is an urgent need to assess their thermo-hygral spalling risk. Relying solely on experimental method obviously goes against the increasing demand on performance-based approach to fire safety design of concrete structures. Hence, developing numerical methods to assess thermo-hygral spalling of concrete is urgently needed.

As reviewed in Section 2.4, many research efforts have been devoted to developing mathematical models for predicting thermo-hygral spalling of concrete under fire. However, some of the aforementioned models require complex material parameters, which are even more challenging to be measured experimentally. Besides, some models have not even been validated against experimental results. Therefore, other than experimental spalling tests, there is still a lack of reliable and yet simple models to predict moisture migration, pore pressure buildup, and assess explosive spalling risk of concrete.

This chapter presents the development of a simple 1D spalling model to predict thermo-hygral spalling of concrete based on the work done by Ichikawa and England (2004). The fundamental differences between the current model and the model proposed by Ichikawa and England (2004) are summarized as follows. In their model, liquid water is compressible. However, in the proposed spalling model, liquid water is assumed to be incompressible, which indicates the degree of saturation of concrete should not exceed 100% (Gawin et al. 2006). Besides, permeability and tensile strength of concrete are taken as a function of temperature in the proposed model, rather than constant values in Ichikawa and England (2004). The proposed model incorporates the effect of silica fume on proportions of concrete components and the effect of drying on moisture distribution. Water release patterns for chemically-bound water in the two models are also different.

The proposed model is then validated against five sets of experimental results: (a) moisture migration inside NSC; (b) pore pressure buildup inside NSC; (c) pore pressure buildup inside a HPC containment vessel; (d) pore pressure buildup inside a HPC slab; and (e) one-time explosive spalling of concrete. From the five comparison studies, it is shown that the proposed model can predict with reasonable accuracy moisture migration, pore pressure development, the first occurrence of spalling and approximated spalling location across the 1D specimens.

The developed 1D spalling model can be used in a wide range of concrete structures, such as tunnels, cooling towers, walls, slabs and containment vessels, as shown in Fig. 7.1. It provides an alternative means to assess thermo-hygral spalling risk of concrete under fire in addition to experimental studies. The numerical method is cost-effective and time-saving, obviating the need to conduct sophisticated finite element modeling which requires much more resources and more input parameters which cannot be measured experimentally. The proposed model can also be used to customize spalling-free concrete mixes in the preliminary stage of concrete mix

design. Further efforts are devoted to develop a performance-based spalling risk assessment method to be incorporated in the framework of performance-based fire safety design of concrete structures.
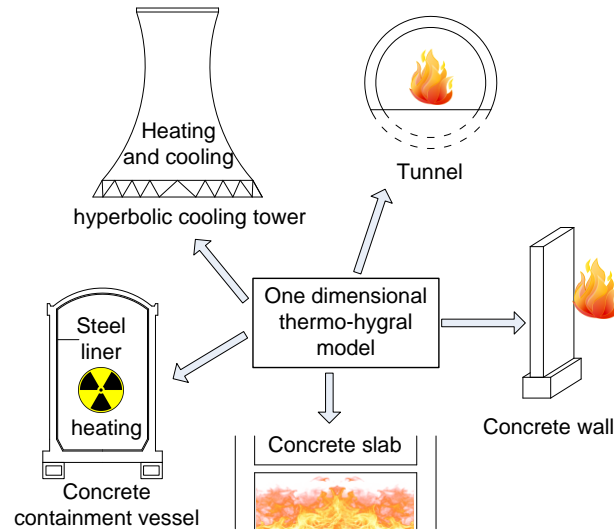
Fig. 7.1 Applications of 1D thermo-hygral spalling model for concrete

7.2 Numerical modeling

7.2.1 Discretization of model

A 1D numerical model is established to predict moisture transfer and pore pressure buildup across the concrete section under elevated temperature. To achieve this, the concrete section is discretized into a finite number of nodes as shown in Fig. 7.2. Total depth of the 1D concrete section is assumed to be L. Variable x represents the depth of a section from the fire-exposed side of concrete, with $x=0$ representing the fire-exposed face and $x=L$ the unexposed face.
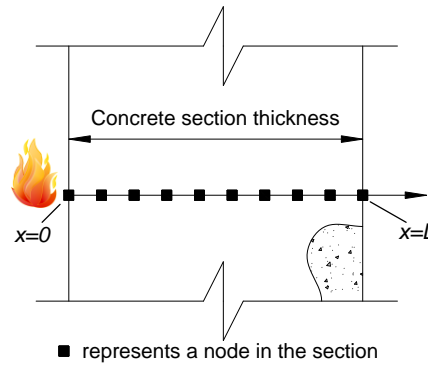
Fig. 7.2 Discretization of concrete section

7.2.2 Modeling of concrete components

It is worth noting that concrete is a porous material consisting of unhydrated cement, hydrated cement, aggregates, chemically-bound water, gel water, free water and empty pores. The corresponding masses and volumes of aforementioned components in a unit volume of concrete are determined using the formulas given in Appendix I. The spalling model proposed by Ichikawa (2000) applies the method developed by Powers and Brownyard (1946) to calculate the respective quantities of concrete components. However, the formulas proposed by Powers and Brownyard (1946) are mainly for cement-based systems. In this study, the formulas are extended to incorporate cement-silica fume blended systems based on Powers and Brownyard (1946) and Atlassi (1995). Then the model can be used for predictions of thermo-hygral spalling behavior of HPC.

7.2.3 Governing equations

When concrete is under fire, heat transfer and moisture migration occur inside concrete simultaneously. The 1D heat transfer governing equation is given by

$$\rho c \frac{\partial T}{\partial t} = \frac{\partial}{\partial x}\left(\lambda \frac{\partial T}{\partial x}\right) \tag{7.1}$$

where ρ is concrete density, c is specific heat of concrete, λ is thermal conductivity of concrete, T is temperature of concrete and t is time from the start of heating.

Moisture transfer within the concrete section is dominated by two flows, viz., diffusion-based flow governed by Fick's law and pressure-induced flow governed by Darcy's law. When concrete is under rapid heating, the diffusion-based flow is negligible. The change in moisture content should be equal to the sum of changes in moisture content due to pressure-induced flow and the gain in moisture content due to dehydration of concrete. Based on conservation of mass of water, the moisture transfer equation is given by Ichikawa (2000)

$$\frac{\partial m_{fw}}{\partial t} = \frac{\partial}{\partial x}\left(k \frac{\rho_{fw}}{\eta_{fw}} \frac{\partial p}{\partial x} \right) + \frac{\partial}{\partial t}\left(m_{gw-r} + m_{cw-r} \right) \qquad (7.2)$$

where m_{fw}, k, p, ρ_{fw}, η_{fw}, m_{gw-r} and m_{cw-r} represent mass of free water, permeability of concrete, pressure, density, dynamic viscosity of free water, mass of released gel water and mass of released chemically-bound water, respectively.

When one face of concrete section is under heating, there are three zones forming across the depth as shown in Fig. 7.3, namely, dry zone, wet zone, and saturated zone.
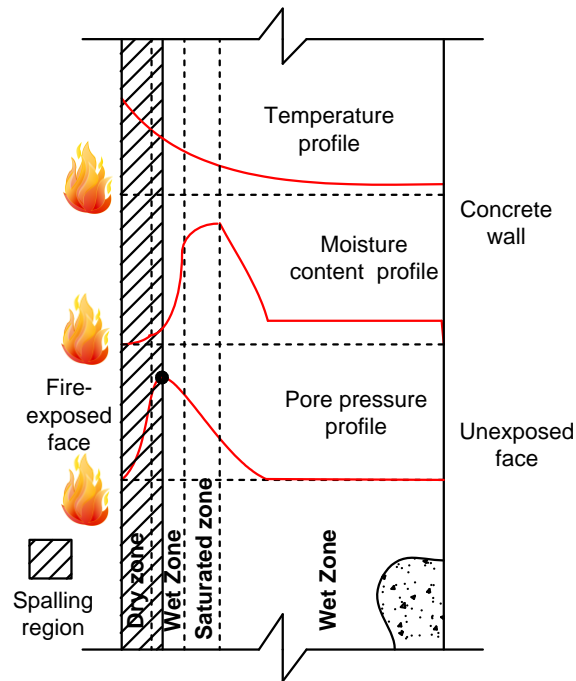
Fig. 7.3 Illustration of spalling mechanism of concrete under fire

When the calculated moisture content at a node exceeds the saturated liquid water content, excess moisture content is driven to adjacent nodes towards the unexposed side. When the calculated moisture content is negative at a node in the dry zone, the moisture content is redistributed linearly from the node to heat-exposed node based on conservation of mass of moisture content. Linear interpolation is used to determine the moisture content and pore pressure at the location in between two adjacent nodes.

7.2.4 Initial conditions

A uniform temperature (room temperature) distribution is taken as the initial condition of heat transfer analysis.

The initial distribution of free water and gel water is determined considering the effect of environmental conditioning affected by curing age and environmental

Relative Humidity (RH). Firstly, RHs at different times and at different distances from $x=0$ are calculated using Eqn. (7.3) proposed by Parrott (1988).

$$RH = 1 - (1 - e^{-At})(100 - RH_a)/100 \qquad (7.3)$$

$$A = 1.42/(d + 0.01)^2 \qquad (7.4)$$

where RH_a is ambient relative humidity, t is the time (days) after the start of drying, and d is the depth(mm) from exposed surface.

Then based on the relationship between RH and moisture content (Eqn. (7.5) to Eqn. (7.8)) proposed by Jiang and Yuan (2013), the initial relative moisture content distribution can be determined.

$$S = \frac{\lambda_1 \times RH/100}{(1 - \lambda_2 \times RH/100)(1 + \lambda_3 \times RH/100)} \qquad (7.5)$$

$$\lambda_1 = (2.9142w/c - 2.5849) \times T_a/1000 - 0.1994w/c + 0.1647 \qquad (7.6)$$

$$\lambda_2 = (2.907w/c - 1.1446T_a/10^3 + 1.5594T_a^3/10^5 + 4.4465)/10^3 \qquad (7.7)$$

$$\lambda_3 = (2.158w/c - 3.2774) \times T_a/1000 - 0.3272w/c + 0.3154 \qquad (7.8)$$

where S is the pore water saturation in concrete, w/c is water-to-cement ratio, and T_a is ambient temperature.

Finally, together with the respective mass of free water and gel water determined in Section 7.2.2, the initial distributions of free water and gel water can be determined.

Distribution of chemically-bound water is assumed to be uniform inside concrete and pore pressure distribution is uniform inside concrete and is set to 0 initially.

7.2.5 Boundary conditions

For the fire-exposed face, the boundary condition for heat transfer analysis is

$$-k\frac{\partial T}{\partial x} = h_f\left(T_f - T_{|x=0}\right) + \sigma\varepsilon_0\left(T_f^{\,4} - T_{|x=0}^4\right) \tag{7.9}$$

For the unexposed face, the boundary condition for heat transfer analysis is

$$-k\frac{\partial T}{\partial x} = h_e\left(T_{|x=L} - T_e\right) + \sigma\varepsilon_L\left(T_{|x=L}^4 - T_e^{\,4}\right) \tag{7.10}$$

where h_f and h_e are the respective heat transfer coefficients of the fire-exposed and unexposed faces; ε_0 and ε_L are surface emissivities at $x=0$ and $x=L$, respectively; $T_{|x=0}$ and $T_{|x=L}$ are temperatures at $x=0$ and $x=L$, respectively; σ is Stefan-Bolzmann constant.

For the fire-exposed face, the boundary condition for moisture transfer analysis is

$$m_{fw|x=0} = 0 \tag{7.11}$$

$$p_{|x=0} = 0 \tag{7.12}$$

For the unexposed face, the boundary condition for moisture transfer analysis is

$$m_{fw|x=L} = \phi_e \rho_{g,T} V_{p|x=L} \tag{7.13}$$

$$p_{|x=L} = \phi_e p_{svp,Ta} \tag{7.14}$$

where ϕ_e is the RH of the environment at the unexposed face, $\rho_{g,T}$ is the density of dry saturated water vapor at the temperature of T, $V_{p|x=L}$ is the pore volume at $x=L$, and $p_{svp,Ta}$ is the saturated vapor pressure at ambient temperature.

7.2.6 Permeability model

When concrete is under rapid heating, moisture inside the section cannot escape within a short time. Permeability of concrete is highly influenced by moisture content of concrete. The initial free water together with released water tends to reduce the permeability of concrete. A decrease in permeability of concrete has been observed between 175 ℃ and 275 ℃ (Klingsch 2014). The surface cracking of concrete was observed to occur at about 290 ℃ (Lin et al. 1996). Cracks significantly increase the permeability of concrete (Yildirim et al. 2015). Therefore, the normalized permeability model of concrete as shown in Fig. 7.4 is adopted for all 5 case studies. The permeability of concrete is constant from room temperature to 290 ℃ for simplification. Greathead (1986) showed that permeability of concrete drying at 400 ℃ increased more than 1000 times relative to that at ambient temperature. In this proposed model, from 290 ℃ to critical temperature of water (374 ℃), it is assumed that permeability increases log-linearly to 1000 times of its initial value. From 374 ℃ onwards, permeability remains constant. Although permeability still increases beyond 374 ℃, further increasing permeability has little influence on the pore pressure dissipation. Hence, the assumption is reasonable.
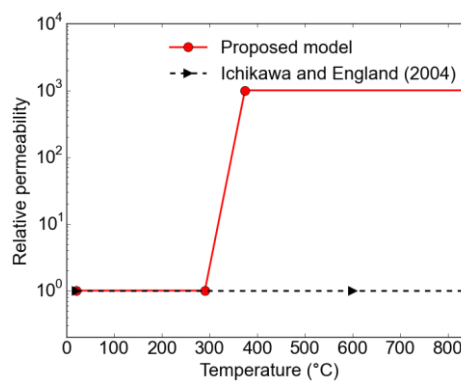
Fig. 7.4 Normalized permeability model

7.2.7 Water-release pattern

There are three forms of water in concrete matrix, i.e. free water, gel water and chemically-bound water. Gel water and chemically-bound water are released gradually into concrete pores at elevated temperature as illustrated in Fig. 7.5. The release of gel water follows the pattern specified by Ichikawa (2000). The release pattern of chemically-bound water is shown in Fig. 7.6, with different water-release patterns proposed by different researchers (Hilsdorf 1967, Bazant and Kaplan 1996, Ichikawa 2000) and experimental data (Tan and Ng 2006). It can be seen that the proposed water release pattern matches well with the experimental data.
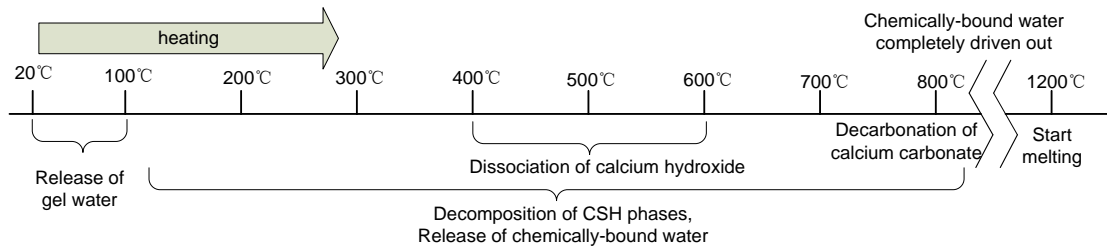
Fig. 7.5 Illustration of water-release of concrete at elevated temperature
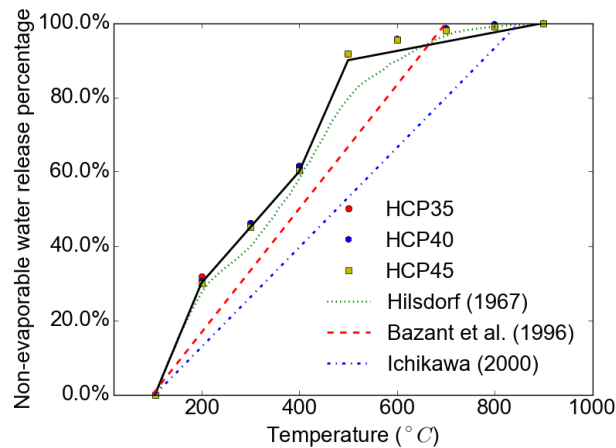
Fig. 7.6 Chemically-bound water release pattern of concrete at elevated temperature

7.2.8 Pressure and dynamic viscosity

Pore pressure in the wet zone and saturated zone is calculated using the equation developed by Saul and Wagner (1987), while that in the dry zone follows the

equation by Saul and Wagner (1989). The dynamic viscosity of water is calculated using the equation developed by Sengers (1986).

7.2.9 Spalling criterion

Thermo-hygral spalling of concrete under fire is deemed to occur when the pore pressure-induced tensile stress exceeds corresponding high-temperature tensile strength. The pore pressure-induced tensile stress is determined using the following equation (Ichikawa and England 2004)

$$\sigma_t = \beta_t p \tag{7.15}$$

where β_t is the scaling factor, taken as 1 in this model (Zeiml et al. 2006).

In this study, tensile strength of concrete is a function of temperature, and temperature-dependent tensile strength reduction factor in Eurocode 2 (2004) is adopted into the model.

7.2.10 Flowchart

A simplified flowchart of the spalling model is shown in Fig. 7.7. Firstly, the concrete section is represented by a finite number of nodes as shown in Fig. 7.2 and time domain is discretized into a finite number of time steps. Given the fire curve and thermal properties of concrete, the temperature profiles of concrete section at different time steps can be determined following Eqn. (7.1). Subsequently, moisture transfer analysis is conducted. Based on the input of concrete mix design parameters, concrete density, environmental RH and curing time of concrete, the initial distribution of moisture is determined. Given the temperature profile across the section, the amount of released gel water and chemically-bound water can be determined according to Section 7.2.7. Given the initial pore pressure in Section 7.2.4, the moisture content is updated using Eqn. (7.2). The pore pressure is updated

following Section 7.2.3. The above steps are repeated for subsequent time steps until the end of heating. After obtaining the pore pressure profiles of concrete section at different time steps, tensile stress generated by pore pressure is compared with temperature-dependent tensile strength of concrete. For a given time step, if the tensile stress at a certain location exceeds the tensile strength of concrete at that temperature, explosive spalling is assumed to occur. If throughout heating, the calculated tensile stress is always below the tensile strength, then there is no spalling.
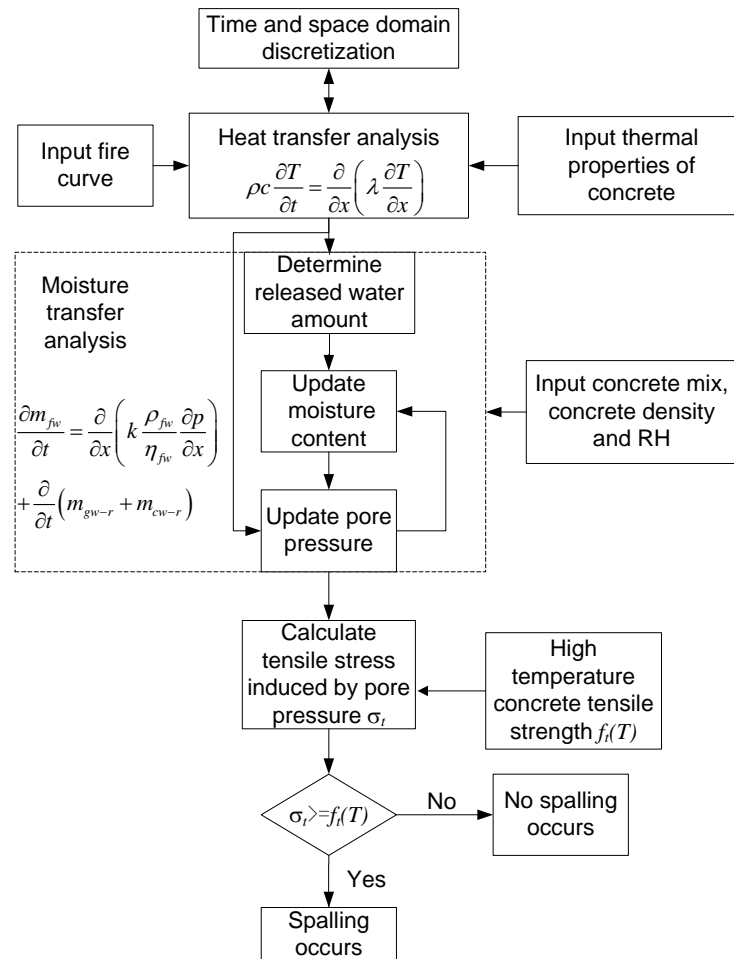
Fig. 7.7 Simplified flowchart of spalling model

7.3 Validation

7.3.1 Moisture migration inside NSC

Van der Heijden et al. (2012) developed a nuclear magnetic resonance (NMR) set-up to measure the moisture transport in heated NSC. The schematic diagram of the NMR set-up is shown in Fig. 7.8. One concrete cylinder specimen (Ø80×100 mm) was prepared for the study. The specimen was pressed in a PTFE holder so that moisture transport was one-dimensional. Heat flow was also confined to one dimension by insulating the specimen using mineral wool. One face of the cylindrical sample was heated with a radiative heat flux of approximately 12 kW m^{-2}. The moisture profiles of the sample were recorded at every 8.5 min.
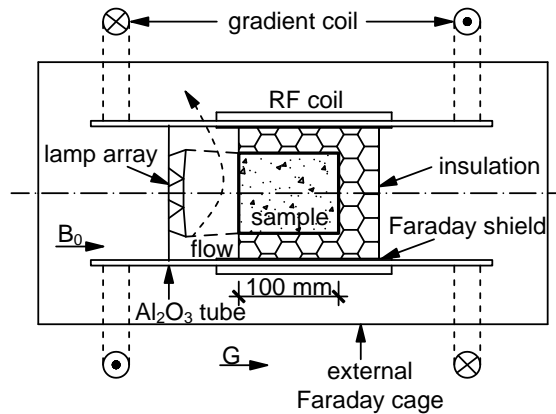
Fig. 7.8 Schematic diagram of the NMR set-up (after Van der Heijden et al. (2012))

The mix proportion of the concrete used in the experiment is given in Table 7.1. Based on the formulation in Appendix I, the volumetric proportions of different components of hydrated concrete are shown in Fig. 7.9.

Table 7.1 Mix proportion of NSC (Van der Heijden et al. 2012)*

CEM I 32.5 R	1
Sand (0.125 – 0.250)	0.363
Sand (0.250 – 0.500)	0.62
Sand (0.500 – 1)	0.62
Sand (1 – 2)	0.723
Sand (2 – 4)	1.086
gravel (4 – 8mm)	1.754
water	0.5
Water/cement ratio (w/c)	0.5
Aggregate/cement ratio (a/c)	5.166

* Ingredients are expressed as respective weight proportion of cement content.
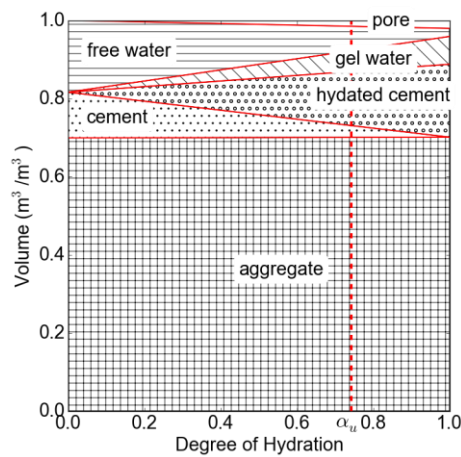
Fig. 7.9 Volumetric proportions of components of the NSC given in Table 7.1

The model parameters are summarized in Table 7.2. Based on the concrete age at testing and environmental RH, moisture distribution along the cylinder height is determined (Fig. 7.10), which serves as the initial condition of moisture transfer analysis.

The permeability of concrete is not provided in literature, so it is estimated based on experience. The principle is that permeability of high performance concrete should be lower than the permeability of normal strength concrete and permeability of concrete should be within the measured permeability range in literature. The same applies to the rest four cases.

Table 7.2 Model parameters for numerical analysis

Time interval	1 s	Thermal conductivity	$2 \ \mathrm{Wm^{-1}K^{-1}}$
No. of Nodes	25	Specific heat	$900 \ \mathrm{Jkg^{-1}K^{-1}}$
Initial Permeability	$8.0\mathrm{E}\text{-}18\mathrm{m}^2$	h_f	$0 \ \mathrm{Wm^{-2}K^{-1}}$
Concrete density	$2460 \ \mathrm{kg/m^3}$	h_e	$0 \ \mathrm{Wm^{-2}K^{-1}}$
Concrete age at testing	365 days	ε_0	0.7
Environmental RH	97%	ε_L	0.3
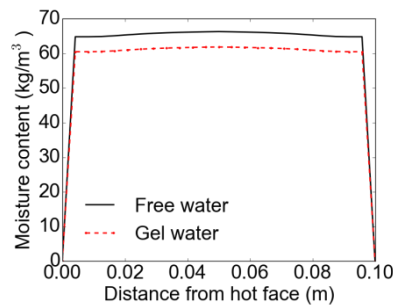
Fig. 7.10 Moisture distribution along the height of the NSC cylinder

Fig. 7.11(a)-(i) compares predicted and measured moisture profiles in the concrete cylinder at different heating times (8.5 min to 76.5 min at an interval of 8.5 min). The predicted results capture important features of moisture migration in the concrete specimen. Moisture in the hot region migrates deep into the cold region because of pressure-induced flow. As a result, the moisture content in the hot region decreases gradually as seen from Fig. 7.11(a) to Fig. 7.11(b). When the moisture content becomes very small, a dry zone forms (Fig. 7.11(b)). The dry zone increases from 17min to 76.5 min as heating continues (from Fig. 7.11(b) to Fig. 7.11(i)). In the inner section of the specimen, a saturated zone forms as seen in Fig. 7.11(b)-(i). The formation of saturated zone is known as a 'moisture clogging' phenomenon (Harmathy 1965) where the concrete pores are filled with water. The saturated zone moves towards the unexposed face as heating continues (from Fig. 7.11(b) to Fig. 7.11(i)). The predicted results are in good agreement with the measured results.

(a) 8.5 min   (b) 17 min   (c) 25.5 min

(d) 34 min   (e) 42.5 min   (f) 51 min

(g) 59.5 min   (h) 68 min   (i) 76.5 min
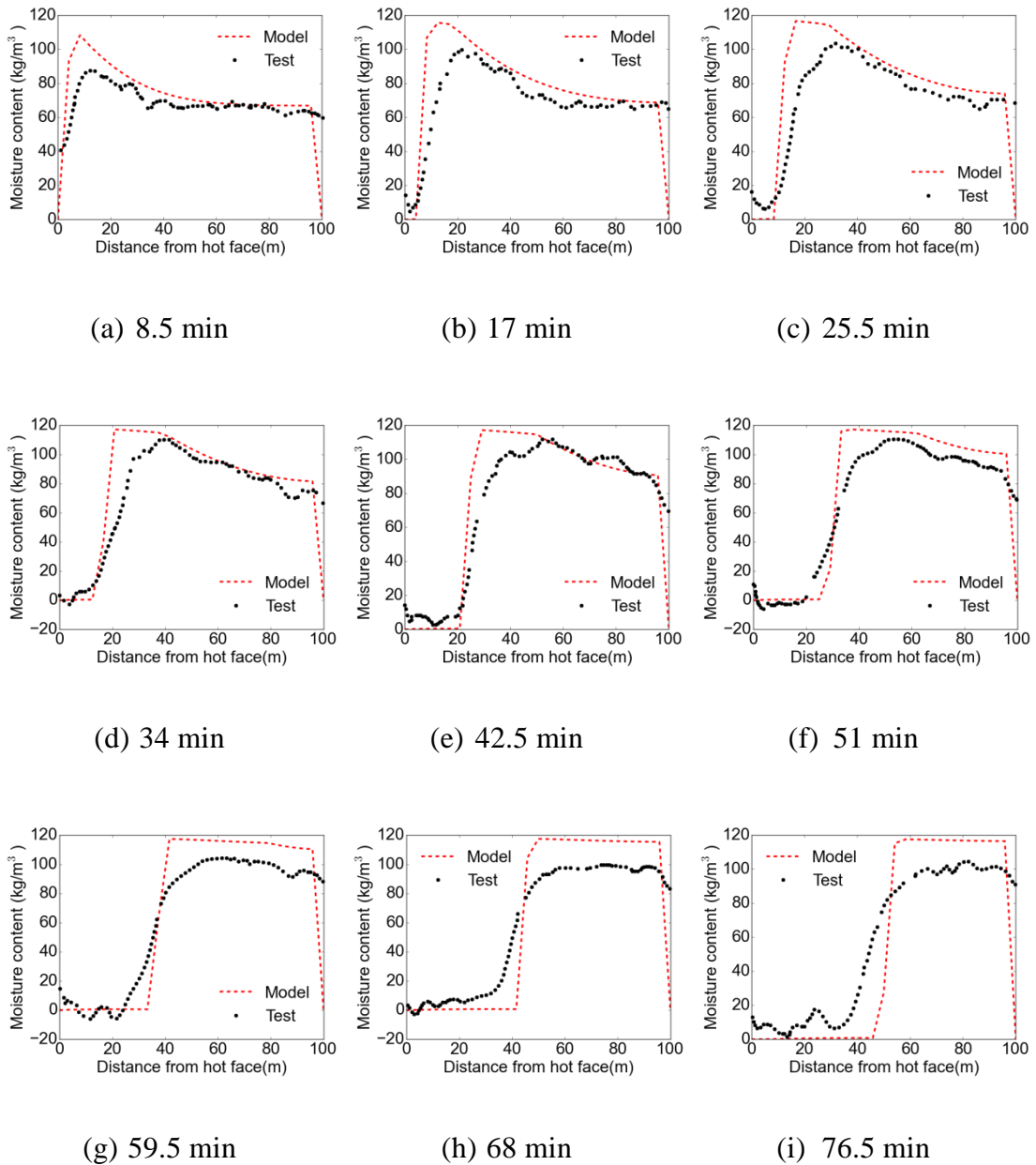
Fig. 7.11 Moisture profiles of the concrete cylinder at different time

7.3.2 Pressure buildup inside NSC

Kalifa et al. (2000) conducted a test to measure pore pressure development inside a NSC slab at high temperature. The experimental set-up is shown in Fig. 7.12. As shown in the figure, the NSC slab was subjected to 600 ℃ on one face and to 20 ℃ on the opposite face. The four lateral faces of the slab were insulated with ceramic

blocks. Five locations (10, 20, 30, 40, and 50 mm from heated face) were installed with pore pressure gages to record pore pressure time history during heating.
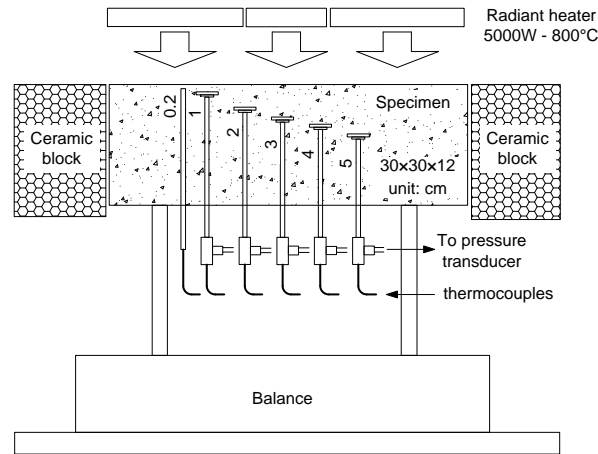
Fig. 7.12 The experimental set-up (after Kalifa et al. (2000))

The mix proportion of the concrete used in the experiment is given in Table 7.3. Based on the formulation in Appendix I, the volumetric proportions of different components of hydrated concrete are shown in Fig. 7.13.

Table 7.3 Mix proportion of NSC (Kalifa et al. 2000)*

Cement CPJ-CEM II 32.5	1
Silico-calcareous sand (Seine 0/4 mm)	1.146
Calcareous sand (Boulonnais 0/5 mm)	1.146
Calcareous aggregates (Boulonnais 5/12.5 mm)	1.469
Calcareous aggregates (Boulonnais 12.5/20 mm)	1.469
Water	0.5
Water/cement ratio (w/c)	0.5
Aggregate/cement ratio (a/c)	5.23

* Ingredients are expressed as weight proportion of cement content.
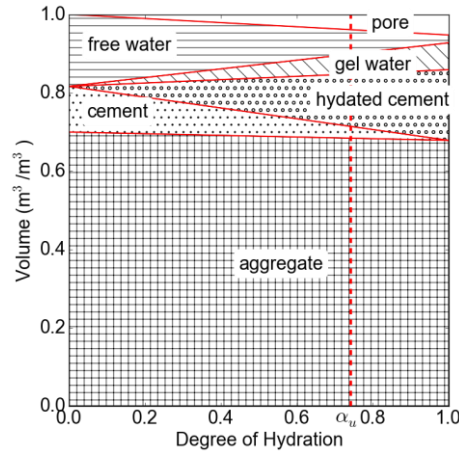
Fig. 7.13 Volumetric proportions of components of the NSC given in Table 7.3

The model input parameters are summarized in Table 7.4. Moisture distribution inside the NSC slab is shown in Fig. 7.14.

Table 7.4 Model parameters for numerical analysis

Time interval	1 s	Thermal conductivity	2 $Wm^{-1}K^{-1}$
No. of Nodes	26	Specific heat	900 $Jkg^{-1}K^{-1}$
Initial Permeability	4.0E-18 m^2	h_f	25 $Wm^{-2}K^{-1}$
Concrete density	2400 kg/m^3	h_e	25 $Wm^{-2}K^{-1}$
Concrete age at testing	180 days	ε_0	0.25
Environmental RH	80%	ε_L	0.39
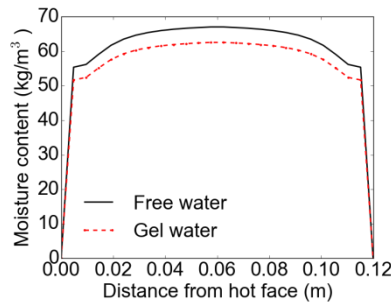
Fig. 7.14 Moisture distribution along the NSC slab depth

Fig. 7.15(a)-(e) compares predicted and measured pore pressure histories at 10, 20, 30, 40, and 50 mm away from the heated face of the NSC slab. Both the predicted and measured pore pressures increase to a peak value at first, and then decrease gradually to a negligible value. In the pre-peak stage, the predicted curves match

well with measured curves at the five locations. At 10, 20, and 30mm, the predicted peak pore pressures are slightly lower than the measured results as shown in Fig. 7.15(a)-(c). At 40 and 50 mm, the predicted peak pore pressures are slightly higher than the test results as shown in Fig. 7.15(d)-(e). The time corresponding to predicted peak pore pressures matches well with that corresponding to measured peak pore pressures at the five locations. In the post-peak stage, the predicted peak pore pressures at 10, 20, 30, and 40 mm are greater than the measured counterparts in the beginning, and became lower than the measured counterparts later; the predicted peak pore pressure at 50 mm were greater than the measured pore pressure all the way. This difference is due to deviations between the actual hot permeability of concrete and the assumed permeability of concrete in the spalling model. The agreement between predicted and measured results is reasonably good.

(a) 10 mm   (b) 20 mm   (c) 30 mm

(d) 40 mm   (e) 50 mm

Fig. 7.15 Measured and predicted pore pressure histories at different depths of the NSC slab from fire-exposed face

7.3.3 Pressure buildup inside HPC

● Reactor containment under accident condition

Shekarchi et al. (2003) conducted a test to study the thermo-hygral behavior of HPC inner wall of a nuclear power station under a severe accident condition. A sketch of the experimental apparatus is shown in Fig. 7.16. A cylindrical specimen with a thickness of 1.3 m (the same as in the nuclear containment) was used. The specimen was vertically put into place, laterally sealed by resin and wrapped with thermal insulation to ensure 1D moisture migration and heat transfer. One face of the cylindrical specimen was subjected to severe accident condition. The accident condition consisted of a linear temperature rise from 20 °C to 200 °C, and a steam pressure increasing to 13 bars in 24 h. Then the temperature and steam pressure were maintained for another 24 h before cooling down.
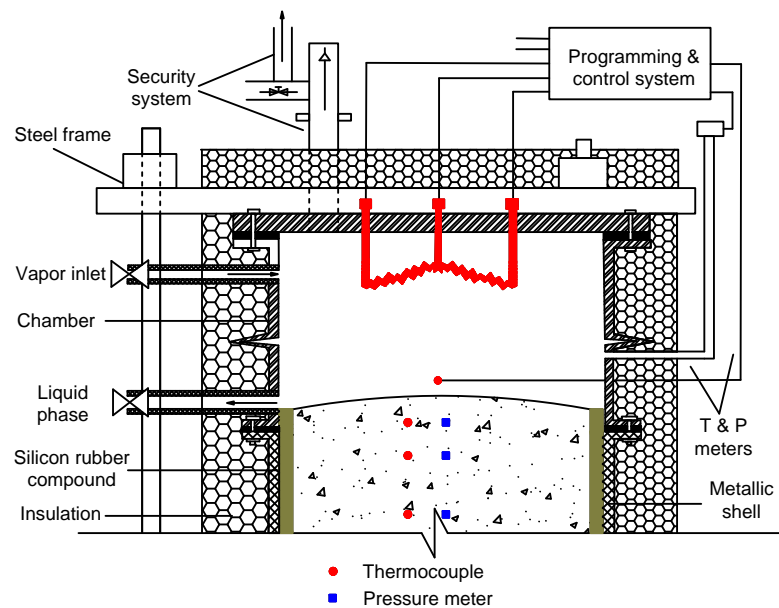
Fig. 7.16 Sketch of experimental apparatus (after Shekarchi et al. (2003))

The mix proportion of the HPC used in the experiment is given in Table 7.5. Based on the formulation in Appendix I, the volumetric proportions of different components of hydrated concrete are shown in Fig. 7.17.

Table 7.5 Mix proportion of HPC (Shekarchi et al. (2003))*

CEM II 42.5 cement	1
Calcareous sand 0/5	2.940
Fine gravel 5/12.5	1.195
Gravel 12.5/25	3.064
Calcareous fillers	0.214
Silica fume	0.152
water	0.605
Superplasticizer	0.034
Retarding admixture	0.004
Water/cement ratio (w/c)	0.605
Aggregate/cement ratio (a/c)	7.41
Silica fume/cement ratio (s/c)	0.152

* Ingredients are expressed as weight proportion of cement content.
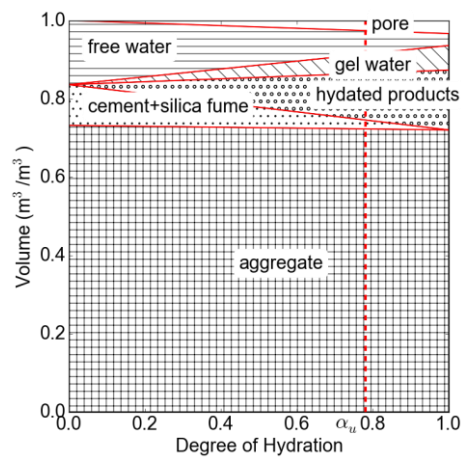
Fig. 7.17 Volumetric proportions of components of the HPC given in Table 7.5

In order to simulate Shekarchi et al.'s experiment (Shekarchi et al. 2003), the cylindrical specimen is represented by a 1D model of length L = 1.3 m. The pressure at the hot face follows the saturated vapor pressure curve. The model parameters are summarized in Table 7.6. Moisture distribution inside the HPC slab is shown in Fig. 7.18.

Table 7.6 Model parameters for numerical analysis

Time interval	60 s	Thermal conductivity	2.3 Wm^{-1}K^{-1}
No. of Nodes	35	Specific heat	900 Jkg^{-1}K^{-1}
Initial Permeability	1.0E-18 m^2	h_f	60 Wm^{-2}K^{-1}
Concrete density	2450 kg/m^3	h_e	0 Wm^{-2}K^{-1}
Concrete age at testing	200 days	ε_0	0.9
Environmental RH	80%	ε_L	0.0
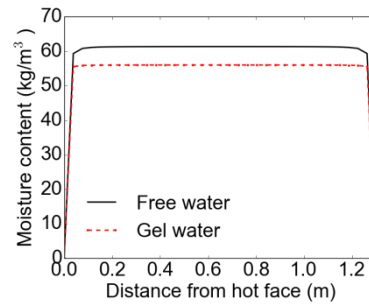
Fig. 7.18 Moisture distribution along the height of the cylindrical specimen

Fig. 7.19 compares measured and predicted pressure distributions in the cylindrical specimen at 24 h and 48 h. The pressure at the fire-exposed face is the greatest and decreases with increasing distance x from the fire-exposed face. At the far end, the pressure is negligible. The predicted results reasonably simulate the test results.
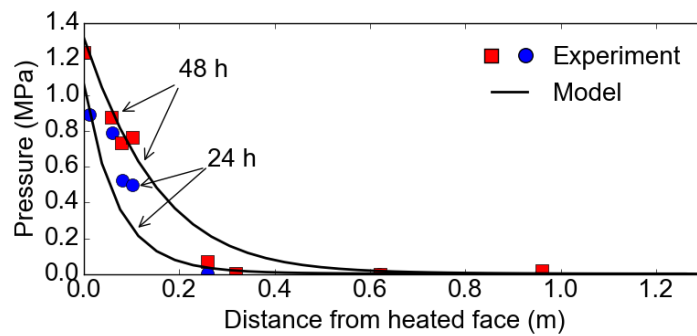
Fig. 7.19 Measured and predicted pressure profiles at 24 h and 48 h

- Concrete slab under high temperature

Kalifa et al. (2001) measured pore pressure development inside HPC at high temperature. Two 120-mm thick HPC slabs were prepared for pore pressure measurements. The same experimental set-up (Fig. 7.12) as described in Section 7.3.2 was adopted. The pore pressure was measured at five locations (10, 20, 30, 40, and 50 mm from heated face).

The mix proportion of the concrete used in the experiment is given in Table 7.7. Based on the formulation in Appendix I, the volumetric proportions of different components of hydrated concrete are shown in Fig. 7.20.

Table 7.7 Mix proportion of HPC (Kalifa et al. 2001)*

Cement CPA CEM I 52.5 PM CP	1
Silico-calcareous sand (Seine 0/4 mm)	1.058
Calcareous sand (Boulonnais 0/5 mm)	1.041
Calcareous aggregates (Boulonnais 5/12.5 mm)	1.176
Calcareous aggregates (Boulonnais 12.5/20 mm)	1.352
Condensed silica fume	0.1
water	0.3
Superplasticizer Chryso GT	0.033
Water/cement ratio (w/c)	0.3
Aggregate/cement ratio (a/c)	5.23
Silica fume/cement ratio (s/c)	0.1

* Ingredients are expressed as weight proportion of cement content.
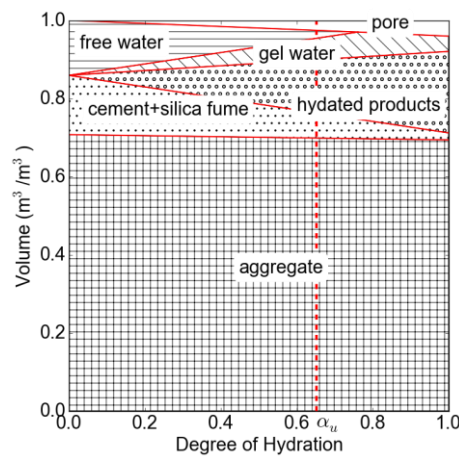
Fig. 7.20 Volumetric proportions of components of the HPC given in Table 7.7

The model parameters are summarized in Table 7.8. Moisture distribution inside the HPC slab is shown in Fig. 7.21.

Table 7.8 Model parameters for numerical analysis

Time interval	1 s	Thermal conductivity	2.3 $Wm^{-1}K^{-1}$
No. of Nodes	26	Specific heat	1000 $Jkg^{-1}K^{-1}$
Initial Permeability	6.0E-19 m^2	h_f	25 $Wm^{-2}K^{-1}$
Concrete density	2500 kg/m^3	h_e	25 $Wm^{-2}K^{-1}$
Concrete age at testing	90 days	ε_0	0.25
Environmental RH	80%	ε_L	0.3
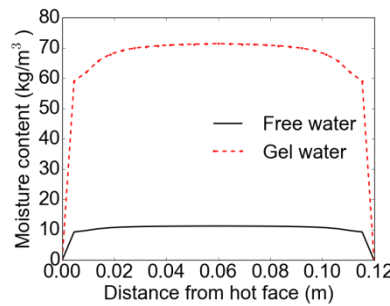
Fig. 7.21 Moisture distribution along the HPC slab depth

Fig. 7.22(a)-(e) compares predicted and measured pore pressure histories at 10, 20, 30, 40 and 50 mm away from the heated face of the HPC slab. Both the predicted and measured pore pressures increase at first at the five locations. When the peak values are reached, both predicted and measured pore pressures decrease with time. The predicted peak pore pressures match well with the measured peak pore pressures at 20, 30, and 40 mm as shown in Fig. 7.22(b)-(d). At 50 mm, the measured peak pore pressure is much lower than the prediction as shown in Fig. 7.22(e) possibly due to occurrence of micro-cracks around the pressure gage. The predicted time corresponding to peak pore pressure is also in good agreement with the actual time for peak pressure except for that at 50 mm. With increasing distance from the fire-exposed face, the time corresponding to peak pore pressure increases as can be seen from Fig. 7.22(a) to Fig. 7.22(d). The numerical model in general

captures well the phenomenon of pore pressure development inside the HPC slabs under heating.

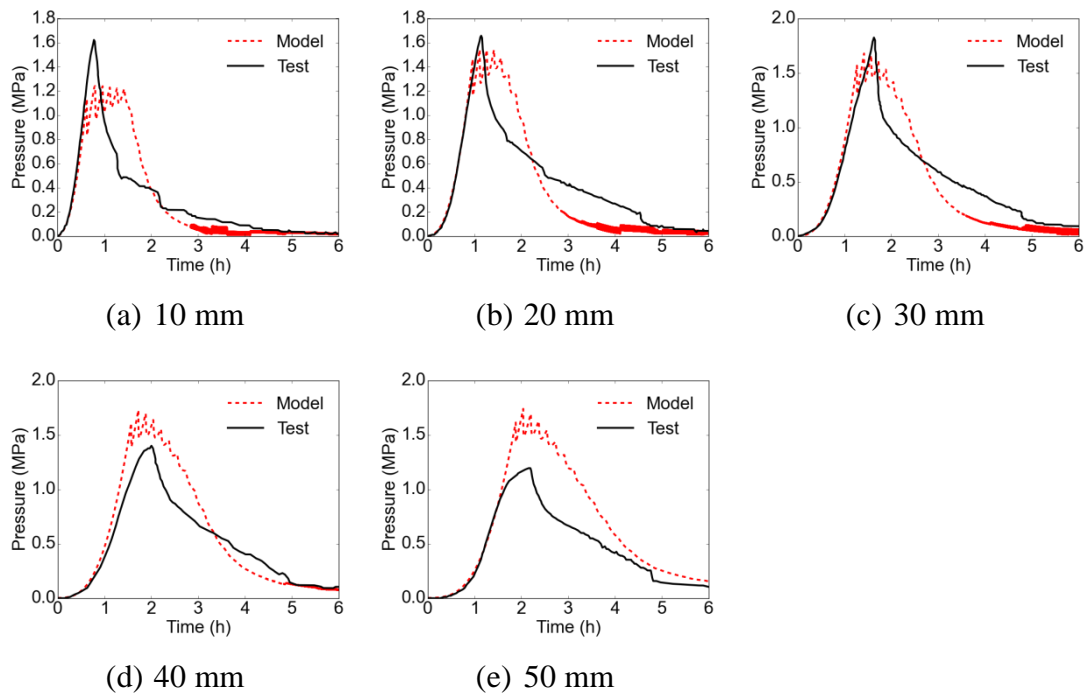(a) 10 mm   (b) 20 mm   (c) 30 mm

(d) 40 mm   (e) 50 mm
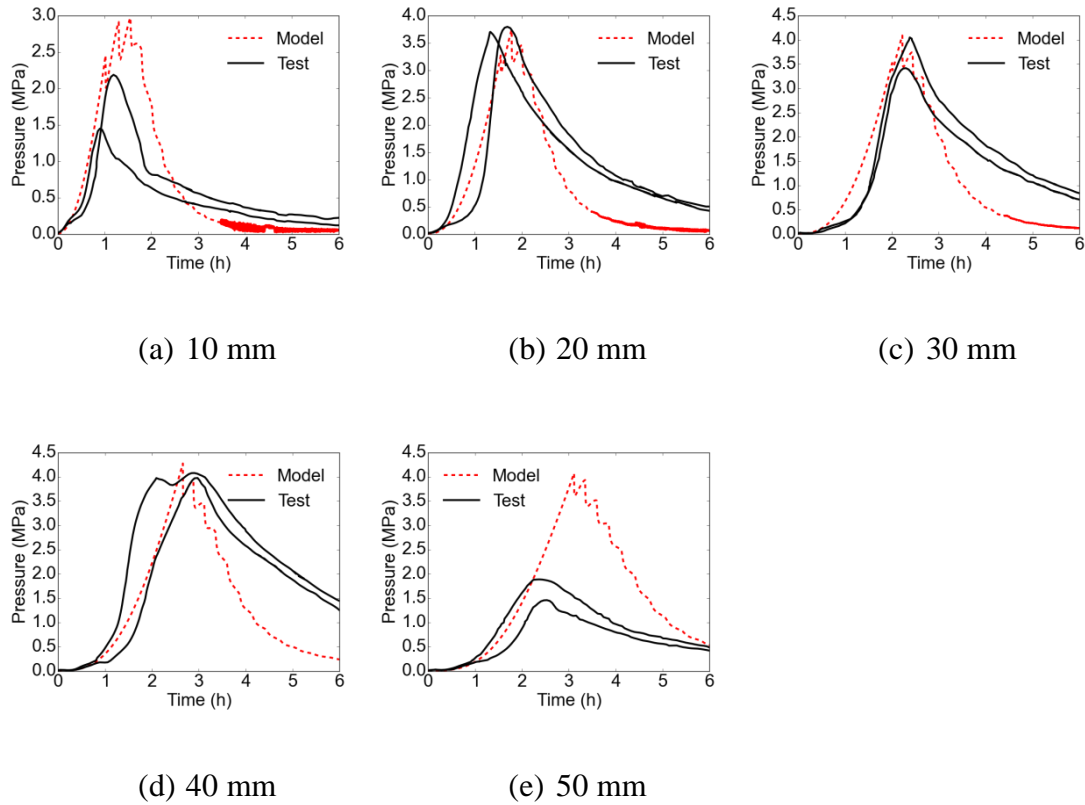
Fig. 7.22 Measured and predicted pore pressure histories at different depths of the HPC slab from fire-exposed face

7.3.4 Prediction of concrete spalling

Ozawa et al. (2012) used acoustic emission method to detect the time of explosive spalling of concrete. The heating test set-up is shown in Fig. 7.23. A concrete panel with a thickness of 100 mm was subject to heating at the bottom face. The gas temperature at the heat-exposed face was increased at a rate of 20 ℃/min. A pressure gage was embedded in the panel at a depth of 8 mm from the heated face to measure internal pore pressure.
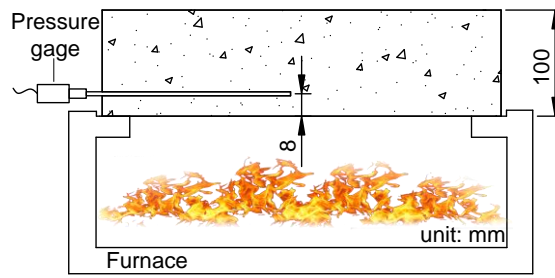
Fig. 7.23 Heating test set-up (after Ozawa et al. (2012))

The mix proportion of the concrete used in the experiment is given in Table 7.9. Based on the formulation in Appendix I, the volumetric proportions of different components of hydrated concrete are shown in Fig. 7.24.

Table 7.9 Mix proportion of concrete (Ozawa et al. 2012)*

Cement	1
Fine aggregate	1.909
Coarse aggregate	2.409
Water	0.3
Admixture	0.05
Water/cement ratio (w/c)	0.3
Aggregate/cement ratio (a/c)	4.32
Compressive strength (MPa)	83.5

* Ingredients are expressed as weight proportion of cement content.
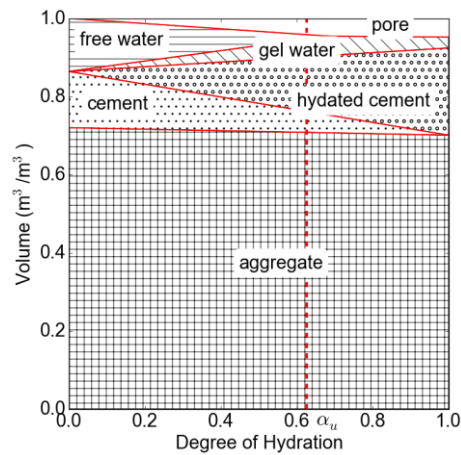
Fig. 7.24 Volumetric proportions of components of the concrete given in Table 7.9

The model input parameters are summarized in Table 7.10. The tensile strength of concrete is estimated to be 1/15 of its compressive strength. Moisture distribution inside the concrete panel is determined as shown in Fig. 7.25.

Table 7.10 Model parameters for numerical analysis

|			
Time interval	1 s	Thermal conductivity	2.2 $Wm^{-1}K^{-1}$
No. of Nodes	25	Specific heat	1000 $Jkg^{-1}K^{-1}$
Initial Permeability	1.0E-18 m^2	h_f	25 $Wm^{-2}K^{-1}$
Concrete density	2480 kg/m^3	h_e	25 $Wm^{-2}K^{-1}$
Concrete drying time	118 days	ε_0	0.25
Environmental RH	40%	ε_L	0.3
Tensile strength	5.6 MPa		
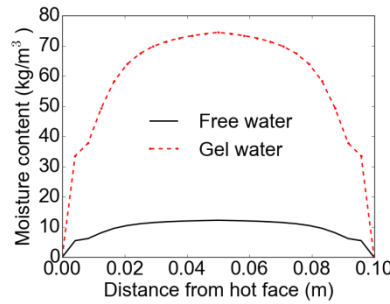
Fig. 7.25 Moisture distribution along the concrete panel depth

Fig. 7.26 gives the predicted concrete panel thickness as a function of heating time. The predicted spalling time and spalling depth of concrete panel are about 41 min and 8.4 mm, respectively. The predicted pore pressure-induced tensile stress across the panel depth at the spalling time is plotted together with instantaneous tensile strength profile of concrete in Fig. 7.27. In the heating test, explosive spalling of concrete occurred at about 43 min. The spalling depths of the concrete panel were uneven across the heated face. The minimum spalling depth was 0 mm and the maximum 12 mm. Fig. 7.28 shows the measured and predicted pore pressure histories at a depth of 8 mm from the heated face. Both the measured and predicted pore pressures increase slowly in the first 35 min, and after that, they increased rapidly to the maximum. At the time of explosive spalling, the measured and the

predicted pore pressures began to decrease. The prediction of spalling in general agrees well with the test results.
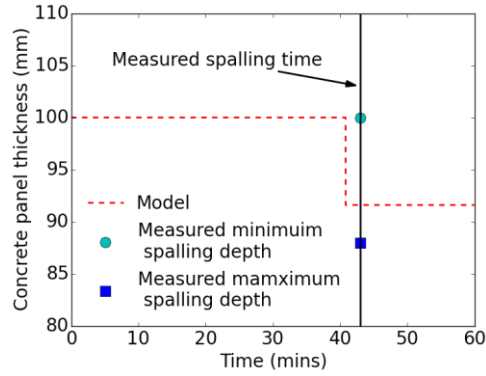
Fig. 7.26 Comparison of predicted and measured spalling time and depth
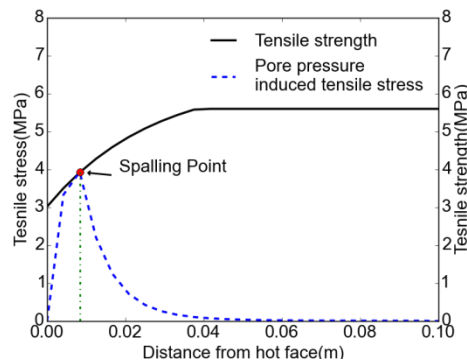
Fig. 7.27 Pressure-induced tensile stress across the concrete panel thickness at spalling time
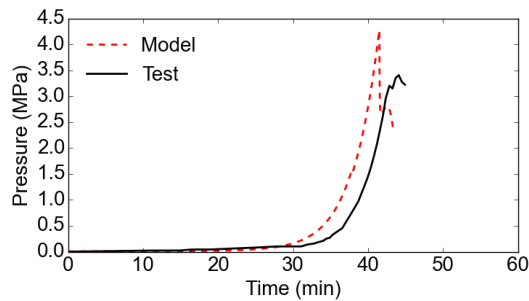
Fig. 7.28 Measured and predicted pore pressure histories at a depth of 8 mm from heated face

7.4 Summary

A simple one-dimensional thermo-hygral spalling model is proposed in this study. The predictions of the spalling model are compared with five different sets of experiment data. The predictions are in relatively satisfactory agreement with the measured results.

The proposed spalling model predicts realistically the movement of moisture inside the heated concrete. Both the model and experiment show that moisture migrates gradually from hot region to cold region as heating continues. The phenomenon of 'moisture clog' is also captured by the model.

The developed spalling model predicts reasonably well the pore pressure buildup in concrete. For rapid uniform heating of one face of a concrete slab, both predicted and measured pore pressure initially increase to the peak value and then diminish gradually. The HPC is predicted to have a higher peak pore pressure than NSC due to lower permeability, which is in agreement with widely-accepted opinion that HPC is more susceptible to explosive spalling than NSC.

The spalling model is also capable of predicting thermo-hygral spalling of concrete under fire, i.e., when and where explosive spalling would occur. This capability can be incorporated into fire resistance analysis of concrete members to get more realistic modeling.

The spalling model provides a cost-effective and time-saving method to assess thermo-hygral spalling risk of concrete under fire. It can also be used to tailor thermo-hygral-spalling-free concrete mix in the preliminary concrete mix design. Future work can be done to take account of the effect of fibers in the spalling model. The effect of polymer fibers can be incorporated in the spalling model by

considering the effect of fibers on porosity and hot permeability of concrete. The effect of steel fibers can be incorporated in the spalling model by considering the contribution of steel fibers to tensile strength of concrete.

However, current model is only applicable for prediction of the first-time thermo-hygral spalling. Thermo-hygral spalling of concrete sometimes occurs in a progressive manner. There is a need to develop a model capable of predicting progressive spalling of concrete under fire. The ultimate goal is to develop a spalling model that takes all three types of spalling and their interactions into account.

CHAPTER 8. CONCLUSIONS, CONTRIBUTIONS, AND CHALLENGES

8.1 Conclusions and Contributions

The research presented in this thesis centers on two topics, i.e. fire resistance of DFRCC and fire-induced spalling of concrete materials.

To improve fire performance of DFRCC, an experimental program was designed to optimize multiple responses of fire-damaged DFRCC. Then residual mechanical properties and explosive spalling resistance of the optimized DFRCC mix were examined. Hot permeability and residual porosity were also measured to discover the role of PVA fibers in combating explosive spalling.

To better understand fire-induced concrete spalling and predict occurrence of spalling, the priority is to identify the driving force underlying this phenomenon. This thesis presents a critical review of conflicting and concordant points on concrete spalling at elevated temperature and proposes a unified and coherent fire-induced concrete spalling theory. A 1D spalling model was also developed to predict occurrence of explosive spalling.

The major contributions of the research in this thesis are summarized as follows:

- This work improved mechanical performance of fire-damaged DFRCC.

- The thesis examined explosive spalling resistance of DFRCC, measured hot permeability of DFRCC and discussed the role of PVA fibers in combating explosive spalling.

- The thesis advanced a unified fire-induced concrete spalling theory, which explains the contradictory issues in previous spalling theories and provides

theoretical basis for modeling spalling and establishing guidelines to prevent spalling.

● Current codes of practice only recommend protective measures against explosive spalling. Countermeasures against three types of fire-induced concrete spalling are proposed in this thesis. The concept of "multiple defense line against fire-induced concrete spalling" can be adopted in next-generation fire safety codes of concrete for the highest level of protection.

● The work developed a 1D spalling model which provides an economic tool to assess explosive spalling risk of concrete and can be used to develop concrete materials which are free from explosive spalling.

The major conclusions of the research on fire resistance of DFRCC in this thesis are summarized as follows:

● The Taguchi approach using utility concept is an effective method to optimize multiple responses of DFRCC, i.e. tensile strain capacity, compressive strength, and residual compressive strength after subjecting to 200 ℃, 400 ℃, 600 ℃, 800 ℃ of heating.

● With 2% vol. PVA fibers, DFRCC shows the best tensile ductility. However, post-fire performance of this DFRCC mix is not the most favorable. Replacement of 0.5% vol. PVA fibers with steel fibers improves residual compressive strength of DFRCC. It also helps resist tensile brittle failure of DFRCC after exposure to 300 ℃.

● The DFRCC optimized in this thesis outperformed normal concrete in terms of residual compressive strength and elastic modulus after fire. The residual compressive strength of DFRCC showed an increase after 200 ℃ of heating. Above 200 ℃, the residual compressive strength reduced with an increase in temperature. Even so, the compressive strength of DFRCC after 800 ℃ of

heating can retain about 35% of its original strength. The elastic modulus of DFRCC decreased as temperature increased. The decreasing trend was aggravated after exposure to 600 ℃ and above. After 800 ℃, only 13.2% of elastic modulus of unheated DFRCC was retained.

● The addition of hybrid PVA and steel fibers is effective in resisting thermo-hygral spalling. The DFRCC specimen showed good spalling resistance under fire. In contrast, the mortar specimen suffered progressive spalling, ending in complete failure even without any mechanical load.

● The initial porosity and permeability of DFRCC is larger than those of mortar. A small increase in porosity can lead to a large increase in permeability. Therefore, in addition to total porosity, pore size distribution also plays an important role in determining permeability of DFRCC.

● The permeability values of DFRCC and mortar remain almost unvaried at 105 ℃ compared to at ambient temperature. However, the permeability of DFRCC increases fast beyond 105 ℃, especially between 150 ℃ and 200 ℃. In contrast, the permeability of mortar at 200 ℃ is still of the same order of magnitude as the permeability of mortar at room temperature.

● There is little difference in porosity increases for DFRCC and mortar after exposure to 300 ℃. Melted products of PVA fibers are attached on fiber channel walls and cannot diffuse into the matrix. The permeability of DFRCC increases fast from 150 ℃ to 200 ℃, before PVA fibers melt.

● No microcracks initiated around the perimeter of PVA fibers up to 300 ℃. Increased ITZs around PVA fibers and voids formed at ends of the fibers contribute to permeability increase in DFRCC, consequently spalling-free performance.

The major conclusions of the research on fire-induced concrete spalling in this thesis are summarized as follows:

● There are three types of fire-induced concrete spalling depending on the mechanisms, viz., thermo-hygral, thermo-mechanical and thermo-chemical spalling.

● Thermo-hygral spalling is induced by moisture clogging and pore pressure buildup inside heated concrete. It typically occurs within 220 ℃ and 320 ℃.

● Thermo-mechanical spalling is caused by applied stress and restraint-induced thermal stress in heated concrete. It typically occurs within 430 ℃ and 660 ℃.

● Thermo-chemical spalling is related to decomposition of hydrated products and calcite, and rehydration of calcium oxide. It typically occurs at or after temperature greater than 750 ℃.

● The proposed 1D thermo-hygral spalling model in this thesis predicts realistically the movement of moisture and pore pressure buildup in the heated concrete. The spalling model is capable of predicting the first thermo-hygral spalling of concrete under fire, i.e., when and where the first thermo-hygral spalling would occur.

8.2 Challenges

Based on the work in this thesis, the following problems are recommended for future research:

● Currently, a majority of works focus on post-fire mechanical properties of DFRCC. Post-fire mechanical properties are necessary for post-fire assessment and restoration. Hot mechanical properties determine how long

structural members can sustain under fire. There is a need to investigate hot mechanical properties of DFRCC.

● The author has developed one type of high-temperature resistive DFRCC, the compressive strength of which is about 50MPa. It maintains its tensile ductility at 200 ℃ and exhibits tensile strain-softening behavior up to 600 ℃ as shown in Fig. 8.1. However, developing high-temperature resistive DFRCC that can maintain strain-hardening behavior at a higher temperature remains a challenge.

(a) 30 ℃   (b) 200 ℃   (c) 600 ℃
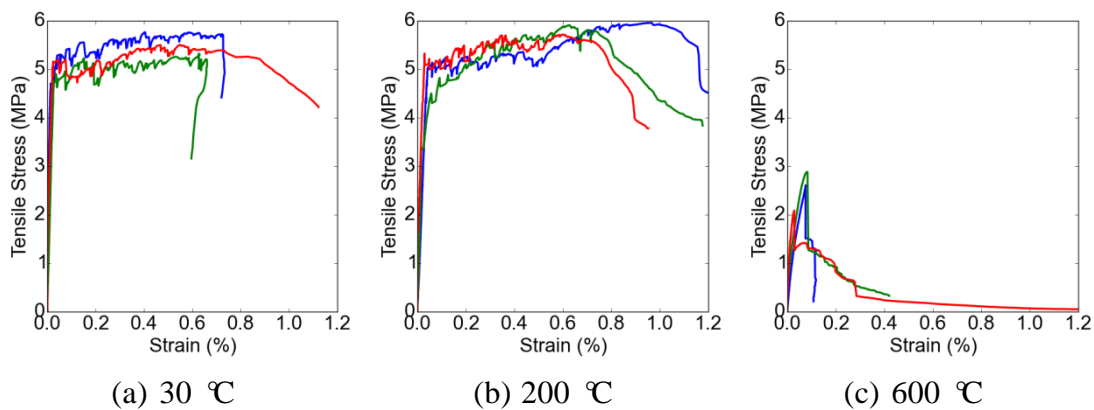
Fig. 8.1 Tensile behavior of high-temperature resistive DFRCC at 30 ℃ and after exposure to 200 ℃ and 600 ℃

● A series of micromechanical tests, such as single fiber pull out tests and fracture toughness tests etc., need to be done for developing high-temperature micromechanics model to predict tensile behavior of fire-damaged DFRCC.

● There is a lack of data on thermal properties of DFRCC including thermal conductivity, specific heat, thermal expansion coefficient at elevated temperature. Thermal property models of DFRCC are necessary inputs in performance-based fire safety design of structures made fully or partially of DFRCC.

● Current research work studies fire resistance of DFRCC at material scale. This forms the basis for studying fire resistance of DFRCC at structural scale.

It is necessary to study structural fire resistance of DFRCC members or members strengthened by DFRCC

● There is interaction among these three types of spalling. There is a lack of research work on spalling behavior of stressed or restrained concrete specimens, especially on full-scale structural members. Test results on stressed or restrained concrete is more useful for designing structural concrete against thermal spalling.

● There is a lack of research work on post-cooling spalling, though it is a potential threat to post-fire performance of concrete structures. There is a need to make an intensive study of post-cooling spalling.

● The proposed spalling model in this thesis is a deterministic model. There is a need to extend the deterministic model to a stochastic model by taking into account uncertainties of parameters in the model.

● The spalling model developed in this thesis is only applicable for prediction of the first-time thermo-hygral spalling of concrete. But thermo-hygral spalling sometimes occurs in a progressive manner, and prediction of thermo-mechanical and thermal-chemical spalling is also not incorporated. Future predictive tools are expected to predict progressive thermo-hygral spalling and all three types of spalling and interactions among them.

REFERENCES

ACI (2007). "216.1 Code requirements for determining fire resistance of concrete and masonry construction assemblies". Farmington Hills (Michigan).

Akturk, B., Yuzer, N. and Kabay, N. (2015). "Usability of Raw Rice Husk Instead of Polypropylene Fibers in High-Strength Concrete under High Temperature." Journal of Materials in Civil Engineering, Vol. 28, No. 1, pp. 04015072.

Ali, F., Nadjai, A., Silcock, G. and Abu-Tair, A. (2004). "Outcomes of a major research on fire resistance of concrete columns." Fire Safety Journal, Vol. 39, No. 6, pp. 433-445.

Annerel, E. and Taerwe, L. (2009). "Revealing the temperature history in concrete after fire exposure by microscopic analysis." Cement and Concrete Research, Vol. 39, No. 12, pp. 1239-1249.

Arioz, O. (2009). "Retained properties of concrete exposed to high temperatures: size effect." Fire and Materials, Vol. 33, No. 5, pp. 211-222.

ASTM (2003). "Standard Specification for Coal Fly Ash and Raw or Calcined Natural Pozzolan for use as a Mineral Admixture in Portland Cement Concrete". 618, Philadelphia, USA.

ASTM (2010). "Standard Practice for Thermal Conductivity of Materials Using a Thermal Capacitance (Slug) Calorimeter". E2584-10. ASTM International, West Conshohocken, PA.

ASTM (2011). "Standard Test Method for Determining Specific Heat Capacity by Differential Scanning Calorimetry". E1269-11. ASTM International, West Conshohocken, PA.

ASTM (2013). "Standard Test Method for Density, Absorption, and Voids in Hardened Concrete". C642. ASTM International.

Atlassi, E. H. (1995). "Nonevaporable water and degree of cement hydration in silica fume-cement systems." ACI Special Publication, Vol. 153, No. pp. 703-718.

Ayan, E., Saatçioğlu, Ö. and Turanli, L. (2011). "Parameter optimization on compressive strength of steel fiber reinforced high strength concrete." Construction and Building Materials, Vol. 25, No. 6, pp. 2837-2844.

Bailey, C. (2002). "Holistic behaviour of concrete buildings in fire." Proceedings of the Institution of Civil Engineers-Structures and Buildings, Vol. 152, No. 3, pp. 199-212.

Bangi, M. R. and Horiguchi, T. (2012). "Effect of fibre type and geometry on maximum pore pressures in fibre-reinforced high strength concrete at elevated temperatures." <u>Cement and Concrete Research</u>, Vol. 42**,** No. 2, pp. 459-466.

Bary, B., Ranc, G., Durand, S. and Carpentier, O. (2008). "A coupled thermo-hydro-mechanical-damage model for concrete subjected to moderate temperatures." <u>International journal of heat and mass transfer</u>, Vol. 51**,** No. 11, pp. 2847-2862.

Bažant, Z. P., Chern, J.-C. and Thonguthai, W. (1982). "Finite element program for moisture and heat transfer in heated concrete." <u>Nuclear Engineering and Design</u>, Vol. 68**,** No. 1, pp. 61-70.

Bazant, Z. P. and Kaplan, M. F. (1996). <u>Concrete at high temperatures: material properties and mathematical models</u>. Longman.

Beneš, M. and Štefan, R. (2015). "Hygro-thermo-mechanical analysis of spalling in concrete walls at high temperatures as a moving boundary problem." <u>International journal of heat and mass transfer</u>, Vol. 85**,** No. pp. 110-134.

Benmarce, A. and Guenfoud, M. (2005). "Experimental behaviour of high-strength concrete columns in fire." <u>Magazine of Concrete Research</u>, Vol. 57**,** No. 5, pp. 283-287.

Bentz, D. P. (2000). "Fibers, percolation, and spalling of high-performance concrete." <u>ACI Materials Journal-American Concrete Institute</u>, Vol. 97**,** No. 3, pp. 351-359.

Bhat, P. S., Chang, V. and Li, M. (2014). "Effect of elevated temperature on strain-hardening engineered cementitious composites." <u>Construction and Building Materials</u>, Vol. 69**,** No. pp. 370-380.

Bošnjak, J., Ožbolt, J. and Hahn, R. (2013). "Permeability measurement on high strength concrete without and with polypropylene fibers at elevated temperatures using a new test setup." <u>Cement and Concrete Research</u>, Vol. 53**,** No. pp. 104-111.

Bunn, D. W. (1982). <u>Analysis for optimal decisions</u>. John Wiley & Sons.

C469M-14, A. C. (2014). "Standard Test Method for Static Modulus of Elasticity and Poisson's ratio of concrete in compression". <u>ASTM International </u>West Conshohocken, PA.

Chang, C., Huang, R., Lee, P. and Weng, T. (2011). "Application of a weighted Grey-Taguchi method for optimizing recycled aggregate concrete mixtures." <u>Cement and Concrete Composites</u>, Vol. 33**,** No. 10, pp. 1038-1049.

Chaulia, P. K. and Das, R. (2008). "Process parameter optimization for fly ash brick by Taguchi method." <u>Materials Research</u>, Vol. 11**,** No. 2, pp. 159-164.

Chen, B.-T., Chang, T.-P., Shih, J.-Y. and Wang, J.-J. (2009). "Estimation of exposed temperature for fire-damaged concrete using support vector machine." Computational Materials Science, Vol. 44, No. 3, pp. 913-920.

Chung, J. H. and Consolazio, G. R. (2005). "Numerical modeling of transport phenomena in reinforced concrete exposed to elevated temperatures." Cement and Concrete Research, Vol. 35, No. 3, pp. 597-608.

Connolly, R. J. (1995). "The spalling of concrete in fires", Aston University.

da Silva Magalhães, M., Toledo Filho, R. D. and Fairbairn, E. d. M. R. (2015). "Thermal stability of PVA fiber strain hardening cement-based composites." Construction and Building Materials, Vol. 94, No. pp. 437-447.

Davie, C., Pearce, C. and Bićanić, N. (2012). "Aspects of permeability in modelling of concrete exposed to high temperatures." Transport in porous media, Vol. 95, No. 3, pp. 627-646.

de Normalisation, C. E. (1993). "prENV 1992-1-2: Eurocode 2: Design of Concrete Structures. Part 1-2: Structural Fire Design." CEN/TC, Vol. 250, No. pp. 59-62.

Debicki, G., Haniche, R. and Delhomme, F. (2012). "An experimental method for assessing the spalling sensitivity of concrete mixture submitted to high temperature." Cement and Concrete Composites, Vol. 34, No. 8, pp. 958-963.

Dotreppe, J.-C., Franssen, J.-M. and Vanderzeipen, Y. (1999). "Calculation method for design of reinforced concrete columns under fire conditions." ACI Structural Journal, Vol. 96, No. 1, pp. 9-18.

Douglas, K. S. and Billington, S. L. (2005). "Rate dependence in high-performance fiber-reinforced cement-based composites for seismic applications". Proceedings, HPFRCC-2005 international workshop, Honolulu, Hawaii, USA.

Dwaikat, M. B. and Kodur, V. (2009). "Hydrothermal model for predicting fire-induced spalling in concrete structural systems." Fire Safety Journal, Vol. 44, No. 3, pp. 425-434.

EN, B. (2004). "1-2: 2004 Eurocode 2: Design of concrete structures-Part 1-2: General rules-Structural fire design". European Standards, London.

Erdem, T. K. (2014). "Specimen size effect on the residual properties of engineered cementitious composites subjected to high temperatures." Cement and Concrete Composites, Vol. 45, No. pp. 1-8.

Fares, H., Noumowe, A. and Remond, S. (2009). "Self-consolidating concrete subjected to high temperature: mechanical and physicochemical properties." Cement and Concrete Research, Vol. 39, No. 12, pp. 1230-1238.

Foster, S. J. (2001). "On behavior of high-strength concrete columns: cover spalling, steel fibers, and ductility." ACI Structural Journal, Vol. 98, No. 4.

Foster, S. J., Liu, J. and Sheikh, S. A. (1998). "Cover spalling in HSC columns loaded in concentric compression." Journal of structural engineering, Vol. 124, No. 12, pp. 1431-1437.

Franssen, J.-M. and Dotreppe, J.-C. (2003). "Fire tests and calculation methods for circular concrete columns." Fire technology, Vol. 39, No. 1, pp. 89-97.

Fu, Y. and Li, L. (2011). "Study on mechanism of thermal spalling in concrete exposed to elevated temperatures." Materials and Structures, Vol. 44, No. 1, pp. 361-376.

Fukuyama, H., Sato, Y., Li, V. C., Matsuzaki, Y. and Mihashi, H. (2000). "Ductile engineered cementitious composite elements for seismic structural applications". Proceedings of the 12 WCEE, Auckland.

Gallé, C. and Sercombe, J. (2001). "Permeability and pore structure evolution of silicocalcareous and hematite high-strength concretes submitted to high temperatures." Materials and Structures, Vol. 34, No. 10, pp. 619-628.

Gawin, D., Majorana, C. and Schrefler, B. (1999). "Numerical analysis of hygro‐thermal behaviour and damage of concrete at high temperature." Mechanics of Cohesive‐frictional Materials, Vol. 4, No. 1, pp. 37-74.

Gawin, D., Pesavento, F. and Schrefler, B. (2006). "Towards prediction of the thermal spalling risk through a multi-phase porous media model of concrete." Computer methods in applied mechanics and engineering, Vol. 195, No. 41, pp. 5707-5729.

Greathead, R. (1986). "Permeability of concrete containing blast furnace slag as affected by temperature, moisture, and time", PhD Thesis, University of London.

Han, C.-G., Hwang, Y.-S., Yang, S.-H. and Gowripalan, N. (2005). "Performance of spalling resistance of high performance concrete with polypropylene fiber contents and lateral confinement." Cement and Concrete Research, Vol. 35, No. 9, pp. 1747-1753.

Han, L.-H. and Lin, X.-K. (2004). "Tests on cyclic behavior of concrete-filled hollow structural steel columns after exposure to the ISO-834 standard fire." Journal of structural engineering, Vol. 130, No. 11, pp. 1807-1819.

Han, L.-H., Tan, Q.-H. and Song, T.-Y. (2014). "Fire performance of steel reinforced concrete columns." Journal of structural engineering, Vol. 141, No. 4, pp. 04014128.

Harmathy, T. (1965). "Effect of moisture on the fire endurance of building elements". Moisture in Materials in Relation to Fire Tests. ASTM International. Vol., No. Issue.

Hertz, K. (1984). "Explosion of silica-fume concrete." Fire Safety Journal, Vol. 8, No. 1, pp. 77.

Hertz, K. (1984). "Heat-induced explosion of dense concretes." Lyngby, Technical University of Denmark, Institute of Building Design Report, Vol., No. 166.

Hertz, K. D. (2003). "Limits of spalling of fire-exposed concrete." Fire Safety Journal, Vol. 38, No. 2, pp. 103-116.

Hilsdorf, H. (1967). "A method to estimate the water content of concrete shields." Nuclear Engineering and Design, Vol. 6, No. 3, pp. 251-263.

Hoseini, M., Bindiganavile, V. and Banthia, N. (2009). "The effect of mechanical stress on permeability of concrete: a review." Cement and Concrete Composites, Vol. 31, No. 4, pp. 213-220.

Huang, X., Ranade, R., Zhang, Q., Ni, W. and Li, V. C. (2013). "Mechanical and thermal properties of green lightweight engineered cementitious composites." Construction and Building Materials, Vol. 48, No. pp. 954-960.

Ichikawa, Y. (2000). "Prediction of pore pressures, heat and moisture transfer leading to spalling of concrete during fire", PhD thesis, Imperial College London.

Ichikawa, Y. and England, G. (2004). "Prediction of moisture migration and pore pressure build-up in concrete at high temperatures." Nuclear Engineering and Design, Vol. 228, No. 1, pp. 245-259.

Institution, B. S. (2000). "Cement: composition, specifications and conformity criteria for common cements". EN 197-1, London.

Institution, B. S. (2004). "Eurocode 2: Design of concrete structures: Part 1-2: General rules-Structural fire design", London.

Jansson, R. (2013). "Fire Spalling of Concrete: Theoretical and Experimental Studies", KTH Royal Institute of Technology.

Jansson, R. and Boström, L. (2010). "The influence of pressure in the pore system on fire spalling of concrete." Fire technology, Vol. 46, No. 1, pp. 217-230.

Jansson, R. and Boström, L. (2013). "Factors influencing fire spalling of self compacting concrete." Materials and Structures, Vol. 46, No. 10, pp. 1683-1694.

Jiang, J. and Yuan, Y. (2013). "Relationship of moisture content with temperature and relative humidity in concrete." Magazine of Concrete Research, Vol. 65, No. 11, pp. 685-692.

JSCE (2008). "Recommendations for Design and Construction of High Performance Fiber Reinforced Cement Composites with Multiple Fine Cracks (HPFRCC)". Sub-Committee, Recommendations for Design and Construction of HPFRCC, Concrete Committee.

Ju, Y., Liu, J., Liu, H., Tian, K. and Ge, Z. (2016). "On the thermal spalling mechanism of reactive powder concrete exposed to high temperature: Numerical and experimental studies." International Journal of Heat & Mass Transfer, Vol. 98, No. pp. 493-507.

Kalifa, P., Chene, G. and Galle, C. (2001). "High-temperature behaviour of HPC with polypropylene fibres: From spalling to microstructure." Cement and Concrete Research, Vol. 31, No. 10, pp. 1487-1499.

Kalifa, P., Menneteau, F.-D. and Quenard, D. (2000). "Spalling and pore pressure in HPC at high temperatures." Cement and Concrete Research, Vol. 30, No. 12, pp. 1915-1927.

Kanéma, M., Pliya, P., Noumowé, A. and Gallias, J. (2011). "Spalling, thermal, and hydrous behavior of ordinary and high-strength concrete subjected to elevated temperature." Journal of Materials in Civil Engineering, Vol. 23, No. 7, pp. 921-930.

Kanda, T. and Li, V. C. (2006). "Practical design criteria for saturated pseudo strain hardening behavior in ECC." Journal of Advanced Concrete Technology, Vol. 4, No. 1, pp. 59-72.

Karahan, O., Tanyildizi, H. and Atis, C. (2009). "Statistical analysis for strength properties of polypropylene-fibre-reinforced fly ash concrete." Magazine of Concrete Research, Vol. 61, No. 7, pp. 557-566.

Keleştemur, O., Arıcı, E., Yıldız, S. and Gökçer, B. (2014). "Performance evaluation of cement mortars containing marble dust and glass fiber exposed to high temperature by using Taguchi method." Construction and Building Materials, Vol. 60, No. pp. 17-24.

Khoury, G. (2008). "Polypropylene fibres in heated concrete. Part 2: Pressure relief mechanisms and modelling criteria." Magazine of Concrete Research, Vol. 60, No. 3, pp. 189-204.

Khoury, G., Majorana, C., Pesavento, F. and Schrefler, B. (2002). "Modelling of heated concrete." Magazine of Concrete Research, Vol. 54, No. 2, pp. 77-101.

Khoury, G. and Willoughby, B. (2008). "Polypropylene fibres in heated concrete. Part 1: Molecular structure and materials behaviour." <u>Magazine of Concrete Research</u>, Vol. 60**,** No. 2, pp. 125-136.

Khoury, G. A. (2008). "Passive fire protection of concrete structures." <u>Proceedings of the Institution of Civil Engineers-Structures and Buildings</u>, Vol. 161**,** No. 3, pp. 135-145.

Kim, Y. Y., Kong, H.-J. and Li, V. C. (2003). "Design of engineered cementitious composite suitable for wet-mixture shotcreting." <u>ACI Materials Journal</u>, Vol. 100**,** No. 6, pp. 511-518.

Klingsch, E. (2014). "Explosive spalling of concrete in fire", <u>PhD Thesis</u>, ETH-Z ürich.

Klinkenberg, L. (1941). "The permeability of porous media to liquids and gases". <u>Drilling and production practice</u>, American Petroleum Institute.

Ko, J., Ryu, D. and Noguchi, T. (2011). "The spalling mechanism of high-strength concrete under fire." <u>Magazine of Concrete Research</u>, Vol. 63**,** No. 5, pp. 357-370.

Kodur, V. (2000). "Spalling in high strength concrete exposed to fire: concerns, causes, critical parameters and cures". <u>ASCE Structures Congress</u>, Philadelphia, Pennsylvania, United States, pp. 1-9.

Kodur, V., Cheng, F.-P., Wang, T.-C. and Sultan, M. (2003). "Effect of strength and fiber reinforcement on fire resistance of high-strength concrete columns." <u>Journal of structural engineering</u>, Vol. 129**,** No. 2, pp. 253-259.

Kodur, V. and Khaliq, W. (2010). "Effect of temperature on thermal properties of different types of high-strength concrete." <u>Journal of Materials in Civil Engineering</u>, Vol. 23**,** No. 6, pp. 793-801.

Kodur, V. and Mcgrath, R. (2003). "Fire endurance of high strength concrete columns." <u>Fire technology</u>, Vol. 39**,** No. 1, pp. 73-87.

Kodur, V. and Phan, L. (2007). "Critical factors governing the fire performance of high strength concrete systems." <u>Fire Safety Journal</u>, Vol. 42**,** No. 6, pp. 482-488.

Kollek, J. (1989). "The determination of the permeability of concrete to oxygen by the Cembureau method—a recommendation." <u>Materials and Structures</u>, Vol. 22**,** No. 3, pp. 225-230.

Kumar, P., Barua, P. and Gaindhar, J. (2000). "Quality optimization (multi‐characteristics) through Taguchi's technique and utility concept." <u>Quality and Reliability Engineering International</u>, Vol. 16**,** No. 6, pp. 475-485.

Lau, A. and Anson, M. (2006). "Effect of high temperatures on high performance steel fibre reinforced concrete." Cement and Concrete Research, Vol. 36, No. 9, pp. 1698-1707.

Lee, J.-H., Sohn, Y.-S. and Lee, S.-H. (2012). "Fire resistance of hybrid fibre-reinforced, ultra-high-strength concrete columns with compressive strength from 120 to 200 MPa." Magazine of Concrete Research, Vol. 64, No. 6, pp. 539-550.

Lepech, M. D. and Li, V. C. (2009). "Water permeability of engineered cementitious composites." Cement and Concrete Composites, Vol. 31, No. 10, pp. 744-753.

Li, M., Wu, Z., Kao, H., Qian, C. and Sun, W. (2010). "Calculation and analysis of pore vapor pressure of concrete exposed to fire." International Journal of the Physical Sciences, Vol. 5, No. 8, pp. 1315-1323.

Li, V. C. and Leung, C. K. (1992). "Steady-state and multiple cracking of short random fiber composites." Journal of Engineering Mechanics, Vol. 118, No. 11, pp. 2246-2264.

Li, V. C., Wang, S. and Wu, C. (2001). "Tensile strain-hardening behavior of polyvinyl alcohol engineered cementitious composite (PVA-ECC)." ACI Materials Journal, Vol. 98, No. 6.

Lin, W.-M., Lin, T. and Powers-Couche, L. (1996). "Microstructures of fire-damaged concrete." Materials Journal, Vol. 93, No. 3, pp. 199-205.

Lin, Z., Kanda, T. and Li, V. (1999). "On interface property characterization and performance of fiber-reinforced cementitious composites." Concrete Science and Engineering, Vol. 1, No. pp. 173-184.

Lu, F. and Fontana, M. (2015). "A thermo-hydro model for predicting spalling and evaluating the protective methods". 4th International Workshop on Concrete Spalling due to Fire Exposure, Leipzig, Germany, pp. 385-395.

Magalhães, M., Toledo Filho, R. and Fairbairn, E. (2011). "Thermal properties and resistance to thermal shock of strain hardening cement-based composites". Proceedings of 2nd International RILEM Conference on SHCC, pp. 189-198.

Majumdar, P., Gupta, A. and Marchertas, A. (1995). "Moisture propagation and resulting stress in heated concrete walls." Nuclear Engineering and Design, Vol. 156, No. 1, pp. 147-158.

Mauroux, T., Benboudjema, F., Turcry, P., Aït-Mokhtar, A. and Deves, O. (2012). "Study of cracking due to drying in coating mortars by digital image correlation." Cement and Concrete Research, Vol. 42, No. 7, pp. 1014-1023.

Mechtcherine, V., Millon, O., Butler, M. and Thoma, K. (2011). "Mechanical behaviour of strain hardening cement-based composites under impact loading." Cement and Concrete Composites, Vol. 33, No. 1, pp. 1-11.

Mechtcherine, V., Silva, F. d. A., Müller, S. and Jun, P. (2012). "Coupled strain rate and temperature effects on the tensile behavior of strain-hardening cement-based composites (SHCC) with PVA fibers." Cement and Concrete Research, Vol. 42, No. 11, pp. 1417-1427.

Mengxiao, S., Qiang, W. and Zhikai, Z. (2015). "Comparison of the properties between high-volume fly ash concrete and high-volume steel slag concrete under temperature matching curing condition." Construction and Building Materials, Vol. 98, No. pp. 649-655.

Mills, R. (1966). "Factors influencing cessation of hydration in water cured cement pastes." Highway Research Board special report, Vol., No. 90.

Mindeguia, J.-C., Pimienta, P., Carré, H. and La Borderie, C. (2009). "Experimental study on the contribution of pore vapour pressure to the thermal instability risk of concrete". 1st International Workshop on Concrete Spalling due to Fire Exposure.

Mindeguia, J.-C., Pimienta, P., Noumowé, A. and Kanema, M. (2010). "Temperature, pore pressure and mass variation of concrete subjected to high temperature—experimental and numerical discussion on spalling risk." Cement and Concrete Research, Vol. 40, No. 3, pp. 477-487.

Msaad, Y. and Bonnet, G. (2006). "Analyses of heated concrete spalling due to restrained thermal dilation: Application to the "chunnel" fire." Journal of Engineering Mechanics, Vol. 132, No. 10, pp. 1124-1132.

Ngo, T., Fragomeni, S., Mendis, P. and Ta, B. (2013). "Testing of Normal-and High-Strength Concrete Walls Subjected to Both Standard and Hydrocarbon Fires." ACI Structural Journal, Vol. 110, No. 3.

Nguyen, D. L., Kim, D. J., Ryu, G. S. and Koh, K. T. (2013). "Size effect on flexural behavior of ultra-high-performance hybrid fiber-reinforced concrete." Composites Part B: Engineering, Vol. 45, No. 1, pp. 1104-1116.

Noumowe, A., Carré, H., Daoud, A. and Toutanji, H. (2006). "High-strength self-compacting concrete exposed to fire test." Journal of Materials in Civil Engineering, Vol. 18, No. 6, pp. 754-758.

Noumowe, A., Clastres, P., Debicki, G. and Costaz, J.-L. (1996). "Transient heating effect on high strength concrete." Nuclear Engineering and Design, Vol. 166, No. 1, pp. 99-108.

Ozawa, M., Uchida, S., Kamada, T. and Morimoto, H. (2012). "Study of mechanisms of explosive spalling in high-strength concrete at high temperatures using acoustic emission." Construction and Building Materials, Vol. 37, No. pp. 621-628.

Ozbay, E., Oztas, A., Baykasoglu, A. and Ozbebek, H. (2009). "Investigating mix proportions of high strength self compacting concrete by using Taguchi method." Construction and Building Materials, Vol. 23, No. 2, pp. 694-702.

Parrott, L. (1988). "Moisture profiles in drying concrete." Advances in Cement Research, Vol. 1, No. 3, pp. 164-170.

Phan, L., Lawson, J. and Davis, F. (2001). "Effects of elevated temperature exposure on heating characteristics, spalling, and residual properties of high performance concrete." Materials and Structures, Vol. 34, No. 2, pp. 83-91.

Phan, L. T. (2008). "Pore pressure and explosive spalling in concrete." Materials and Structures, Vol. 41, No. 10, pp. 1623-1632.

Pistol, K., Weise, F., Meng, B. and Schneider, U. (2011). "The mode of action of polypropylene fibres in high performance concrete at high temperatures". Proceedings of the 2nd International RILEM Workshop on Concrete Spalling due to Fire Exposure, pp. 289-296.

Powers, T. C. and Brownyard, T. L. (1946). "Studies of the physical properties of hardened Portland cement paste". ACI Journal Proc, pp. 101-132.

Qian, C., Wang, H., Sun, W., Guo, Z. and Stroeven, P. (2005). "Numerical calculations of vapour pressure in concrete exposed to fire." Magazine of Concrete Research, Vol. 57, No. 3, pp. 179-184.

Qudah, S. and Maalej, M. (2014). "Application of Engineered Cementitious Composites (ECC) in interior beam–column connections for enhanced seismic resistance." Engineering Structures, Vol. 69, No. pp. 235-245.

Rahim, A., Sharma, U., Murugesan, K., Sharma, A. and Arora, P. (2013). "Multi-response optimization of post-fire residual compressive strength of high performance concrete." Construction and Building Materials, Vol. 38, No. pp. 265-273.

Ramezanianpour, A. and Malhotra, V. (1995). "Effect of curing on the compressive strength, resistance to chloride-ion penetration and porosity of concretes incorporating slag, fly ash or silica fume." Cement and Concrete Composites, Vol. 17, No. 2, pp. 125-133.

RILEM, T. (2007). "Recommendation of RILEM TC 200-HTC: Mechanical concrete properties at high temperatures—modelling and application, Part 10: Restraint stress." Materials and Structures, Vol. 38, No. pp. 913-919.

Roy, R. K. (2010). A primer on the Taguchi method. Society of Manufacturing Engineers.

Şahmaran, M., Lachemi, M., Hossain, K. M. and Li, V. C. (2009). "Internal curing of engineered cementitious composites for prevention of early age autogenous shrinkage cracking." Cement and Concrete Research, Vol. 39, No. 10, pp. 893-901.

Sahmaran, M., Lachemi, M. and Li, V. C. (2010). "Assessing mechanical properties and microstructure of fire-damaged engineered cementitious composites." ACI Materials Journal, Vol. 107, No. 3.

Şahmaran, M. and Li, V. C. (2009). "Durability properties of micro-cracked ECC containing high volumes fly ash." Cement and Concrete Research, Vol. 39, No. 11, pp. 1033-1043.

Şahmaran, M., Özbay, E., Yücel, H. E., Lachemi, M. and Li, V. C. (2011). "Effect of fly ash and PVA fiber on microstructural damage and residual properties of engineered cementitious composites exposed to high temperatures." Journal of Materials in Civil Engineering, Vol. 23, No. 12, pp. 1735-1745.

Saito, H. (1966). "Explosive spalling of prestressed concrete in fire." Bulletin of Japan Association for Fire Science and Engineering, Vol. 15, No. 2, pp. 23-30.

Sanjayan, G. and Stocks, L. (1993). "Spalling of high-strength silica fume concrete in fire." Materials Journal, Vol. 90, No. 2, pp. 170-173.

Saul, A. and Wagner, W. (1987). "International equations for the saturation properties of ordinary water substance." Journal of Physical and Chemical Reference Data, Vol. 16, No. 4, pp. 893-901.

Saul, A. and Wagner, W. (1989). "A fundamental equation for water covering the range from the melting line to 1273 K at pressures up to 25 000 MPa." Journal of Physical and Chemical Reference Data, Vol. 18, No. 4, pp. 1537-1564.

Sengers, J. (1986). "Improved international Formulations for the Viscosity and Thermal Conductivity of Water Substance." J. Phys. Chem. Ref. Data, Vol. 15, No. 4.

Shekarchi, M., Debicki, G., Billard, Y. and Coudert, L. (2003). "Heat and mass transfer of high performance concrete for reactor containment under severe accident conditions." Fire technology, Vol. 39, No. 1, pp. 63-71.

Shorter, G. and Harmathy, T. (1965). "Moisture clog spalling." Proceedings of institution of civil engineers, Vol. 20, No. pp. 75-90.

Sun, H., Yao, J., Fan, D.-Y., Wang, C.-C. and Sun, Z.-X. (2015). "Gas transport mode criteria in ultra-tight porous media." International journal of heat and mass transfer, Vol. 83, No. pp. 192-199.

Tan, K. H., Liu, J.-C. and Liu, J. (2015). "Fire Performance Of Fiber-Reinforced Concrete: Research Needs". 4th International Workshop on Concrete Spalling due to Fire Exposure, pp. 145-164.

Tan, T. and Ng, L. (2006). "Predicting non-evaporable water loss of cement paste at elevated temperature." Advances in Cement Research, Vol. 18, No. 2, pp. 83-89.

Tanyıldızı, H. (2014). "Post-fire behavior of structural lightweight concrete designed by Taguchi method." Construction and Building Materials, Vol. 68, No. pp. 565-571.

Tanyildizi, H. and Şahin, M. (2015). "Application of Taguchi method for optimization of concrete strengthened with polymer after high temperature." Construction and Building Materials, Vol. 79, No. pp. 97-103.

Tapkın, S. (2008). "The effect of polypropylene fibers on asphalt performance." Building and Environment, Vol. 43, No. 6, pp. 1065-1071.

Tenchev, R., Li, L., Purkiss, J. and Khalafallah, B. (2001). "Finite element analysis of coupled heat and mass transfer in concrete when it is in a fire." Magazine of Concrete Research, Vol. 53, No. 2, pp. 117-125.

Tenchev, R. and Purnell, P. (2005). "An application of a damage constitutive model to concrete at high temperature and prediction of spalling." International Journal of Solids and Structures, Vol. 42, No. 26, pp. 6550-6565.

Uysal, M. (2012). "Taguchi and Anova approach for optimisation of design parameters on the compressive strength of HSC." Magazine of Concrete Research, Vol. 64, No. 8, pp. 727-735.

Van der Heijden, G., Pel, L. and Adan, O. (2012). "Fire spalling of concrete, as studied by NMR." Cement and Concrete Research, Vol. 42, No. 2, pp. 265-271.

van Zijl, G. P., Wittmann, F. H., Oh, B. H., Kabele, P., Toledo Filho, R. D., Fairbairn, E. M., Slowik, V., Ogawa, A., Hoshiro, H. and Mechtcherine, V. (2012). "Durability of strain-hardening cement-based composites (SHCC)." Materials and Structures, Vol. 45, No. 10, pp. 1447-1463.

Wagner, C., Dollase, A. and Slowik, V. (2012). "Evaluation of crack patterns in SHCC with respect to water permeability and capillary suction". Concrete Repair,

Rehabilitation and Retrofitting III: 3rd International Conference on Concrete Repair, Rehabilitation and Retrofitting, ICCRRR-3, 3-5 September 2012, Cape Town, South Africa, CRC Press, pp. 351.

Wu, X., Wu, Z.-M., Zheng, J.-J., Ueda, T. and Yi, S.-H. (2013). "An experimental study on the performance of self-compacting lightweight concrete exposed to elevated temperature." Magazine of Concrete Research, Vol. 65, No. 13, pp. 780-786.

Xing, Z., Beaucour, A.-L., Hebert, R., Noumowe, A. and Ledesert, B. (2011). "Influence of the nature of aggregates on the behaviour of concrete subjected to elevated temperature." Cement and Concrete Research, Vol. 41, No. 4, pp. 392-402.

Xu, Y., Wong, Y., Poon, C. and Anson, M. (2001). "Impact of high temperature on PFA concrete." Cement and Concrete Research, Vol. 31, No. 7, pp. 1065-1073.

Yang, E. and Li, V. C. (2006). "Rate dependence in engineered cementitious composites". Int. RILEM Workshop HPFRCC in Structural Applications, pp. 83-92.

Yildirim, G., Sahmaran, M., Balcikanli, M., Ozbay, E. and Lachemi, M. (2015). "Influence of cracking and healing on the gas permeability of cementitious composites." Construction and Building Materials, Vol. 85, No. pp. 217-226.

Yu, J., Lin, J., Zhang, Z. and Li, V. C. (2015). "Mechanical performance of ECC with high-volume fly ash after sub-elevated temperatures." Construction and Building Materials, Vol. 99, No. pp. 82-89.

Yu, K.-Q., Dai, J.-G., Lu, Z.-D. and Leung, C. K. (2014). "Mechanical Properties of Engineered Cementitious Composites Subjected to Elevated Temperatures." Journal of Materials in Civil Engineering, Vol., No. pp. 04014268.

Zeiml, M., Lackner, R. and Mang, H. A. (2008). "Experimental insight into spalling behavior of concrete tunnel linings under fire loading." Acta Geotechnica, Vol. 3, No. 4, pp. 295-308.

Zeiml, M., Leithner, D., Lackner, R. and Mang, H. A. (2006). "How do polypropylene fibers improve the spalling behavior of in-situ concrete?" Cement and Concrete Research, Vol. 36, No. 5, pp. 929-942.

Zhang, Q., Ranade, R. and Li, V. C. (2014). "Feasibility Study on Fire-Resistive Engineered Cementitious Composites." ACI Materials Journal, Vol. 111, No. 1-6.

Zhao, J., Zheng, J.-J., Peng, G.-F. and van Breugel, K. (2014). "A meso-level investigation into the explosive spalling mechanism of high-performance concrete under fire exposure." Cement and Concrete Research, Vol. 65, No. pp. 64-75.

Zhukov, V. (1975). "Explosive failure of concrete during a fire." <u>Translation No. DT</u>, Vol. 2124**,** No.

Appendix. Formulations to determine the quantities of concrete components

If $w/c \geq 0.44\alpha_u$,

$$m_{cw} = 0.23\alpha_u m_{cem} \tag{H.1}$$

$$m_{gw} = 0.93\alpha_u m_{gw} + 0.34\alpha_p \eta_s \left(s/c\right) m_{cem} \tag{H.2}$$

$$m_{fw} = \left(w/c - 0.44\alpha_u\right) m_{cem} - m_{gw} \tag{H.3}$$

If $0.23\alpha_u \leq w/c < 0.44\alpha_u$,

$$m_{cw} = 0.23\alpha_u m_{cem} \tag{H.4}$$

$$m_{gw} = \left(w/c - 0.23\alpha_h\right) m_{cem} \tag{H.5}$$

$$m_{fw} = 0 \tag{H.6}$$

If $w/c < 0.23\alpha_u$,

$$m_{cw} = \left(w/c\right) m_{cem} \tag{H.7}$$

$$m_{gw} = 0 \tag{H.8}$$

$$m_{fw} = 0 \tag{H.9}$$

$$V_{cw} = m_{cw}/\rho_{cw} \tag{H.10}$$

$$V_{gw} = m_{gw}/\rho_{gw} \tag{H.11}$$

$$V_{fw} = m_{fw}/\rho_w \tag{H.12}$$

$$V_p = 1 - \left(a/c/\rho_a + 1/\rho_{cem} + V_{cw} + V_{cw} \right) \tag{H.13}$$

$$\alpha_u = \frac{1.031 w/c}{0.194 + w/c} \tag{H.14}$$

α_u: degree of hydration of cement. If no measured degree of hydration is given, the Eqn. (H.14) developed by (Mills (1966)) is used to calculate the value.

α_p: degree of pozzolanic reaction of silica fume. If no measured degree of pozzolanic reaction is given, the value is assumed to be equal to α_u.

m_{fw}: mass of free water per unit volume of concrete, kg/m^3.

m_{gw}: mass of gel water per unit volume of concrete, kg/m^3.

m_{cw}: mass of chemically-bound water per unit volume of concrete, kg/m^3.

m_{cem}: mass of cement per unit volume of concrete, kg/m^3.

η_s: percentage of pure amorphous silica in silica fume = 90%, typically.

V_{fw}: volume of free water per unit volume of concrete, m^3/m^3.

V_{gw}: volume of gel water per unit volume of concrete, m^3/m^3.

V_{cw}: volume of chemically-bound water per unit volume of concrete, m^3/m^3.

V_p: pore volume per unit volume of concrete, m^3/m^3.

ρ_w: density of water = 1000kg/m^3.

ρ_{gw}: density of gel water = 1110 kg/m^3.

ρ_{cw}: density of chemically-bound water = 1220 kg/m^3.

ρ_a: density of aggregate, = 2600 kg/m^3 if not specified.

s/c: the silica fume to cement ratio.